ABSTRACT

Title of Document: TWO-PHASE HEAT TRANSFER MECHANISMS WITHIN PLATE HEAT EXCHANGERS: EXPERIMENTS AND MODELING.

Valentin Solotych, PhD, 2015

Directed By: Professor, Jungho Kim, Department of Mechanical Engineering

Two-phase flow heat exchangers have been shown to have very high efficiencies, but the lack of a dependable model and data precludes them from use in many cases. Herein a new method for the measurement of local convective heat transfer coefficients from the outside of a heat transferring wall has been developed, which results in accurate local measurements of heat flux during two-phase flow. This novel technique uses a

chevron-pattern corrugated plate heat exchanger consisting of a specially machined Calcium Fluoride plate and the refrigerant HFE7100, with heat flux values up to 1 W cm^{-2} and flow rates up to 300 kg $m^{-2}s^{-1}$. As Calcium Fluoride is largely transparent to infra-red radiation, the measurement of the surface temperature of PHE that is in direct contact with the liquid is accomplished through use of a mid-range (3.0-5.1 µm) infra-red camera.

The objective of this study is to develop, validate, and use a unique infrared thermometry method to quantify the heat transfer characteristics of flow boiling within different Plate Heat Exchanger geometries. This new method allows high spatial and temporal resolution measurements. Furthermore quasi-local pressure measurements enable us to characterize the performance of each geometry. Validation of this technique will be demonstrated by comparison to accepted single and two-phase data. The results can be used to come up with new heat transfer correlations and optimization tools for heat exchanger designers.

The scientific contribution of this thesis is, to give PHE developers further tools to allow them to identify the heat transfer and pressure drop performance of any corrugated plate pattern directly without the need to account for typical error sources due to inlet and outlet distribution systems. Furthermore, the designers will now gain information on the local heat transfer distribution within one plate heat exchanger cell which will help to choose the correct corrugation geometry for a given task.

TWO-PHASE HEAT TRANSFER MECHANISMS WITHIN PLATE HEAT EXCHANGERS: EXPERIMENTS AND MODELING.

By

Valentin Solotych.

Dissertation submitted to the Faculty of the Graduate School of the
University of Maryland, College Park, in partial fulfillment
of the requirements for the degree of
Doctor of Philosophy
2016

Advisory Committee:
Professor Jungho Kim, Chair
Professor Michael M. Ohadi
Professor Gary A. Pertmer
Professor Reinhard Radermacher
Professor Christopher Cadou

Acknowledgements

There are a lot of people that helped me during my time as a graduate student. I will list everyone alphabetically so no one should feel bad about their position. If you are not on the list than it does not mean that I don't like you, it just means that you did not help me that much in completing my dissertation (I am looking at you, Jason). My thanks goes to:

Aerospace Machine shop (Howard and Mike): Always had a couple of minutes to help me with designing parts and using their equipment.

Amalfie, Luca (Collaborator): Did great work on creating data bases for single and two-phase correlations to which he then compared my data to. Our hour long discussions about the common topic helped me tremendously.

Aroom, Majid (ME Machine shop director): Helped me in many situations when it came to fabricating parts for my experiment.

Dessiatoun, Sascha (Intern): Did a wonderful job helping me over the summer, with figuring out how to CNC machine.

Dessiatoun, Serguei (Mentor): Thought me most of my practical engineering knowledge. He also never denied me any help whenever I asked him for advice, whether he let me use his lab equipment, borrowing tools or helping to build parts for my experiment. Russian engineering ftw.

Flores, Giovanni: For helping me polishing samples.

Greeve, Hannes: We had a lot of discussions about electronic design, which helped a lot.

Kafri, Dvir: For helping me with Matlab.

Ketchum, Christina (My wife): For being my second advisor, she helped me with my writing, listened to my boring presentations and rants about work and always gave me advice and comfort.

Kim, Jungho (Advisor): For letting me graduate, and also being a good professor/advisor. We sure had our differences when it came to research and working in the lab, but in the end he was always willing to listen to my theories, or he would take the time to explain to me why I was wrong. I also really appreciated his commitment to his students, which included: answering annoying emails, helping to write papers, hands on help for experiments and in general have the best interest of the student on mind.

Lee, Donghyeon (Intern): Became a CNC master during his short visit and reduced my work load by a lot. Also no matter what task you would throw at him he would come up with a solution.

Reich, Marius (Intern): Did most of the Labview coding, which was a little buggy, but nonetheless, good job

Root, TJ (Terp Racing): Allowed and helped me to use his CNC machine.

Scammel, Alex (Lab mate): For being in the same boat as me. Without his help and presents I am certain that my GPA would have been lower. He also helped me a lot by just listening and discussing my engineering problems.

Solotych, Juri (My dad): Truly a life saver, who sacrificed 5 month of his life to take care of our new born daughter, without him the last months of this work would have been much more difficult. Спасибо!

Warehime, Mick: For all the Matlab help.

Table of Contents

List of Figures

List of Tables

Nomenclature

A	abbreviation for the plate corrugation
a	amplitude of the corrugation [m]
B	abbreviation for the chevron angle
Bo	Boiling Number, $Bo = \frac{q''}{GH_{lv}}$
Bd	Bond number, $Bd = \frac{g\rho_l d_h^2}{\sigma}$
b	corrugation pressing depth [m]
C_i	specific constants or functions
c_p	specific Heat [J kg^{-1} K^{-1}]
d	diameter [m]
f	Fanning friction factor, $f = \frac{dP}{dz}\frac{\rho d_e}{2G^2}$
F	correction factor
G	mass Flux [kg m^{-2}s^{-1}]
g	gravitational constant, g = 9.81 [m s^{-2}]
H	specific enthalpy [J kg^{-1}]
h	heat transfer coefficient [W m^{2}K^{-1}]
i	current supplied to the heater [A]
k	thermal conductivity [W m^{-1}K^{-1}]
L	abbreviation for corrugation pitch
L_H	length of the section with constant heat generation [m]
Nu	Nusselt Number, $Nu = h\, d_h/k$
$\dot{m}$	mass rate [kg s^{-1}]
n	number of data points
n	index of refraction
p	specific constants to calculate Nu and f
P	pressure [Pa]
Pr	Prandtl Number, $Pr = c_p\mu/k$
q''	heat flux
$\dot{Q}$	heat [J s^{-1}]

q''	heat flux generated by the heater [W m^{-2}]
$\dot{q}$	volumetric heat generation by the heater [W m^{-3}]
r	reflectance
R	function for uncertainty analysis
$R_{heater,\Omega/\square}$	Sheet resistance of the heater [Ω m/m]
Re	Reynolds number, $Re = G\, d_h/\mu$
U	Liquid velocity [m s^{-1}]
T	Temperature
t	Wall thickness [m]
W	Width
We	Weber number, $We = \frac{\rho v^2 d_h}{\sigma}$
v	flow velocity [m s^{-1}]
$\dot{V}$	Volumetric flow rate [m^3 s^{-1}]
x	quality
X_{tt}	Lockhart-Martinelli parameter
X, Y, Z	Coordinates

Greek

α	angle between bulk fluid motion and corrugation pattern
β	corrugation angle [°]
γ	corrugation aspect ratio $\gamma = b/\lambda$
ε	emissivity
Θ	angle of incident
λ	Wavelength of the corrugation [m]
μ	Dynamic viscosity [kg m^{-1} s^{-2}]
μ_w	Dynamic viscosity at the wall [kg $m^{-1}s^{-2}$]
ν	Kinematic viscosity [m^2 s^{-1}]
φ	Area enhancement factor
Φ	place holder for unknown function
ρ	Density [kg m^{-3}]
σ	surface tension [kg s^{-2}]

Υ	Array of values for MAE

Subscripts

a	acceleration
C	Carbon filled polyimide
cb	convective boiling
e	equivalent
exp	experimental
G	Glue
gen	generation
H	constant heat generation
i	running variable
l	liquid
lo	liquid only
lv	liquid to vapor
m	mean
meas	measured
nb	nucleate boiling
o	outlet
pool	pool boling
pre	predicted
P	Polyimide
S	Surface
sat	saturation
tot	total
tp	two-phase
v	vapor

Acronyms

BD	black dot
CaF_2	calcium Fluoride
CNT	carbon nano tubes
HTC	heat transfer coefficient

IR	infra-red
MAE	mean absolute error
PHE	plate heat exchanger
TC	thermocouple

1. Introduction

Plate heat exchangers (PHE) as shown in Figure 1.1, are widely used in many applications (food, oil, chemical and paper industries, HVAC, heat recovery, refrigeration, etc.) because they are smaller and lighter, have lower pressure drops, and require less structural support than tube and shell heat exchangers. Furthermore, by allowing the easy removal or addition of plates to the PHE, it is easy to clean the assembly and provide flexibility for different heat load configurations.

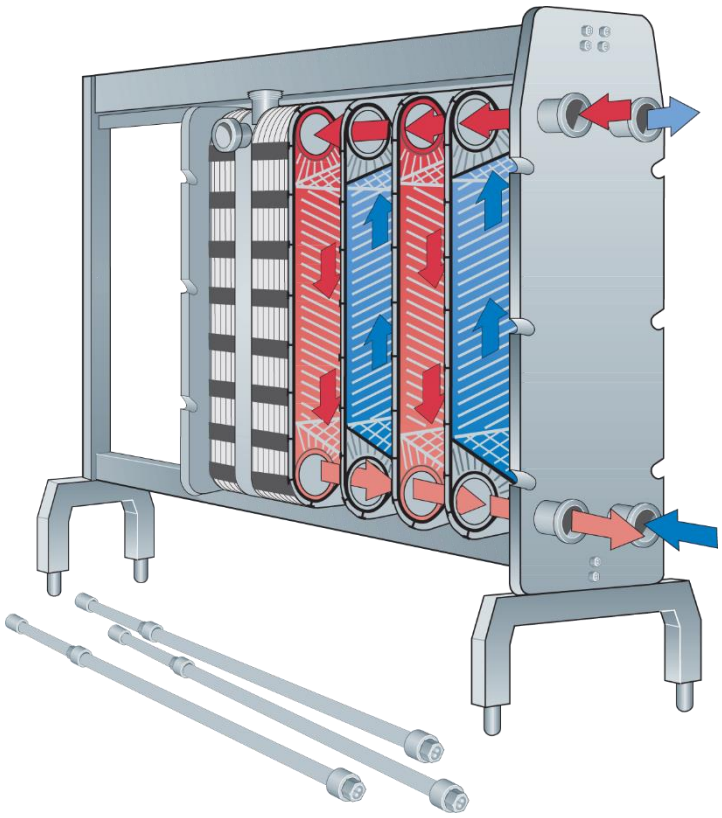

Figure 1.1: Schematics of a typical PHE
(http://www.dairyprocessinghandbook.com/chapter/heat-exchangers)

The increased heat transfer performance of PHEs is primarily due to the very large surface area per unit volume that facilitates the heat transfer between the two

fluids. The plate design, which usually consists of sinusoidal corrugations arranged in chevron patterns with opposite pitch angles within a plate pair, also contributes to the high heat transfer efficacy through mixing and agitation of the fluid.

To further improve the performance of a PHE, it is possible to operate the PHE in a two phase regime. Two phase flow has the ability to transfer large amounts of energy away from a heated surface, due to the change in phase of the fluid. The penalty for the increase in heat transfer is a higher pressure drop due to the rapid acceleration of the vapor phase, which needs to be compensated though an increase in pumping power. However, given a constant pumping power the heat transfer achieved with two-phase cooling is, in almost all cases, higher than the single phase alternative. A considerable amount of experimental and numerical research has been performed to develop correlations from which the overall heat transfer and pressure drop can be predicted for specified plate geometries and fluids with reasonable accuracy. However, very little information is available regarding local measurements of heat transfer. Local measurements can serve as benchmarks for numerical models and can provide insight into heat transfer mechanisms which can lead to improved PHE designs.

This work focuses on developing a new technique using infra-red (IR) thermography to measure local heat transfer distributions within typical PHE geometries operated as evaporators. Quasi local pressure drop measurements and two phase flow visualization are also performed to give a complete picture of the heat transferring process. This thesis is divided into seven chapters. Chapter 2 gives a brief introduction to the operation and properties of a PHE as well as fundamentals in heat transfer for single and two-phase flow. Chapter 3 provides an extensive literature

review on single and two-phase cooling of a heated PHE wall. Chapter 4 focuses on the experimental aspects of this work. The experimental technique of measuring the local heat transfer and the data reduction is described in detail followed by the uncertainty analysis of all measurements. In Chapter 5 the new technique is evaluated by comparing the measured heat transfer and pressure drop values for single phase flow, to correlations from previous publications. Local heat transfer data will be presented and analyzed. In the Chapter 6 an overview of two-phase results will be given followed with a conclusion and proposed future work.

2. Fundamentals

This section covers all the knowledge necessary to fully understand PHE and the heat transfer within the PHE. First the characteristics of the PHE geometry are explained with the commonly used nomenclature. Afterwards a brief introduction to single and two-phase heat transfer is given.

2.1 Geometry

PHEs consist of thin, rectangular, pressed sheet metal plates that are sandwiched between full peripheral gaskets and clamped together in a frame or welded/brazed, such that the hot and cold fluid streams alternate through the inter-plate passages. The plates are stamped with corrugated patterns that not only provide larger effective heat transfer surface area but also modify the flow field, thereby promoting a significantly enhanced thermal-hydraulic performance. The corrugations also help to improve the rigidity of the stack. Among a variety of surface corrugation patterns that are commercially available for the PHEs, the sinusoidal chevron corrugation geometry or a variation known as a herringbone or zig-zag pattern is the most popular used in diverse applications due to its ease of manufacturing, reduction in fouling and thermal-hydraulic performance (Figure 2.1).

Figure 2.1: Showcase of the different PHE designs

To increase mixing within the channel that is formed by the two sinusoidal plates, a corrugation angle was added to the plates. This forces the liquid to move in a zig-zag pattern rather than moving along the wave. The corrugation angle is measured in most scientific literature as shown in Figure 2.2. However in some engineering field work the corrugation angle is measured by its complimentary angle as shown in Figure 2.2.

The steeper the corrugation angle the more turbulent mixing occurs within the channel and thus the thermal performance increases. The laminar-turbulent transition in a typical PHE channel is lower than in a comparable tube flow. The penalty for this, however, is a higher pressure drop.

To change the corrugation angle, it is possible to have two plates with different corrugations pressing against each other. The resulting corrugation angle for both plates is the average of both angles. In general, PHEs with a $\beta > 45$ are defined as hard plates and for $\beta < 45$ as soft plates.

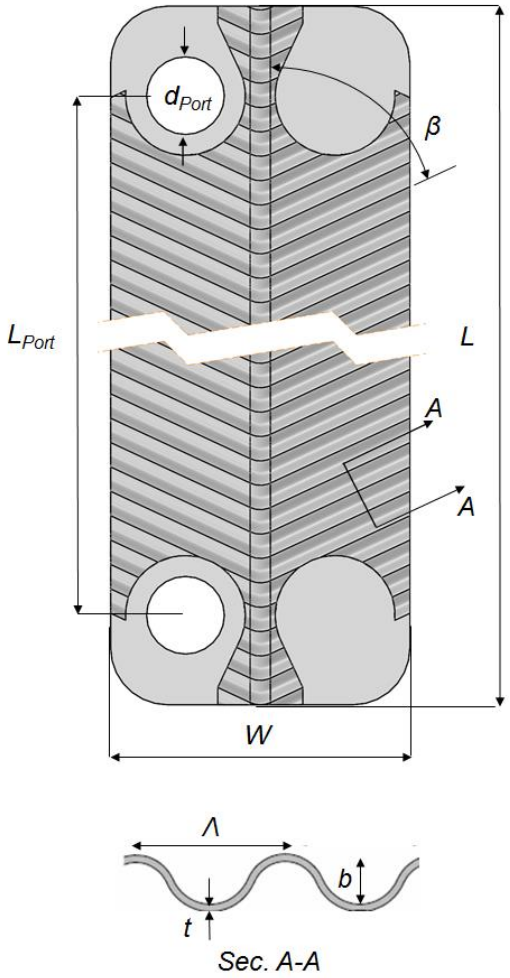

Figure 2.2: Corrugation features of a typical chevron plate:

In order to rate and compare the performance of PHEs, several non-dimensional parameters were introduced, which are the plate corrugation aspect ratio γ, and the enlargement factor φ a are given by Equation 2.1 and 2.2 respectively:

$$\gamma = \frac{4a}{\Lambda} \tag{2.1}$$

$$\varphi = \frac{Effective\ Area}{Projected\ Area} = \frac{\int_0^{\Lambda} \sqrt{1 + \left(\frac{\gamma\pi}{2}\right)^2 \cos\left(\frac{2\pi}{\Lambda}x\right)^2}\, dx}{\Lambda} \tag{2.2}$$

Where a and Λ are the respective amplitude and wavelength (pitch) of a sinusoidal surface corrugation as show in Figure 2.2.

For characterizing flow and heat transfer parameter such as Reynolds number, friction factor and Nusselt number, a hydraulic diameter (d_h) is introduced:

$$d_h = \frac{4a}{\varphi} = \frac{2b}{\varphi} \qquad 2.3$$

With the help of Equations 2.1-2.3 any sinusoidal PHE characteristic can be fully explained. The nomenclature used in this paper to characterize the corrugation patterns is shown in Figure 2.3. The wavelength and amplitude of the corrugation are indicated by L and A respectively. The chevron angle B is followed by two numbers since PHEs can be arranged in a mixed configuration resulting in an overall angle which is the average of both plates, e.g., mixing a 60° and 30° plate would result in a 45° arrangement. As an example of the nomenclature, the PHE L3.7A0.5B65-65 would have a corrugation wavelength of 3.7 mm, an amplitude of 0.5 mm, and two plates both having chevron angles of 65°.

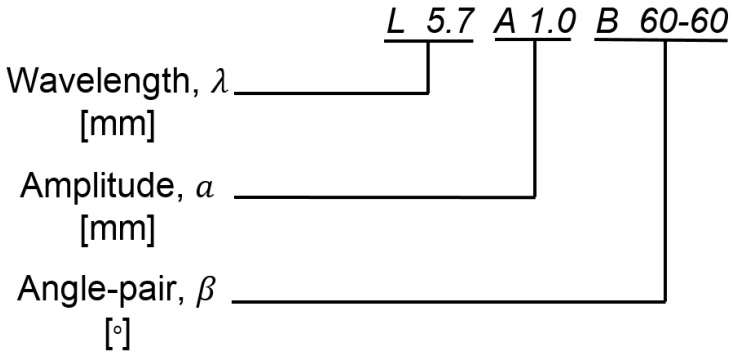

Figure 2.3: Nomenclature to characterize a PHE geometry

2.2 Single Phase Flow

2.2.1 Heat transfer

When a fluid moves across a solid or liquid surface of different temperature, a convective heat transfer occurs. The convective heat transfer describes the energy transport through the collective movement of molecules from one place to another, in contrast to heat conduction which is based on the energy transport between molecules. Heat transfer through convection and conduction happens when a fluid flows over a wall. Depending on the physical properties of the wall and the fluid, one heat transfer mechanism will dominate the other. The temperature and velocity profile of the moving fluid are strongly coupled and thus influence each other. The definition of the convection coefficient according to Newton's law of cooling is:

$$h = \frac{q''_{wall}}{T_{wall} - T_{Fluid}} \qquad 2.4$$

This law indicates that the heat transfer between the fluid and the wall is linearly dependent on the heat transfer coefficient.

Due to the nature of the fluid's boundary layer which is closest to the wall, the velocity of the fluid approaches zero at the fluid-wall interface. This region is known as the viscous sublayer. Thermal conduction is the dominating heat transfer mechanism in this layer. Consequently, convective heat transfer depends on conduction over the temperature profile in the viscous sublayer and the temperature gradient near the surface determines the convection coefficient. With conduction in the stagnant fluid near the wall and k_{Fluid} the thermal conductivity of the fluid, the heat flux is

$$q''_{wall} = -k_{Fluid}\left(\frac{\delta(T - T_{wall})}{\delta y}\right)_{wall} \quad 2.5$$

Substituting Equation 2.5 into 2.4 will result in the following expression:

$$h = k_{wall}\frac{\left(\frac{\delta(T_{wall} - T)}{\delta y}\right)_{wall}}{T_{wall} - T_{Fluid}} \quad 2.6$$

The ratio of k/h is an illustrative estimation of the thermal boundary layer thickness. Furthermore, when taking the inverse of the mentioned ratio and multiplying it with a characteristic length (e.g. the equivalent diameter of a channel flow) one would get the dimensionless Nusselt number which is used to describe the ratio between convective and conductive heat transfer:

$$Nu = \frac{hd_{eq}}{k} \quad 2.7$$

The Nusselt number is commonly used to compare heat transfer performance within single phase cooled channels. Single-phase heat transfer correlations have been proposed by several investigators. Most correlations for PHE are similar to the Dittus Boelter equation that is used to calculate Nu in turbulent pipe flow:

$$Nu = C_1\, Re^{C_2} Pr^{C_3}$$

With $Pr = c_p\mu/k$ being the Prandtl number which gives a ratio of momentum diffusivity to the thermal diffusivity of a liquid, and adjustable constants C_i

2.2.2 Pressure drop

During convective cooling an energy source is required to keep the liquid in motion, which in most cases is done by a pump. The energy consumed by the pump depends

heavily on the frictional losses between the fluid and the wall and viscous losses if the fluid is turbulent. These losses can be described as a pressure drop ΔP, since the static pressure in the flow will continuously decrease downstream of the pump. The goal of the PHE geometry is to create a turbulent flow which is more desirable for high heat transfer rate, due to the strong mixing within the turbulent boundary layer. Calculating pressure losses during turbulent flow cannot be done analytically. However it is known that in fully developed turbulent flow, the pressure drop in a horizontal constant-area pipe depends on pipe diameter d, pipe length L, pipe roughness e, average flow velocity $\bar{v}$, fluid density ρ, and fluid viscosity μ. In functional form this can be written as:

$$\Delta P = f(d, L, e, \bar{v}, \rho, \mu) \tag{2.8}$$

Through dimensional analysis Equation 2.11 can be rewritten as a non-dimensional pressure drop:

$$\frac{\Delta P}{\rho \bar{v}^2} = f\left(\frac{\mu}{\rho \bar{v} d}, \frac{L}{d}, \frac{e}{d}\right) \tag{2.9}$$

Experiments have shown that the non-dimensional pressure drop is directly proportional to the term $\frac{L}{d}$. In addition we introduce the dimensionless Reynolds number as $Re = \mu/(\rho \bar{v} d)$ and the number $\frac{1}{2}$ into the denominator of the left side, so it becomes the ratio of the pressure drop to the kinetic energy per unit mass of flow:

$$\frac{\Delta P}{\rho \bar{v}^2} = \frac{L}{d}\ \Phi\left(Re, \frac{e}{d}\right) \tag{2.10}$$

We can now define the unknown function $\Phi(Re, e/d)$ as the friction factor f which can be determined experimentally. In general it can be said that convective cooling

application are desired to have a high HTC while keeping the friction factor low, by means of optimizing geometry and flow parameters.

2.3 Fundamentals in Flow Boiling

During condensation and evaporation processes in channels, the liquid and the vapor take up a variety of configurations known as flow patterns. Flow patterns for circular tubes have been extensively studied, and similarities to flow patterns in PHE have been observed. Therefore, this section will give a brief introduction of flow patterns within circular tubes. Figure 2.4 shows a vertical heated tube with liquid passing through the tube from the bottom to the top. In the beginning of the tube (Section A) the heat is only transported throughout the diameter of the tube through convective heat transfer. After a certain entrance length the temperature of the fluid that is in direct contact with the heated wall is so high that small bubbles begin forming on the surface although the average bulk temperature of the liquid is below saturation temperature, which is referred to as subcooled boiling (Section B).

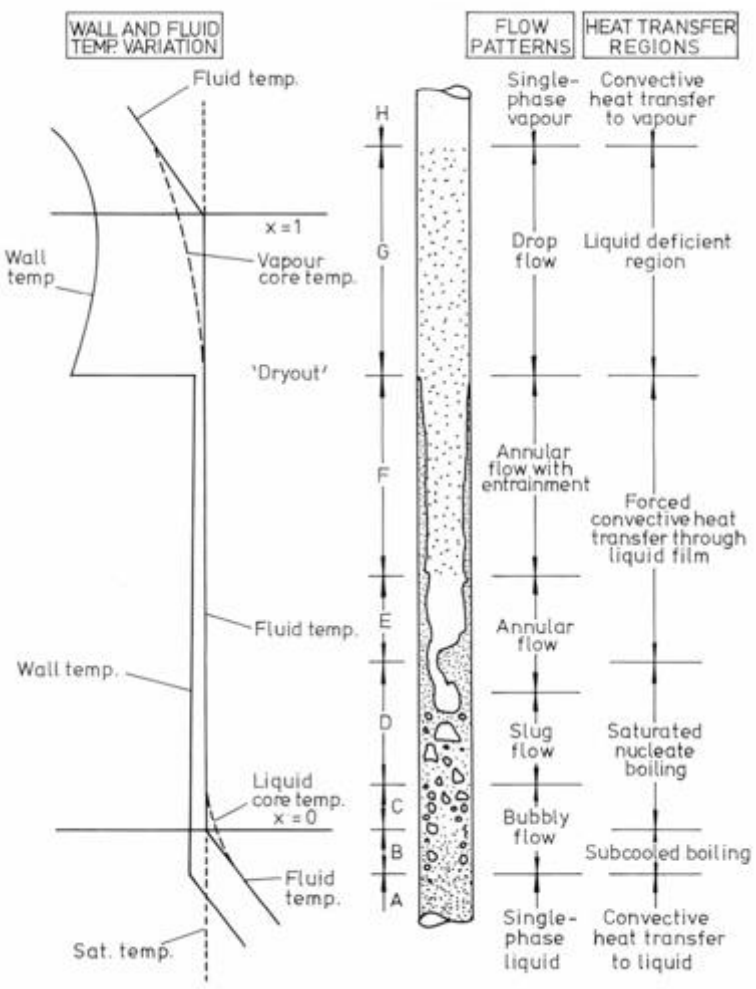

Figure 2.4: Vertical heated tube exhibiting sequential stages of two-phase flow boiling from the bottom to the top (image reproduced with permission from Collier and Thome [1])

Once bubbles begin to form, a new metric (other than just temperature), is required to fully define the state of the system. A useful variable for this purpose is the thermodynamic mass quality (x) of the fluid. The thermodynamic mass quality of the fluid at a given distance, *z*, from the beginning of the tube is given by :

$$x = \frac{H(z) - H_{sat}}{\Delta H_{vap}} \qquad 2.11$$

where *H(z)* is the enthalpy of the layer of fluid at distance *z*, H_{sat} is the enthalpy of the fluid at the saturation temperature, and ΔH_{lv} is the change in enthalpy required for vaporization of the liquid. Negative values of x give a measure of how far the enthalpy of the liquid is from the saturation point. For $x = 0$ the liquid is exactly at saturation. When x is a small positive quantity ($0 < x_m < 1$) the quality gives an approximate ratio between the amount of vapor in the system to the total volume. For values greater than one the vapor is oversaturated.

The transition between regions B and C, from the subcooled nucleate boiling region to the saturated nucleate boiling region, can be clearly defined thermodynamically although the transition may not be visually so obvious. This is the point at which the liquid reaches the saturation temperature (thermodynamic equilibrium quality, $x = 0$). Due to the continued presence of vapor bubbles from the subcooled boiling region, there is a requirement that some of the liquid must be subcooled to ensure that the liquid bulk enthalpy equals that of saturated liquid. This effect is due to the temperature gradient inherent in any cross-section of the tube. The subcooled liquid flowing in the center of the channel will only reach the saturation temperature at some distance downstream of the point $x = 0$, where the liquid bulk enthalpy will be greater than that of saturated liquid. In the regions C to G the thermodynamic mass quality of the fluid can be employed as a description of how much of the volume is occupied by vapor. As the quality increases in the saturated nucleate boiling region a point may be reached, where transition in the heat transfer mechanism occurs. This transition is preceded by a change in the flow pattern from bubbly or slug flow to annular flow (regions E and F). This transition signals the change over from the

process of boiling to the process of evaporation. In the boiling regime bubble nucleation was the vector for heat transfer. The transition is made to the evaporation regime due to the thinning layer of liquid film coating the inside surface of the tube. As the thickness of the liquid film on the heating surface is such that the effective thermal conductivity is sufficient to prevent the liquid in contact with the wall from being superheated, bubble nucleation is no longer possible. Thus, heat is carried away from the wall by forced convection in the liquid film to the interface between liquid and vapor in the core of the tube where evaporation can take place. Since nucleation may be completely suppressed, the heat transfer process may no longer be called boiling. The region beyond the transition has been referred to as the two-phase forced convective region of heat transfer (Regions E and F).

The next major transition step in the flowing liquid occurs at some determinable value of the thermodynamic mass quality where the liquid film coating the inside of the tube is heated enough to have completely evaporated. This particular critical heat flux (CHF) is known as "dryout". Subsequent to dryout the wall temperature for a channel with controlled surface heat flux will begin to rise. Eventually, with continued heat flux, all transported droplets in this vapor column will also evaporate, which is known as the saturated vapor region as seen in Region H of the tube. The region between dryout and complete elimination of droplet flow is known as the liquid-deficient region as shown in Region G. This is where post-CHF heat transfer occurs. The dryout transition often limits the amount of evaporation which should be allowed to occur for a channel at a particular heat flux.

Understanding the fundamental knowledge of liquid evaporation in a smooth tube is necessary as it forms a basis for understanding almost all correlations for PHE evaporators. Most of the correlation in the literature for flow boiling in tubes can be summarized by the general equation first proposed by Chen [2] and improved by Steiner and Taborek [3]:

$$h = \left(h'_{nb}{}^{C_1} + h'_{cb}{}^{C_2}\right)^{\frac{1}{C_3}} = \left((h_{nb}F_{nb})^{C_4} + (h_{cb}F_{cb})^{C_5}\right)^{C_6} \qquad 2.12$$

The model assumes that the local flow boiling heat transfer coefficient can be obtained by summing the nucleate boiling heat transfer coefficient (h'_{nb}) and the forced convection heat transfer coefficient (h'_{cb}). F_{nb} is the correction factor for the nucleate boiling which accounts for the partial or total suppression of nucleate boiling sites in two-phase flows and F_{cb} is the correction factor for convective boiling which accounts the enhancement of convection in a two-phase flow due to the higher velocity of the two-phase flow with respect to the liquid only flow. For a PHE this formula is used by adding new empirical constants or by modifying the correction factors. Some literature uses a two-phase Nusselt number with the characteristic length being the equivalent diameter as defined in Equation 2.3.

To quantify the pressure drop during two-phase flow a similar approach as for single phase flow can be performed. However during two-phase flow applications several pressure components are added to the frictional pressure drop due to the gaseous face in the fluid. This will be discussed in detail in the data reduction section 4.4.4

3. State of the Art Literature review

Summaries of the extensive work-to-date into PHEs have been provided by Ayub [4], Manglik et al. [5] and Abu-Khader [6]. A review of recent PHE publications most pertinent to the current study (i.e., those that involve changes in geometry, local measurements, IR techniques or flow visualization) is provided below.

3.1 Single Phase flow

3.1.1 Averaged HTC and frictional factor measurements

Okada et al. [7] was one of the first research group that extensively analyzed the effect of geometrical properties of a corrugated PHE on heat transfer and pressure drop. They used water as testing fluid in a Reynolds number range of 400 to 15000. Six plates were manufactured in total. Four of them had identical wave pattern (L10A2.8BXX/XX) and only changed in corrugation angle: 30°, 45°, 60° and 75°. Three of the plates had identical corrugation angle (60°) and changed in wavelength: 8 mm, 10 mm, 15 mm and amplitude: 2.6 mm, 2.8 mm, 3.2 mm respectively. They measured that the HTC and the frictional pressure drop increases exponentially with increasing Reynolds number. HTC clearly increased with increasing corrugation angle. The rate of increase for all angles remained approximately constant by a factor of approximately 2. The pressure drop behaved similarly, with the exception that the pressure drop increased by a factor of 4 when increasing the angle from 45° to 60°, whereas the other angle changes produced lower factors (30° to 45°: increase by a factor of 2; 60° to 75°: increase by a factor of 1.4). When changing the wave length of the corrugation the HTC remained

nearly constant, however for the pressure drop a clear decrease was observed when increasing the wavelength from 10 mm to 15 mm by a factor of nearly 2.

Heavner [8] made friction factor and HTC measurements on an industrial PHE using water as the working fluid. Three plates with identical corrugation geometry and different corrugation angle were used to create 5 chevron-angle combinations: 45°/90°, 23°/90°, 45°/45°, 45°/23°, and 23°/23°. No information of the corrugation amplitude and wavelength were given in their paper, nor how they reduced their pressure data, since the pressure was measured before and after the PHE. They found that the friction factor decreases exponentially with increasing Reynolds number. The friction factor decreased with decreasing corrugation angle. When reducing the corrugation angle from 67.5° (45°/90°) to 45° (45°/45°) the friction factor decreased by a factor of 3, a further decrease to 23° reduced the friction factor by a factor of 2. For the HTC a similar relation was observed, however the ratio of decreasing HTC with decreasing corrugation angle was lower, for example the difference between the HTC for the hardest plate and softest plate was a factor of 3.

Focke et al. [9] used a PHE with the corrugation wavelength of 10 mm, an amplitude of 2.5 mm (L10A2.5BXX/XX) and corrugation angles of 0°, 30°, 45°, 60°, 72°, 80°, and 90°. They saw that the pressure drop increases with an increasing corrugation angle up to 60° with an increasing rate, after that angle the rate of increase decreased until reaching the pressure drop maximum at 80°. At 90° they observed a local minimum with similar values as the 60° plate. For heat transfer a similar trend was observed, as the global maximum accrued at an angle of 80°, and a local minimum at 90°. They concluded that an increasing corrugation angle (0°-80°) at constant

Reynolds number increases the pressure drop over 2.5 orders of magnitude, whereas the HTC only increases by a factor of 4-10. Flow visualizations showed that at an angle of 45° the fluid moves along the furrows and gets reflected into the furrow of the opposite side when reaching the edge of the plate. For 60° and 72° plates no flow visualization were available but they expected a similar flow pattern. Crossing streams induce secondary swirling motions in the flow along the furrows since the opposite furrow has liquid that moves in a direction perpendicular to the flow. When increasing the corrugation angle theses streams have a retarding effect on each other due to the velocity components being in the opposite directions. This was confirmed by a flow visualization of a 80° plate which showed a zig-zag pattern since the reflections occurred between contacts points.

Muley and Manglik [10] used two plates (L9.0A1.25B30, L9.0A1.25B60) to create two symmetric and one mixed PHE. They used water as working fluid and were able to measure pressure and overall HTC in a range of $600<Re<10^4$. They found as previous groups before that HTC and friction factor increase with increasing corrugation angle. The rate of change for both friction factor and HTC remained constant. When comparing their experimental friction data with the data from Focke et al. [9] and Thonon et al. [11] they found little agreement for the symmetric PHE. They conclude that heat transfer increases with increasing chevron angle and deeper furrows because of an increased swirl flow generation. However the increased swirl generation also increases the frictional pressure drop.

Khan et al. [12] used two plates (L13.25A1.8B30, L6.25A1.1B60) to create a L13.25A1.8B30-30 PHE, a L6.25A1.1B60-60 PHE and a mixed configuration out of

the two plates. Water was used as the working fluid and only overall heat transfer data was acquired. They found that the L6.25A1.1B60-60 geometry produces nearly twice as high HTC for low Reynolds numbers and up to 3.5 higher HTC for high Reynolds numbers compared to the L13.25A1.8B30-30 geometry. The mixed arrangement produced HTC that were closer to the ones of the L13.25A1.8B30-30 geometry. In addition they used that data to create a separate HTC correlation for each plate.

3.1.2 Local HTC measurements

Gaiser and Kottke [13] applied an ammonia absorption method (AAM) to study flow phenomena and local heat transfer coefficients of PHE plates in a wind tunnel for Re=2000 and plate profiles with various pitch angles and corrugation wavelengths. Heat transfer coefficients were determined from the light reflectance of the absorption paper samples and converted into a surface map of Nusselt number distribution.

Stasiek et al. [14] used liquid crystal thermography to measure the local temperature on a typical PHE corrugated plate. Two plates of the same geometry were placed in a wind tunnel forming the PHE channel. The upper side of the plate with the attached liquid crystal was kept at a constant temperature using a water bath. The other side was exposed to a hot air flow. They plotted the local Nusselt number distribution in a unit cell for different Re and two corrugation angles (30°, 60°). They observed that the trough heat transfer was low and the minimum in Nu was located at the contact points between the two plates. Larger Nu was observed on the upstream face of a corrugation where liquid impacted the wall. The experimental results were compared with their CFD simulations in Ciofalo et al. [15]. The model provided insight into the

swirling flow regime and the Nu values calculated with the large-eddy simulation method showed good agreement with their experimental data.

Freund and Kabelac [16] investigated local heat transfer in a PHE (L12A1.6B63-63) using temperature oscillation IR thermography (TOIRT) by using a halogen spot array whose power oscillates with time (0.1-0.2 Hz) to radiantly heat the outside of a test section formed by two PHE plates and measuring the temperature response with an IR camera. The steady-state, macroscale flow pattern was determined for a single-phase flow using water. The minimum heat transfer occurred at the crossing points of the corrugated structures and lines of local maxima occurred along the corrugations. With increasing Reynolds number, the heat transfer distribution became more uniform. They also compared the measured heat transfer distribution within a representative unit cell to a CFD simulation. The maximum velocity within the cell was three times higher than the velocity of the mean flow direction at Re=2120 which induced mixing within the fluid enhancing the heat transfer. The CFD data did not show a maximum in heat transfer just upstream of the contact point, but higher heat transfer was spread along the upstream side of a corrugation. Lower heat transfer was found downstream of the contact points, and the minimum was interrupted by spots of enhanced convection in a recirculation zone. In general the CFD simulation under predicted the measured heat transfer coefficient by up to 40% as can be seen in

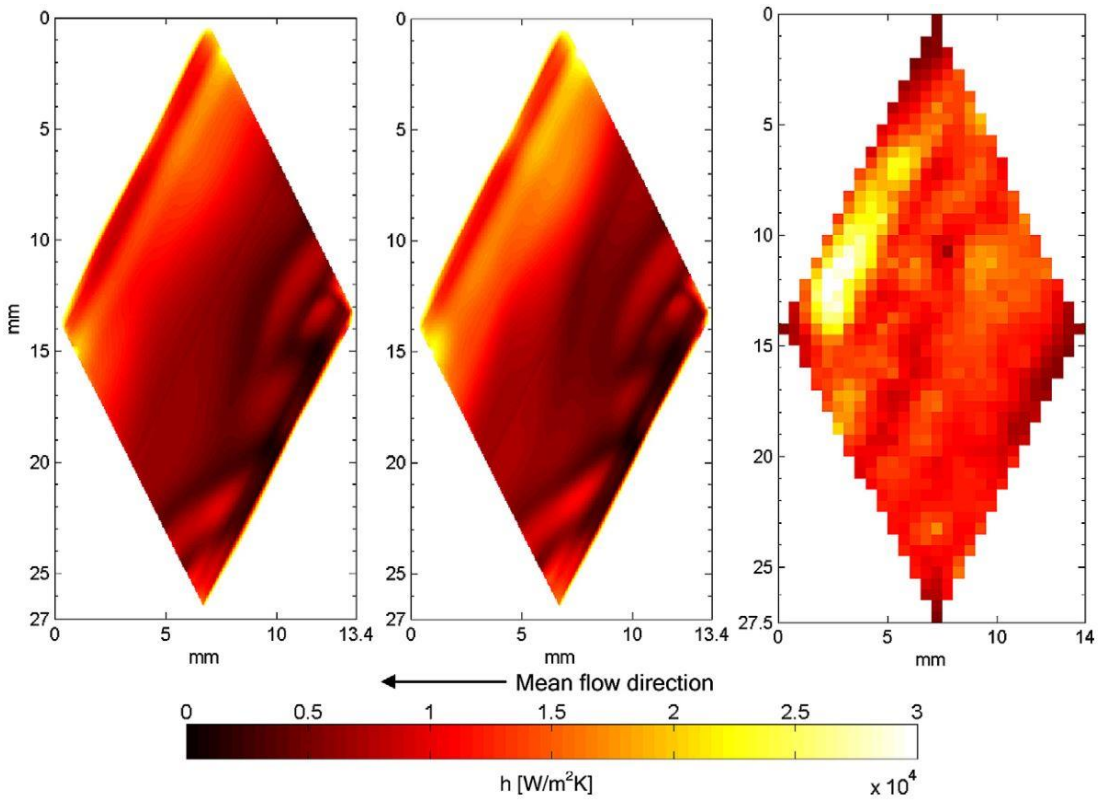

Figure 3.1: Heat transfer coefficients on the surface of a unitary cell at Re = 2120. CFD Simulation with a) SST turbulence model (left), b) RSM–EASM (middle) and (c) TOIRT measurement (right). (image reproduced with permission from Freund and Kabelac [16])

Gherasim et al. [17] used a PHE (L9.0A1.25B60-60) consisting of three plates to create two channels, one for cold water and one for hot water. Eighty thermocouples were attached to the outside plates (cold side and hot side). Except for the thermocouples on the lateral edges, the thermocouples were spaced in a 29 mm x 47 mm grid allowing measurement of the temperature profiles over each plate. Due to the relative small size of the PHE, the isotherms were very irregular with significant temperature gradients in the streamwise and cross-stream directions. The measured Nusselt number and friction factor were compared with various numerical models in Gherasim et al. [18]. They concluded that the κ-ϵ model with non-equilibrium wall functions gave the best

agreement with the experimental values. The maximum and average relative error with respect to the experimental data were 15.1% and 8.6% respectively.

Longo [19] examined heat transfer coefficients during evaporation within a brazed PHE (BPHE) consisting of 10 plates with a sinusoidal herringbone pattern. Three refrigerants (HC-600a, HC-290 and HC-1270) were tested with different inlet conditions using water for heating. The test fluids entered the BPHE with an inlet quality between $0.2<x<0.4$ and exited as superheated vapor under certain conditions. The temperature distribution along the flank of the BPHE was measured using an IR camera and used to identify the portion of the BPHE where superheated vapor was present.

Numerical investigations to study temperature and velocity distributions within a unit cell were carried out by Croce and D'Agaro [20]. Water and air were used as working fluids at two flow rates (Re=100 and Re=1000). Strong mixing was observed for water in the turbulent flow regime causing the temperature distribution within the cell to be highly uniform. Metwally and Manglik [21] studied the effect of the corrugation aspect ratio ($0\leq\gamma\leq1$, $\gamma=0\Rightarrow$flat plates) in a parallel-plate channel with in-phase sinusoidal wall waviness. For the laminar flow regime ($10\leq Re\leq1000$) they observed that Re and γ had a significant effect on the dynamic behavior of the flow field by creating swirls in the troughs.

3.2 Two-Phase Flow

3.2.1 Flow Patterns

There exist many different configurations that liquid and vapor phases may assume during evaporation. These configurations are well established for two-phase flow patterns in tubes. This arrangement has been comprehensively studied and continually improved through the development of new visualization techniques. For cross corrugated surfaces, however, flow configurations are not as well established. Most research using this geometry has been performed for only the single phase flow regime (Focke and Knibbe [22]).

Of the information available concerning two-phase flow in cross corrugated surfaces, one study was performed using water and injected nitrogen using a PHE which was formed with acrylic (Gradeck and Lebouché [23]). In this study the superficial liquid velocity was held constant while the superficial gas velocity was varied, from which only two distinct flow patterns could be observed- stratified flow and bubbly flow.

Tribbe and Müller-Steinhagen [24] further studied two-phase flow using a transparent polyester PHE. This investigation resulted in the identification of five main flow regimes: regular bubble flow, irregular bubble flow, churn flow, film flow and partial film flow.

The regular bubble flow pattern was characterized by individual bubbles ranging from 3mm to 5mm in diameter, which flowed along the furrows of both plates (Figure 3.2). Shear stresses which originated at the plane between the two heating plates

forced bubbles to flow toward plate contact points. Depending on the size of the bubble, larger bubbles would be broken up as they approached contact points, where one component of the bubble would continue in the initial direction of flow, while the second component would drop into the neighboring furrow and thereby reverse in its direction of flow. As is observed in single phase flow, an increasing chevron angle reduces the likelihood of crossing flow furrows and increases the dominance of the longitudinal wavy flow regime.

.

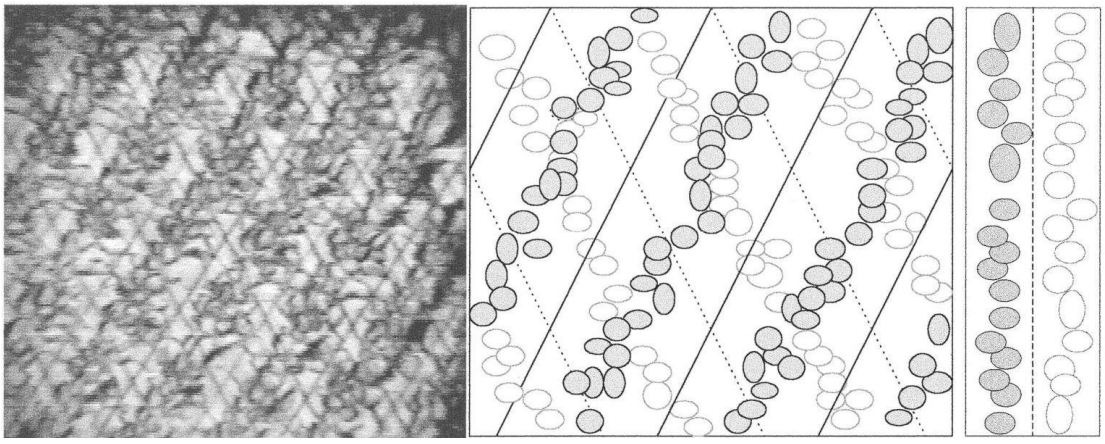

Figure 3.2: Regular bubbly flow (image reproduced with permission from Tribbe and Müller-Steinhagen [24])

With increasing gas flow rates, spherical bubbles become insufficient for transporting the quantity of gas present in the system. Instead, large irregularly shaped bubbles of gas begin to coexist with the regular bubbly flow which is a novel two-phase flow regime (Figure 3.3). These large gas regions spread over many furrows and occupy the entire depth of the channel.

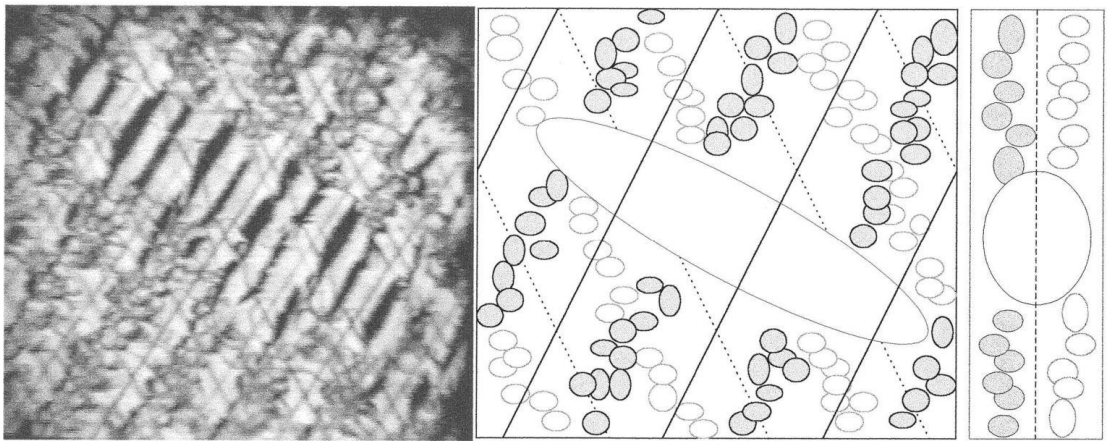

Figure 3.3: Irregular bubbly flow (image reproduced with permission from Tribbe and Müller-Steinhagen [24])

A transition from the bubbly flow regime to the churn flow regime is marked by the appearance of high-velocity liquid slugs (Figure 3.4). With increasing gas flow, the intermittencies between slugs becomes more regular and less sporadic. These slugs maintain their character throughout the channel and have a regular frequency.

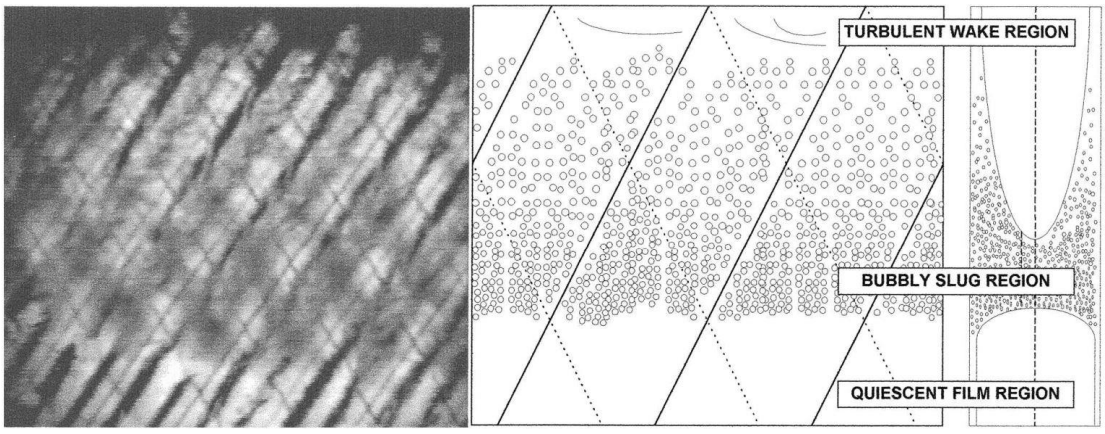

Figure 3.4: Churn flow (image reproduced with permission from Tribbe and Müller-Steinhagen [24])

The next regime, known as film flow, is defined by the presence of a thin liquid film which flows along a furrow, above which is a high velocity gas stream (Figure 3.5). The film flow regime in some ways resembles annular flow, but due to the geometry of the channel and the midplane shear the film is unable to form an annulus.

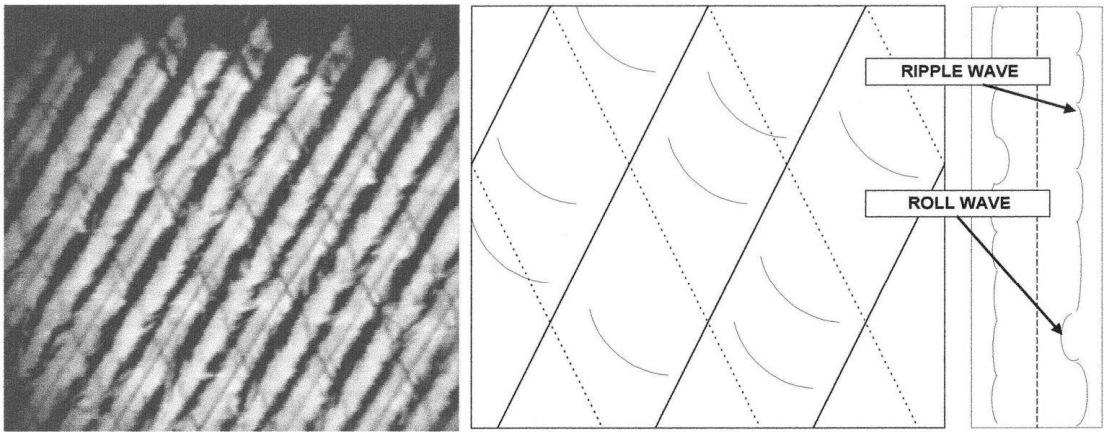

Figure 3.5: Film flow (image reproduced with permission from Tribbe and Müller-Steinhagen [24])

Finally, as the vapor flow rates increases, the film is no longer able to completely wet the surface, so that dry surface areas appear (Figure 3.6). A secondarly flow in the gas phase also results from shear forces at the midplane. Furthermore, liquid droplets are observed at the dry edge while the deposition of entrained liquid occurs at the gas/liquid interface.

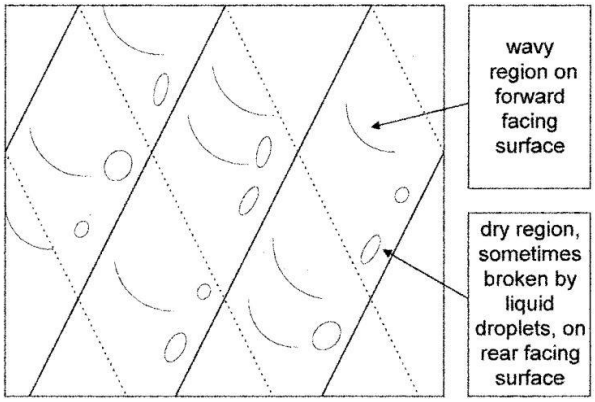

Figure 3.6: Partial film flow (image reproduced with permission from Tribbe and Müller-Steinhagen [24])

Tribbe and Müller-Steinhagen [24] produced a flow pattern map for PHEs from the observed superficial velocities.

In addition, Vlasogiannis et al. [25] removed the end plate of a PHE and replaced it with a corrugated acrylic plate (L10A1.2B60-60) in order to investigate two-phase phenomena of water-air flow. The variety of flow patterns were recorded using a high speed camera, which was then used for heat transfer and flow pattern analysis. Their results on heat transfer during two-phase flow showed that at low liquid superficial velocities (<0.025 m/s) the liquid remains at the bottom of the furrows and is sheared by a continuous gas phase. At higher liquid superficial velocities (>0.1 ms) and low air velocities a continuous liquid phase pervades the channel area. At an intermediate up to high superficial air and water flow velocities, they observed a mixture of both regimes or slug flow. The heat transfer coefficient was calculated to be higher with injected air than without it, which is especially true for low superficial water velocities.

Hsieh et al. [26] used a L10A1.5B60-60 PHE with an acrylic plate to visualize two-phase flow of R-134a. With an increase in heat flux at a given mass flux, larger bubbles formed before departing the surface. When the heat flux was constant and the mass flux changed, the bubble size was noticeably affected. Small, individual bubbles were observed at high subcooling, whereas bubbles would coalesce and move vigorously at lower subcooling.

The visualization of air/water two-phase flow was studied by Asano et al. [27] for a commercial PHE. These plates were opaque in the visible light spectrum so visualization was performed using thermal neutron radiography. The liquid and air distributions were found for one channel and also a multichannel PHE from which a distribution of phases was derived. Two-phase flow was introduced into the PHE,

where the gaseous phase occupied the center of the channel while the liquid phase occupied the sides.

Nilpueng and Wongwises [28] used a similar visualization technique as Vlasogiannis et al. [25], by removing the end plate of a commercial PHE and replacing it with an identical plate made out of transparent polyurethane. They used a non-symmetrical plate with chevron angles of 55° and 10°. By switching the flow direction they were able to see different flow patterns that were based on the inlet quality and gravity effect. For the vertical upward flow, bubble recirculation flow and bubbly flow were observed, whereas for the vertical downward flow slug flow, annular-liquid bridge/air-alone flow were observed. Annular-liquid bridge flow which describes a thin water film that is present over the whole plate surface while the air flows between the water films, was observed in both cases.

All of the above mentioned analysis of flow patterns is based on the experimental results of adiabatic gas and liquid mixture. Certainly, the fluid may experience significantly different flow patterns if either condensation or evaporation is involved.

3.2.2 Two-Phase heat transfer and pressure drop measurement

Danilova et al. [29] was one of the first researchers to investigate heat transfer in PHE geometries during evaporation. R12, R22, R113 and ammonia were used as working fluids. His group measured that the HTC increased almost linearly with an increase in quality. A correlation of a two-phase Nusselt number was established, that included the Bond number, which takes into account gravitational and surface tension force.

Engelhorn and Reinhart [30] tested R22 in an industrial PHE. They observed when elevating heat flux and mass flux, that the heat transfer increased. On the other hand, heat transfer decreased with increasing evaporation temperature. In addition, they analyzed the effect of flow distribution and found out that the maldistribution of two-phase flow can significantly decrease the heat transfer.

Tribbe and Müller-Steinhagen [31] also investigated the effect of the corrugation angle and quality on the frictional pressure drop. They were able to insert small syringe needles, with an OD of 1.2 mm through the rubber gasket, and thus measuring the pressure drop inside the PHE. The frictional pressure drop increased linearly with an increase of flow quality for all PHE tested. When changing the corrugation angle the pressure within the PHE changed significantly. When changing the angle from a 60°/60° to a 60°/30° configuration, the frictional two-phase pressure drop decreased by a factor of roughly 7.5. When further decreasing the angle from 60°/30° to 30°/30° the pressure drop decreased by a factor of approximately 2. During all tests the inlet and outlet distribution systems remained the same, as did the pressure drop over them. Therefore it became evident that the inlet and outlet distribution pressure drop has a much higher effect on the overall pressure drop for lower corrugation PHE angles.

Kumar [32] was one of the first who observed a decrease in heat transfer after reaching a certain quality ($x = 0.7$). R22 and ammonia were used in his experiments. Thonon et al. [11] gave a review of available two-phase research in PHE at that time. They were able to divide the two-phase flow into two categories, namely: nucleate boiling dominated and convective boiling dominated and provided correlations for both

of them. The criteria for categorizing the flow was a function of the boiling number (Bo) and the Lockhart-Martinelli parameter (X_{tt}).

Margat et al. [33] investigated the evaporation of R134 in a PHE in a mass flux range of $35\ kg\ m^{-2}s^{-1} \leq G \leq 120\ kg\ m^{-2}s^{-1}$ with a 60° corrugation angle and 2 mm corrugation height and an unknown wavelength. Void fraction measurement were conducted in the PHE by using a specially adapted quick closing valve technique before and after the PHE. After the valves were closed the remaining liquid in the PHE was drained in a bottle and was then weighed. They measured that the volumetric void fraction is affected by velocity and that conventional models underestimated their values. For pressure and heat transfer measurement, they saw that both are governed by mass flux and quality but not heat flux, which provided the conclusion that the main heat transfer mechanism in PHE is convective boiling (as opposed to nucleate boiling, which in general is dependent on heat flux).

As previously mentioned Ayub [4] provided an extensive summary of research carried out for single and two-phase flow in PHEs. In addition, he proposed a correlation for the evaporation of ammonia. His correlations includes parameters such as the Reynolds number, liquid thermal conductivity, and geometrical parameters like corrugation angle and overall length of the PHE channel.

Han et al. [34] used 3 different PHE geometries L4.9A1.1B70-70, L5.2A1.1B55-55, L7.0A1.1B45-45. A broad range of qualities ($0.15 < x < 0.9$) were tested for the liquids R410a and R22 in a mass flux range of $13\ kg\ m^{-2}s^{-1} \leq G \leq 34\ kg\ m^{-2}s^{-1}$. They noted that with increasing corrugation angle the heat transfer increased but only for higher qualities. For the two-phase pressure drop they saw that

the effect of changing the chevron angle became more evident at higher qualities. Varying the mass flux showed a significant effect on the HTC. Whereas changes in quality affected the HTC noticeably, only for the 70° plate. Heat flux affected the overall HTC slightly only at low qualities and low mass fluxes, due to the abrupt changes of flow path and strong turbulences within the PHE which suppresses nucleate boiling heat transfer. Correlations including equivalent Reynolds number, boiling number and geometrical parameters have been developed from the experimental data.

Park and Kim [35] investigated the evaporation heat transfer and pressure drop characteristics of R-134a in an oblong shell and PHE in a mass flux range of $40\ kg\ m^{-2}s^{-1} \leq G \leq 80\ kg\ m^{-2}s^{-1}$. The heat exchanger consisted of four oval shaped L9.0A1.4B45 plates that only had 2 ports, which were all lined up to create three parallel channels for the refrigerant. The plates were installed in a shell through which hot water was pumped, creating four vertical counter flow channels. They measured HTC and frictional pressure drop while changing quality, heat flux, system pressure, and mass flux. The data showed that HTC and frictional pressure drop are heavily dependent on mass flux and quality, whereas heat flux had almost no effect. At high qualities the saturation temperature of the fluid had a noticeable effect on the mean HTC and frictional pressure drop, when changing T_{sat} from 0 to 10°C an HTC increase of 20% was observed. This was attributed to the lower specific volume of the working fluid vapor at higher saturation temperatures, which decreases the vapor velocity and therefore decreases the shear forces to the liquid film on the heat transfer surface, and the smaller latent heat of vaporization at higher saturation temperatures. They also compared their results with standard PHE from the literature and found that the oblique

shell PHE produce higher evaporation heat transfer and higher pressure drops although the rise in heat transfer was more pronounced than that of the pressure drop.

Palm and Claesson [36] used a variety of plates with different geometries to analyze single and two-phase flow heat transfer using R134a and R22. They observed that the HTC is mainly dependent on the heat flux and less on the mass flux. Six different chevron angles ranging from 53° to 65° were analyzed to determine which angle produces the highest HTC. Their tests showed that all evaluated chevron angles produced similar HTC when varying the heat flux, however there was a modest increase at the angle of 61°. These results did not include any pressure measurement data, making it impossible to judge the performance of a PHE which includes HTC and pressure drop. A variety of different flow distributors were tested, showing that flow distribution plays a significant role for the overall HTC due to the homogeneous fluid distribution. In addition, they tried to fit their data to established pool boiling correlations. The final result was a modified correlation by Cooper [37].

Sterner and Sunden [38] tested five different PHE geometries with ammonia as the working fluid. The geometries were very similar, since the first three PHEs only differ in wavelength and only the last plate had a different corrugation angle (60° as opposed to 54°). A noticeable difference in performance between the first three PHEs was measured. The PHE with the shortest wavelength outperformed the other two. They also analyzed the effect of inlet flow distribution and observed that when adding a flow distributor the heat transfer will always increase, however the pressure loss was significant which led to the conclusion that flow distributors can be removed if pumping power is limited.

Djordjevic and Kabelac [39] used an array of thermocouples in two PHEs (L12A1.6B63-63 and L12A1.6B27-27) to measure quasi local heat transfer in a PHE during the evaporation of R134a and ammonia. The length of the PHE was 0.8 m, meaning that they could calculate the local quality and correlate the heat transfer to that quality value. They observed as many other groups that the HTC is independent of the heat flux, but heavily depends on the vapor quality. They also concluded that the HTC rises for high mass flux but decreases for lower mass fluxes at a vapor quality of ($x = 0.5$). When analyzing the effect on chevron angle on the overall HTC they observed that the low chevron angle produced a higher HTC during the evaporation of ammonia. They concluded that low chevron angles are more favorable for evaporation in PHEs especially for higher qualities (x>0.7), where strong deflections are not as effective and potentially cause local dry outs. Finally, they compared their data to previous correlations, and they found that a modified Steiner and Taborek [3] and Danilova et al. [29] model fits their data the best.

Táboas et al. [40] studied boiling heat transfer in a L9.6A1.0B60-60 PHE with an ammonia/water mixture as working fluid and a mass flux range of $50\ kg\ m^{-2}s^{-1} \leq G \leq 140\ kg\ m^{-2}s^{-1}$. At higher mass fluxes ($G \geq 100\ kg\ m^{-2}s^{-1}$) they saw an increase in HTC with increasing quality, whereas at lower mass fluxes ($G \leq 70\ kg\ m^{-2}s^{-1}$) HTC decreased with increasing quality. Heat flux affected the HTC only in the low quality region where the HTC slightly increased. Convective boiling HTC normally increases and nucleate boiling HTC decreases with decreasing system pressure, due to the changes in vapor density. When increasing the system pressure from 7 bar to 15 bar, however, no changes in HTC were detected. On the other hand,

the frictional pressure drop was reduced with an increasing system pressure, since the vapor density is higher and therefore has a lower velocity. They concluded that the main parameter that influences the HTC and the frictional pressure drop is the mass flux. Later they analyzed their data in depth and compared it to other data and correlations in Táboas et al. [41]. The group was only able to test low flow qualities ($x < 0.2$) for which they recommended a slightly modified Chisholm [42] correlation to fit their data.

Huang et al. [43] used the refrigerants R134a, R507A, in an industrial PHE evaporator with a mass flux range of $6\ kg\ m^{-2}s^{-1} \leq G \leq 31\ kg\ m^{-2}s^{-1}$. With two similar plate patterns, where the only difference was the corrugation angle, they created three different channels by using each plate pattern separately and combining the two different patterns (L8.1A1.0B28-28, L8.1A1.0B28-60, L8.1A1.0B60-60). All three PHE showed similar results for two-phase HTC. They concluded that the heat transfer mechanism is nucleate boiling dominated and therefore is strongly dependent on heat flux and less dependent on quality, mass flux and chevron angle. The frictional pressure drop however showed a strong dependence on mass flux, quality and chevron angle. A linear increase of the frictional pressure drop was observed with kinetic energy per unit volume. The pressure was measured before the inlet and after the outlet of the PHE, meaning that the inlet and outlet pressure losses had to be estimated using Shah and Focke [44]. Finally, they used statistical regression to come up with a correlation for a two-phase Nusselt number including non-dimensional groups, based on saturation temperature, thermal diffusivity and surface tension of the fluid.

Recently Khan et al. [45]–[49] gained a lot of data for the evaporation of ammonia in plate heat exchangers. A wide spectrum of plate geometries were tested with a goal to come up with empirical correlations for a two-phase Nusselt number and fanning friction factor. In Khan et al. [48] the group looked at heat transfer and pressure drop characteristics of one PHE with three different corrugation angles using ammonia as the working fluid. They showed that the overall HTC depends less on the chevron angle than the frictional pressure drop. It was also observed that the HTC depends strongly on saturation temperature and less on quality and heat flux. Furthermore, the group was very focused on industrial applications, which is why in the most recent study (Khan et al. [49]) they were the first to include miscible oil in the flow and compare it to flow without oil. They found that the oil concentration had a significant effect on the heat transfer of ammonia and friction factor.

Amalfi et al. [41, 42] provided a comprehensive literature survey of flow boiling heat transfer and two-phase frictional pressure drops mechanisms within chevron PHEs. In this study, the prediction methods available in the open literature from 1981 until 2014 were detailed and a consolidated experimental database from 13 research studies were culled that included 3601 data points. The authors carried out a sensitivity analysis to investigate the effect of plate geometrical parameters on the thermal and hydraulic performance, and an extensive statistical comparison of all available two-phase prediction methods against the above mentioned databank was also furnished. Using dimensional analysis coupled with the multi-regression technique, new methods for predicting local HTC and local frictional pressure gradient within

plate heat exchangers were developed and shown to work better than the available methods.

Recently, Vakili-Farahani et al. [43 - 44] examined the local heat transfer and pressure drop within a PHE channel (L3.7A0.5B65-65, port-to-port length of 228 mm) created by two plates that were electrically heated. The fluid was R245fa. The plates were pressed together by two PVC plates to stabilize and insulate the test section. Six windows along the length of the PHE were machined into the PVC plates allowing the outer surface temperature (and thus the local HTC) to be measured with an IR-camera. Through adiabatic two-phase flow tests, the authors were able to measure the saturation temperature of the refrigerant and thereby calculate the quasi local pressure for each window. They concluded that the two-phase behavior in PHEs is similar to pipe flow, and the flow distributions at the PHE inlet and outlet have a significant effect on the overall thermal and hydraulic performance.

In another recent publication, Lee et al. [54] used water as a working fluid in a L10A1.3B60-60 PHE evaporator at low mass fluxes ($14.5 \leq G \leq 33.6\ kg\ m^{-2}s^{-1}$). Quality values of ($0.15 < x < 0.9$) where achieved by heating the plates with an electrically heated copper block. They also observed that with an increase in quality the HTC decreased due to the partial dry-out of the liquid film. They compared their data with correlation from the literature and concluded that the correlations either over or under predict the experimental data. Therefore, the group developed a new correlation to fit the data.

3.3 Conclusion and motivation

There has been much research conducted on PHE evaporators. However, no group has analyzed the local heat transfer distribution and local pressure drop data in a PHE during evaporation at different quality levels. Also, most of the developed correlations are highly dependent on the apparatus that they were gained from. In almost all cases, researchers included inlet and outlet fluid distribution in their measurements and calculation for HTC and friction factor. There are a variety of distribution systems available and chances are small that two research groups used the same system. The pressure drop over the distributors can be significant, especially for soft PHE plates. The pressure drop in two-phase systems governs the saturation temperature of a fluid, therefore potentially falsifying the energy balance that is solved in order to calculate overall HTC.

One group was able to measure the pressure drop within the PHE but was not able to measure HTC. Other groups were able to measure local HTC for single phase flow but did not include any pressure drop measurement. This thesis presents results of truly local pressure drop and HTC measurements for four PHE geometries for single and two-phase flow. The performance of each PHE can be analyzed by comparing the overall HTC and the pressure drop with each other. In addition, high spatial resolution HTC measurements of a unit cell within a PHE coupled with adiabatic flow visualization will be presented.

Measurement of the local HTC distribution within the heat exchanger in conjunction with flow visualization allows researchers to gain insight into the mechanisms by which heat is transferred during boiling in compact heat exchangers–

this will greatly facilitate the development of new, innovative, higher performance designs based on a solid understanding of the underlying physics. Local measurements can serve as benchmarks for numerical models and can provide insight into heat transfer mechanisms, which can lead to improved PHE designs. The ability to measure local HTC for various plate geometries will lead to correlations that will be more universal.

4. Experimental Technique

This section will describe in detail the experimental setup, which includes test section and flow apparatus. The heating method and temperature acquisition method are explained next. The chapter will close with the uncertainty analysis.

4.1 Experimental Setup

4.1.1 Test Section

Representative PHE geometries L5.7A1.0B60 and L3.7A0.5B65 (Figure 4.1) were machined into CaF_2 plates using a CNC mill. Since CaF_2 is expensive, brittle, hard to machine, and since the surface temperature measurement was only required on one plate, it was decided to fabricate the opposing plate using polycarbonate. In addition two polycarbonate plates where machined with different corrugation angle to create a mixed plate configuration with a L5.7A1.0B60-30 and L3.7A0.5B65-25 geometry. The L5.7A1.0B60-60 geometry is similar to commonly used PHE evaporators, whereas the L3.7A0.5B65-65 geometry is a novel configuration that minimizes refrigerant charge, is more compact, and tries to gain higher performances by decreasing the pressing depth and corrugation wavelength. A summary of important geometrical parameters of all the plates tested in this study is shown in Table 4.1.

Plate	LP [mm]	WP [mm]	λ [mm]	a [mm]	β [°]	φ [-]	Area [cm^2]
L5.7A1.0B60	99	50	5.7	1	60	1.25	62
L5.7A1.0B30	99	50	5.7	1	30	1.25	62
L3.7A0.5B65	99	50	3.7	0.5	65	1.16	57
L3.7A0.5B25	99	50	3.7	0.5	25	1.16	57

Table 4.1: Geometric characteristics of chevron plates tested in the present study

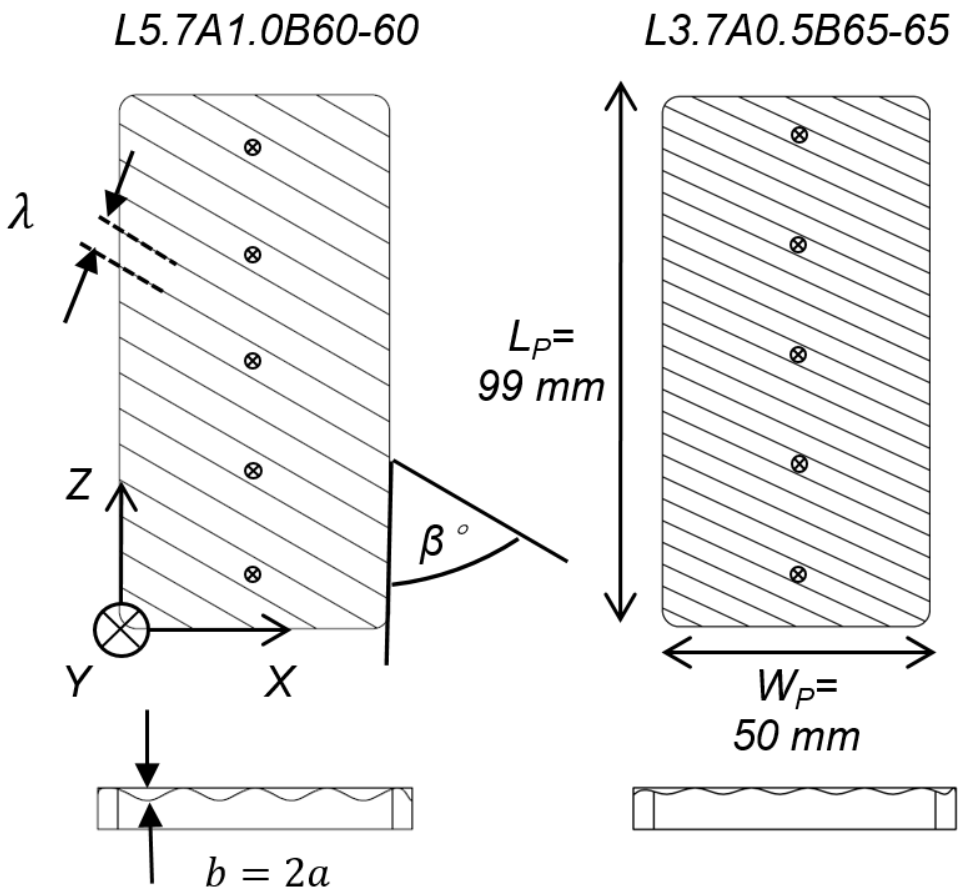

(a) (b)

Figure 4.1: Schematic of the two plate geometries that were machined into CaF_2 and the location of the thermocouples in their polycarbonate counter plate: (a) test section L5.7A1.0B60-60, (b) test section L3.7A0.5B65-65

A polycarbonate and CaF_2 plate, both with film heaters attached, were pressed together in the test section whose cross section is shown in Figure 4.3. To prevent the two heater films from shorting at the contact points, small pieces (~ 2x2 mm) of Scotch Magic™ tape (60 μm) were attached to the heated film on the polycarbonate plate at each contact point (Figure 4.2). Two T-type thermocouples were used to measure the inlet and outlet temperatures, and five T-type thermocouples were inserted into the flow. These five thermocouples were equally spaced apart along the plate (19.8 mm spaced apart, see

Figure 4.1 and Figure 4.2). They were fixed by drilling 0.6 mm holes into the polycarbonate plate and epoxying the wires so the tip would extend two times the amplitude into the channel created by the two plates.

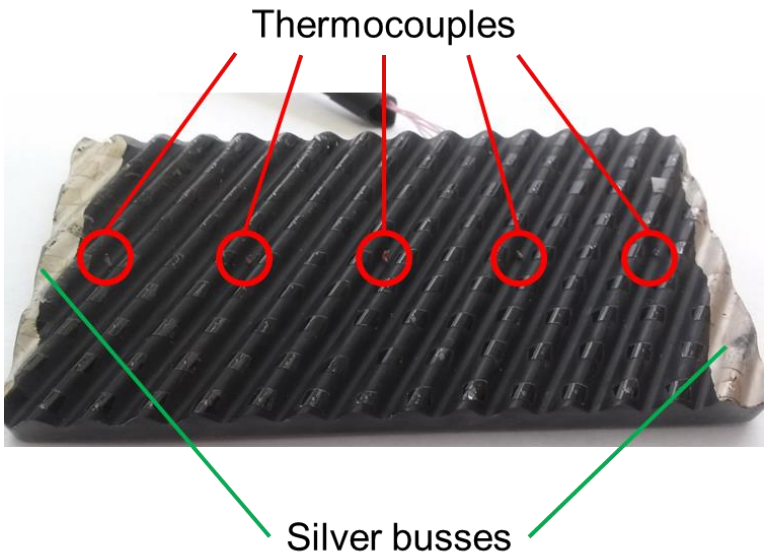

Figure 4.2: L5.7A1.0B60 polycarbonate plate with attached heater, silver busses, electrical insulating tape at the contact points, and TCs to measure bulk fluid temperature.

In addition five pressure taps (1 mm diameter holes spaced 19.8 mm apart, on the same height as the thermocouple) drilled into the side wall of the test section (Figure 4.4) were used to measure the pressure drop along the test section. Another two pressure taps where located upstream of the inlet and downstream of the outlet. To measure the pressure difference between the taps, a system of valves was used to connect the furthermost upstream tap in the PHE and any of the other taps to a single differential pressure transducer (Validyne DP15, 0-22000 Pa). Since the fluid enters and exits the test section perpendicular to the channel created by the two plates through a single inlet in the center, two 3D printed flow distributors were added between the inlet and outlet

of the channel to minimize flow maldistribution. The flow distributors were designed to continue the current PHE geometry. In addition, the flow distributors were used to hold the electrodes that connect to the silver leads painted on the film heater as well as hold thermocouples that were used to measure the channel inlet and outlet temperatures.

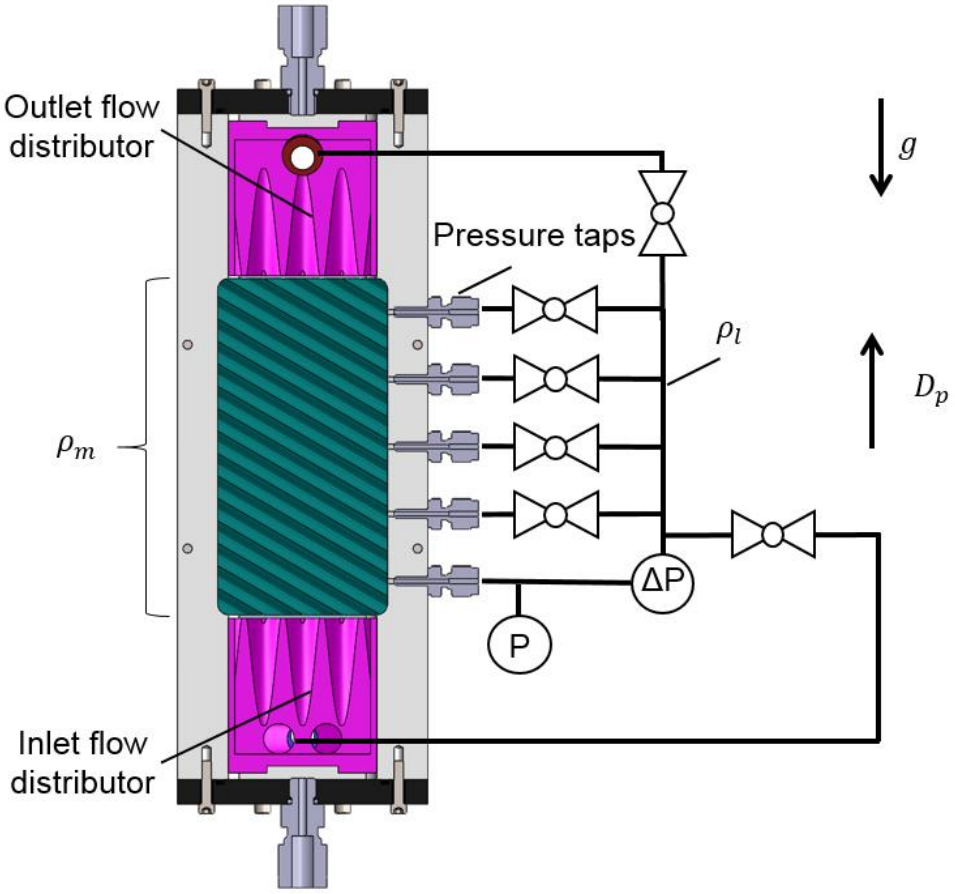

Figure 4.3: Experimental setup: cross section view of the test section, including the inlet and outlet flow distributors, pressure taps and valve system to measure absolute and differential pressure.

4.1.2 Experimental Apparatus

A schematic of the flow loop is shown in Figure 4.4. The working fluid in the primary flow loop was HFE7100 (see Table 4.2 for a summary of the properties). The fluid was chosen based on its boiling point (61°C @ 1 bar) which is ideal for the current setup since it is high enough to reduce ambient noise during IR measurements and low enough to avoid damaging heat sensitive components in the test section. It is a nontoxic fluid and is representative of other refrigerants. The fluid was pumped through a coil preheater to create the desired inlet condition for the test section. The coil heater was electrically powered by two generic 12 VDC/80 A computer power supplies combined with a solid state relay controlled using a PC through pulse-width modulation at 2 Hz. The fluid exiting the test section entered a counterflow concentric tube heat exchanger cooled by a secondary water loop. A membrane accumulator (Hydac SBO210-0.75 E1) was used to keep the pressure in the main loop at 1 atm. Liquid degassing was performed by pumping the liquid past a polyolefin membrane (Radial Flow SuperPhobic^{TM}) and using a vacuum pump to remove gas from the liquid. Two flow meter (Omega FLR 1000, 400-5000 ml/min and 0-500 ml/min), a pressure transducer (Omega PX309-030AV, 0-1 bar) and twelve T-type thermocouples were installed in the apparatus to measure the flow conditions at various locations within the loop. Two USB based National Instruments^{TM} systems were used for data acquisition (NI 9213 for all T-type thermocouples and NI 6211 for all other analog voltage measurements and preheater control).

	@25°C	@50°C	@61°C	@65°C	@70°C
Liquid density [kg m^{-3}]	1513	1443	1414	1400	1386
Vapor density [kg m^{-3}]	2.902	6.965	9.581	11.16	12.94
Thermal conductivity [W m^{-1} K^{-1}]	$6.9x10^{-2}$	$6.4x10^{-2}$	$6.2x10^{-2}$	$6.1x10^{-2}$	$6.0x10^{-2}$
Kinematic Viscosity [m^2 s^{-1}]	$3.7x10^{-7}$	$2.8x10^{-7}$	$2.5x10^{-7}$	$2.4x10^{-7}$	$2.3x10^{-7}$
Specific Heat of liquid [J $kg^{-1}K^{-1}$]	1183	1233	1255	1263	1273
Evaporation enthalpy [J kg^{-1}]	$1.23x10^{-5}$	$1.15x10^{-5}$	$1.11x10^{-5}$	$1.1x10^{-5}$	$1.08x10^{-5}$
Pr [-]	9.70	7.88	7.57	7.56	7.55

Table 4.2: Properties of HFE7100

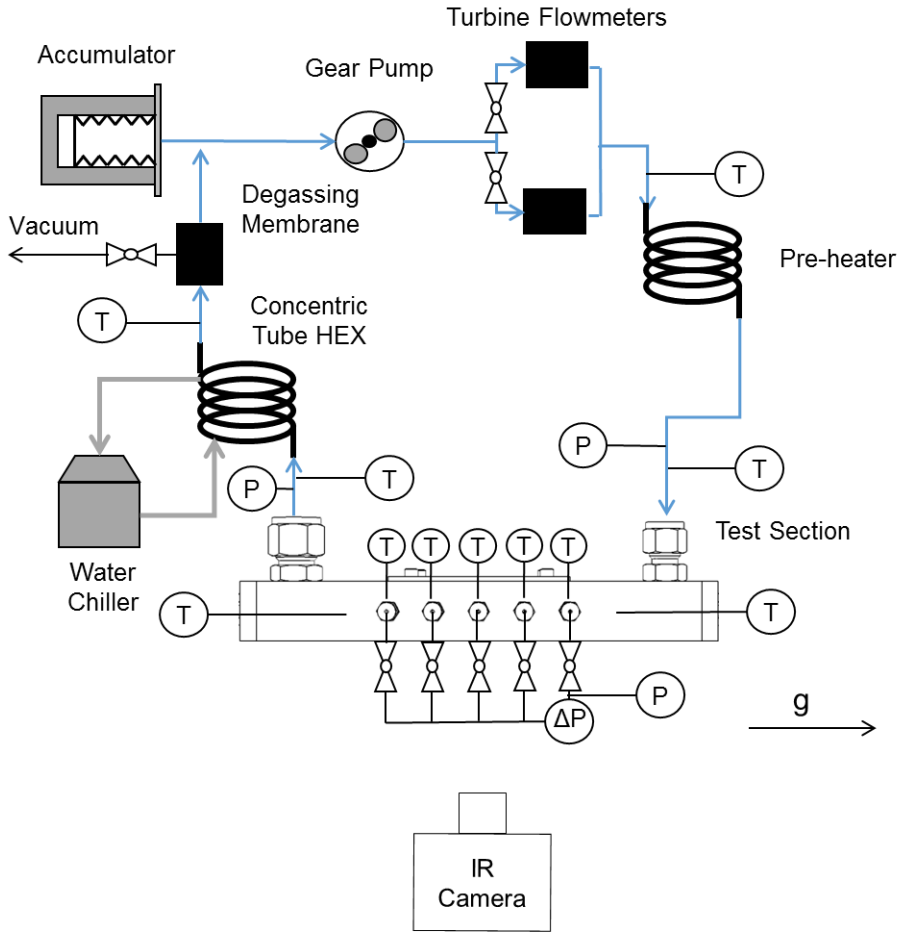

Figure 4.4: Schematic of flow loop.

4.2 Heater Setup

The principle by which the local heat transfer distribution was measured in this study is described below. A thin, flexible film heater (Dupont 200RS100) consisting of a

polyimide layer containing electrically conductive carbon (the resistance of the film was measured to be 100 Ω/□) bound to an electrically insulating polyimide layer, was used as the heating element. Since the carbon is dispersed throughout the polyimide layer, the heating was uniform and resistant to damage and cracking, unlike metallic or Indium Tin Oxide (ITO) films (see Section 8.3.2). The carbon also made this layer opaque and of high emissivity (>0.94). The thickness of the two layers were measured using an SEM (Figure 4.5).

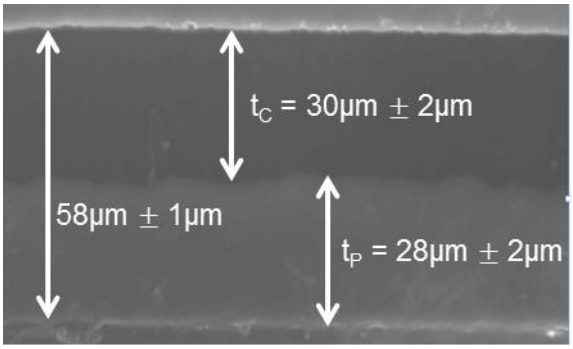

Figure 4.5 SEM image of Dupont 200RS100 cross section identifying the conducting (t_C) and non-conducting layers (t_P) and their thicknesses. The film was potted into an epoxy carrier and polished before viewing. The average values and the standard deviation about these averages are noted.

The film heater was attached to an IR transparent CaF_2 plate (Alkor Technologies) using a UV curing optical glue (Norland Optical Adhesive 61). Since the film is relatively stiff and would not stay in the trough of the corrugation without the application of force, a device was needed to hold the film in place while the adhesive could harden. The device is depicted in Figure 4.6 and consists of individual rods with the same radius as the radius of the corrugation at the trough. The rods were pushed into the through trough individual aluminum bars, so that the film would constantly be pressed against the plate. A window was machined into the baseplate of the device to

allow UV-radiation to shine though the CaF_2 plate and harden the adhesive. Using that device it was possible to create a uniform layer of adhesive without entrapping any air bubbles for most of the surface and not cracking the brittle substrate.

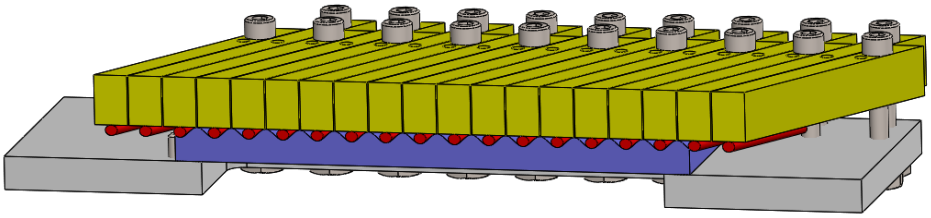

(a)

(b)

Figure 4.6: Device used to create a uniform layer of adhesive between the CaF_2 substrate and the 100RS200 film, without entrapping air bubbles and not fracturing the CaF_2, cross section view of the CAD model (a) and assembled device (b)

Electrical connections to the edges of the heater were made using silver loaded paint (SPI #5001-AB). The contact resistance between the paint and the heater was measured using a 4-wire method to be <0.25% of the overall heater resistance.

To measure the heat flux conducted into the substrate, the temperature distribution on top of the CaF_2 substrate must be known. Opaque, square dots 1x1 mm^2 were attached to the CaF_2 at select locations so this temperature could be measured. The size of the dots was large enough to ensure the camera pixel reading at the center of any dot was not influenced by the slit response function (SRF) of the camera as explained in Vollmer and Moellmann [55]. To determine the center-to-center spacing between adjacent dots, a 2-D numerical heat conduction simulation was carried out to simulate the amount of heat spreading within the polyimide film and the optical glue. A step function in temperature was used as the boundary condition on the carbon heater film and the temperature profile along the optical glue-CaF_2 interface was computed. The spacing between the dots (3 mm in our case), was chosen such that the temperature profile between the dots could be accurately reconstructed using spline interpolation (see Section 8.2.2 for a more detailed explanation). To produce the dot pattern, a negative mask made of polyimide tape was prepared using a laser cutter and attached to the CaF_2 plate. A solution containing Carbon nano tubes (CNT) dispersed within DMSO was obtained from International Technology Center, Raleigh and spray coated onto the masked surface–details of the CNT solution and the deposition procedure are described in Gokhale et al. [56]. To ensure the dots were opaque, chromium was deposited onto the CNT layer. Chromium has excellent adhesion when applied through vapor deposition and requires a relative thin layer in order to become fully opaque. The polyimide mask was then removed leaving the dots on the CaF_2 surface. The final thickness of the dots was measured to be less than 2μm. Figure 4.7 shows the schematic of the final multilayer.

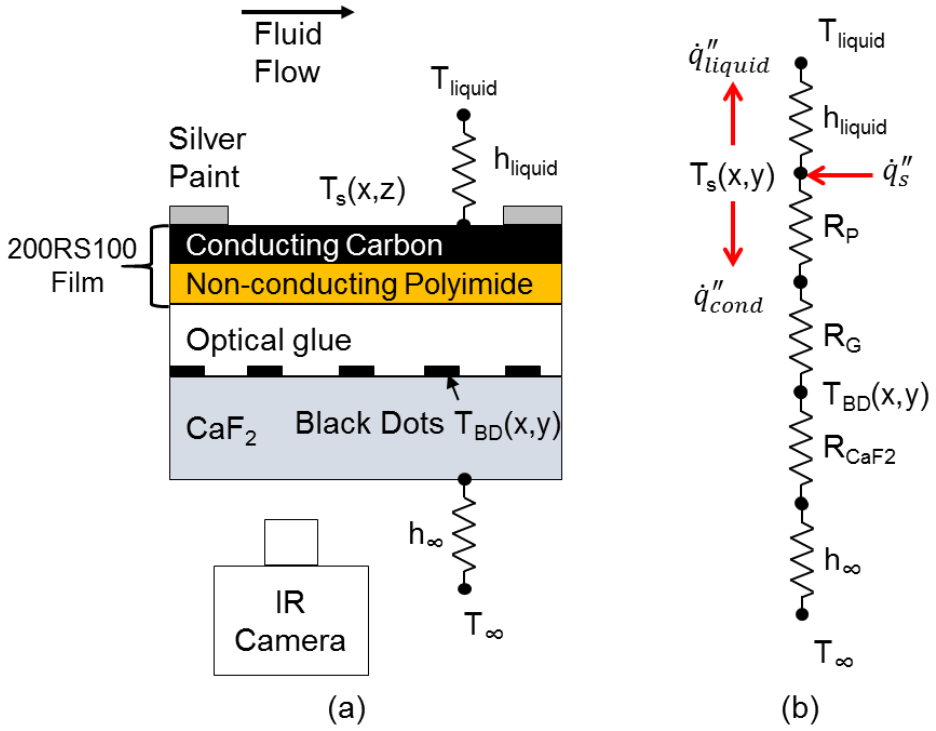

Figure 4.7: Schematic of test wall construction.

Properties of the materials used in the wall construction are summarized in Table 4.3. The thermal conductivity of the electrically conductive layer was measured to be >5 W/m-K using the technique described in Section 8.1.

Layer	k [W m^{-2}K^{-1}]	ρ [kg m^{-3}]	Abs. coefficient [m^{-1}]	Index of Refraction [-]	c_p [J kg^{-1}K^{-1}]
CaF_2	12	3180	3.5x10^{-4}	1.41	854
Polyimide Film	0.12	1420	7110	1.7	1090
Optical glue	0.17	1231	4200	1.527	-

Table 4.3: Physical properties of the transparent/translucent materials

4.3 Infrared Thermography

Infrared thermometry is an established technology whereby the measurement of infrared wavelength energy emission combined with knowledge of the surface emissivity of a substance can be used to determine its temperature. A major advantage

of this temperature measuring technique is its non-invasive nature; therefore the flow would not have to be disturbed by any mechanical means. An overview of IR thermography in heat transfer research within the last decades is given by Astarita et al. [57]. IR imaging done with scientific grade cameras can yield reasonable frame rates although the local measurement accuracy may only be as good as 2 °C due to factors such as noise and uncertainty. However, when a pixel-by-pixel calibration is carried out the accuracy can be greatly improved to around 0.2 °C.

The calibration procedure for all experiments was carried out in a standardized fashion. The camera was rigidly mounted to the same structure as the test section. This will not allow any relative movements between the camera and the CaF_2 plate, thus every pixel will have the same field of view of the test section during the experiments. Liquid with constant temperature is then pumped through the test section without powering the heater film. The camera records 100 frames and takes the average temperature value for each pixel. The quasi local temperature along the PHE channel, which is interpolated using the 7 thermocouples in the test section, is then used to calibrate each pixel of the camera. Using this technique it is possible to account for non-unity emissivity values and multiple reflections from the surroundings and from within the CaF_2 layer itself. Figure 4.8a shows the calibration curve from 3 randomly selected points across the plate. As expected the raw temperature from the IR-camera is lower than the temperature measured by the TCs due to the previously mentioned effects.

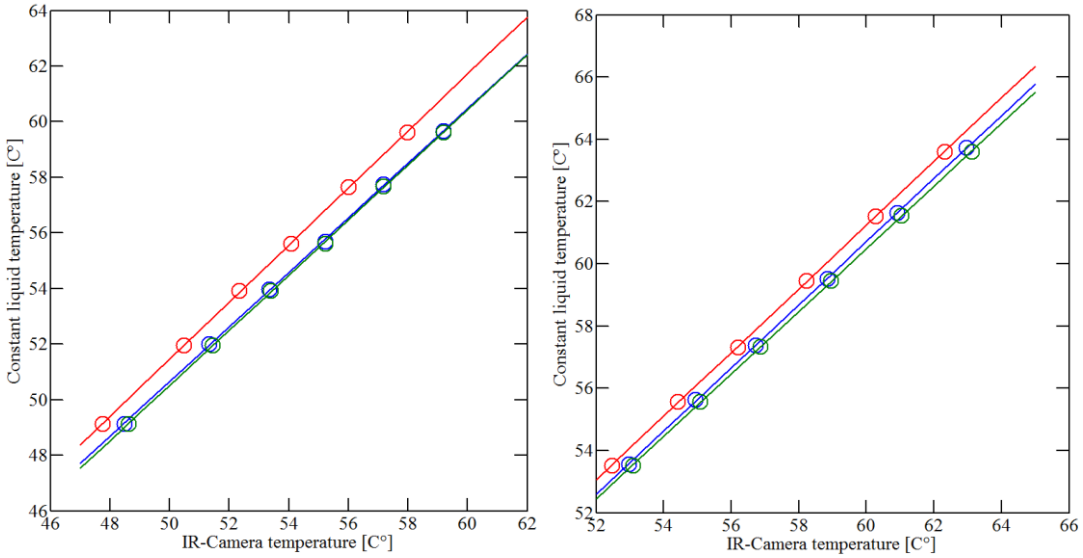

(a) (b)

Figure 4.8: IR-camera calibration for three random pixels for (a) single phase measurements and (b) two-phase measurements.

The calibration is limited to the point where the liquid reaches saturation temperature, whereas the temperature of the heated film is higher than that during evaporation. However, as can be seen by the linear behavior of the calibration curve of one pixel (Figure 4.8a), it can be assumed that the linearity will be preserved up to temperatures higher than saturation. To ensure that the linear assumption is correct a test was performed by increasing the pressure in the test loop which would raise the saturation temperature. This was done by pressurizing the open side of the accumulator. The IR-camera calibration was then carried out for higher temperatures and the linearity of the calibration remained, as can be seen in Figure 4.8b. A final validation of the calibration was done by visually inspecting the overall calibration as seen in Figure 4.9.

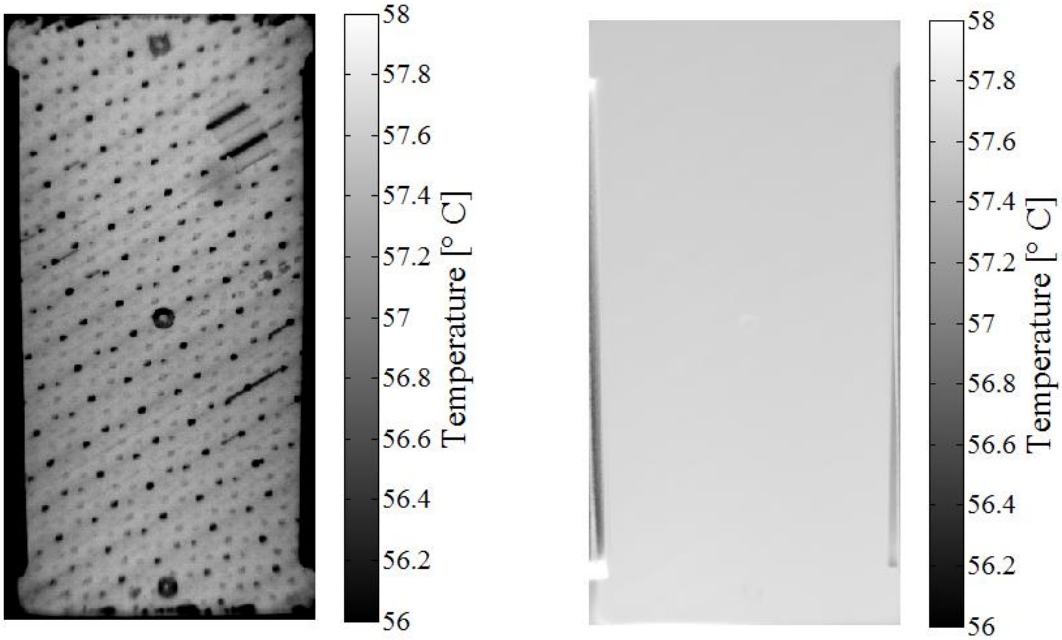

(a) (b)

Figure 4.9: IR-temperature measurement of the heater surface during calibration: Before (a) and after calibration (b).

4.4 Data Reduction

4.4.1 General heat flux and HTC calculation

The objective of this measurement technique is to enable the heat transfer coefficient distribution on the corrugated surface. The heat generated within the conducting film by applying a voltage across the silver electrodes. The heat generated per unit area within a rectangular area of the film with length L_H and width W_H is given by

$$\dot{q}''_{gen} = \frac{\dot{q}}{L_H W_H} = \frac{i^2 R_{heater,\frac{\Omega}{\square}} \left(\frac{L_H}{W_H}\right)}{L_H W_H} = \frac{i^2 R_{heater,\frac{\Omega}{\square}}}{W_H^2} \left[\frac{W}{m^2}\right] \qquad 4.1$$

where i=current through the film [A] and $R_{heater,\frac{\Omega}{\square}}$=resistance of a square section of the heater. The film that is attached to the corrugated CaF_2 plate is not rectangular,

however, but of trapezoidal shape as shown in Figure 4.10. Comsol^{TM} was used to simulate the current flow (and thus the local generation rate) within this trapezoidal shape (Figure 4.10). Heat is generated non-uniformly near the electrodes but a region of relatively uniform heat generation exists within the central portion of the film where Equation 4.1 is valid. The generation rate within the square area (W_H=52.5mm, L_H=50mm) shown in Figure 4.10 varies by up to 10%.

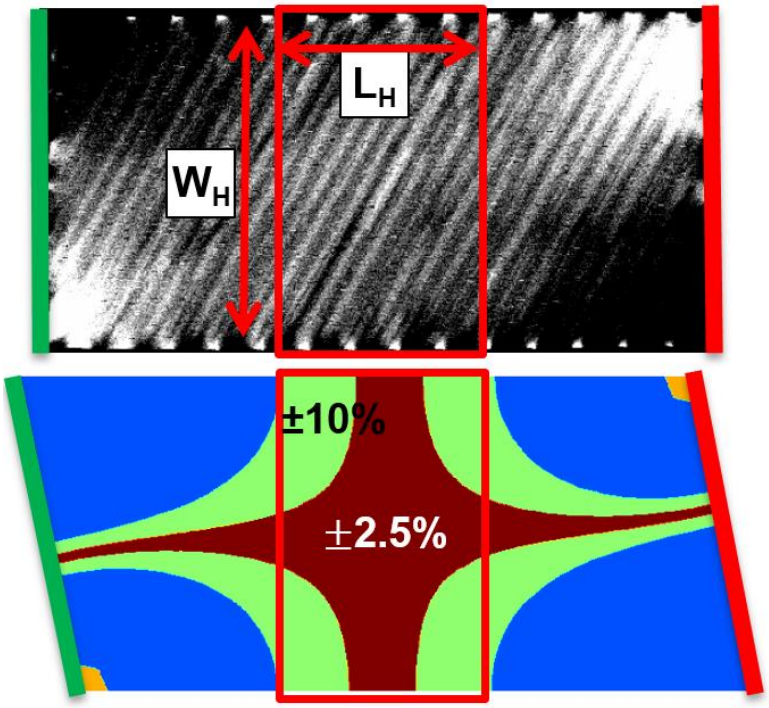

Figure 4.10 Heat generation distribution within the heating film after 8ms of heating, when applied to the corrugated surface.

To improve the uniformity of heating, the silver electrodes where extended in such a way that the heated area changed from trapezoidal into a rectangular shape. The silver had to be applied to the heating film after it was attached to the CaF_2 substrate, since it is not trivial to predict the final position of the film during the gluing process. The 3D CAD model of the plate was used to determine the two triangles that need to be painted.

Masking tape was then applied on the corrugation to assure that the paint would not cover additional areas. The result was that the film was now uniformly heated as can be seen in Figure 4.11.

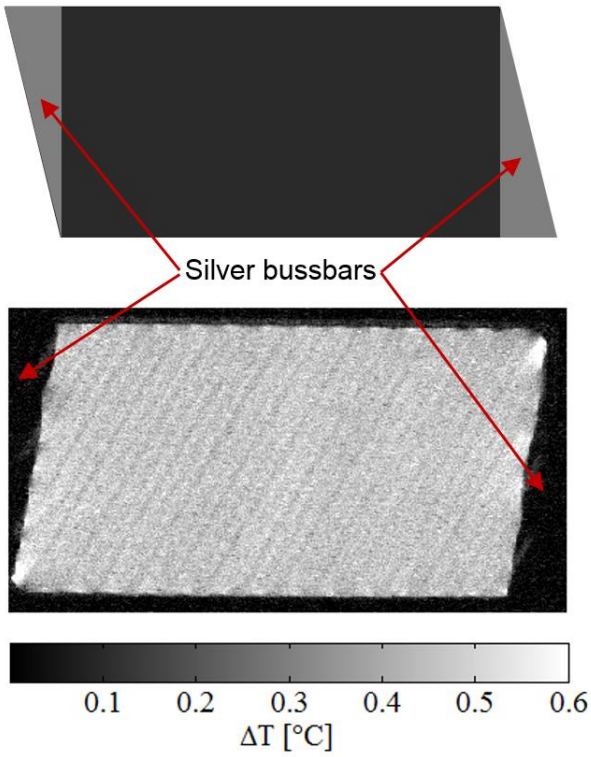

Figure 4.11: Heater film shape required to cover a rectangular PHE plate along with silver bussbars shaped to provide uniform heat flux (top); the temperature distribution on the PHE surface measured by the IR camera during transient heating of the film to test the heater uniformity (ΔT is the temperature difference between the heated and unheated state after 8 ms of heating (bottom).

One 600V 1.4A Sorenson power supply was used to power both heaters in series. When creating a mixed PHE arrangement with two plates that only differ in corrugation angle, the plate with the lower corrugation angle would have a lower resistance since the width of the heater film would be larger. To ensure that both plates receive equal amount of heat flux, a rheostat was connected to the CaF_2 plate heater in

parallel. Since the heated surface area of both plates were approximately identical, the resistance of the rheostat was adjusted that the total heating power to each plate was the same. The resistance of the rheostat was calculated as followed:

$$P_{CaF_2} = i_{CaF_2}^2 R_{CaF_2} = i_{Poly}^2 R_{poly} = P_{Poly} \tag{4.2}$$

$$i_{CaF_2} = \frac{R_{Rheo}}{R_{CaF_2} + R_{Rheo}} i; \;\; i_{Poly} = i \tag{4.3}$$

$$R_{Rheo} = \frac{R_{CaF_2}\left(R_{Poly} + \sqrt{R_{CaF_2} R_{Poly}}\right)}{R_{CaF_2} - R_{Poly}} \tag{4.4}$$

The heat generated could be removed by convection into the liquid or by substrate conduction. To estimate the heat lost into the substrate, the IR camera was used to measure the temperature of the black dots on the surface of the CaF_2 substrate as well as the conducting film between the dots (Figure 4.7). The heat lost into the substrate can be estimated using:

$$q''_{sub} = \frac{T_w - T_{dot}}{\frac{t_P}{k_P} + \frac{t_G}{k_G}} \tag{4.5}$$

The local thickness of the optical glue (t_G) could vary, however, and was not known. An overestimate of the substrate conduction can be obtained by assuming the thickness of the optical glue is zero, i.e, all the measured temperature difference occurs across the polyimide. Even with this assumption, the substrate conduction losses were found to be no more than 1% of the input heat flux. The local heat transfer from the heater to the liquid was obtained by subtracting this small conduction loss from the heat generated:

$$\dot{q}''_{fluid} = \dot{q}''_{gen} - \dot{q}''_{sub} \quad (4.6)$$

The local heat transfer coefficient can be calculated using

$$h_{fluid}(x,z) = \frac{\dot{q}''_{fluid}(x,z)}{T_w(x,z) - T_{fluid}} \quad (4.7)$$

where T_{fluid} is the local temperature obtained by linearly interpolating the thermocouple readings between the inlet and outlet of the test section.

The above analysis assumes the temperature within the electrically conducting film is uniform. The validity of this assumption can be shown using a simple conduction analysis. The conducting layer can be modeled as a plate with internal heat generation, an insulated boundary on one side (to approximate the conduction loss), and a specified temperature on the other (the temperature wall-fluid boundary). The maximum temperature difference within the film is given by

$$\Delta T_{max} = \frac{\dot{q}''' t_C^2}{2k_C} = \frac{\dot{q}'' t_C}{2k_C} \quad (4.8)$$

At the maximum heat flux used in the tests below ($\dot{q}''$=0.8 W/cm^2), the maximum temperature difference within the film was calculated to be ~0.02 °C. The temperature variation within the conducting film was thus much smaller than the temperature difference between the film and fluid and could be neglected for all cases.

4.4.2 Eliminating film heater defects

During the application of the 100RS200 film to the CaF_2 substrate the entrapment of air bubbles was inevitable. These areas needed to be avoided, when taking the average HTC for the entire plate. In addition the black dots and reference markings on the plate

should not be included as well. The black dots will have approximately the same temperature as the heater during adiabatic operation when the heater temperature is uniform. However, during steady state heating the heater surface temperature is not uniform and therefore heat spreading occurred within the multilayer (for more details see Appendix 8.2.2). Since this works focus is on the steady state HTC, it was decided to not include the black dots in the data analysis.

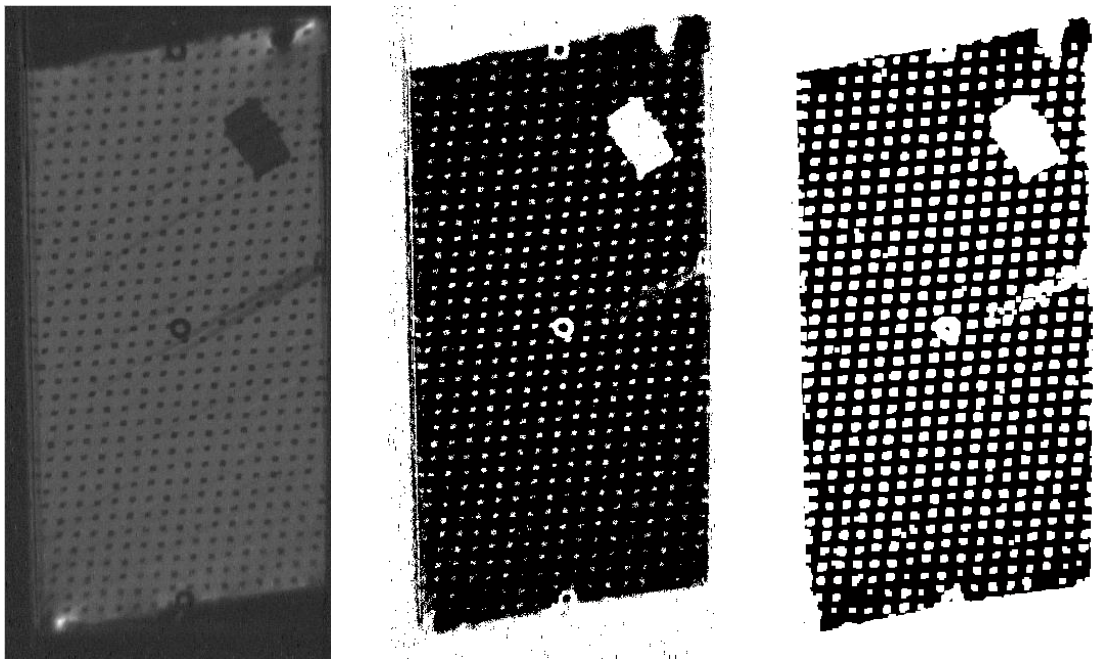

(a) (b) (c)

Figure 4.12: Initial image from the IR-camera after 8 ms of heating (a), detection of pixels that are below a certain threshold (b), identifying areas and filling the gaps in each area (c).

To identify the areas that were not included in the data analysis, a similar approach was used as in the previous section where the uniformity of the heat flux distribution of the heater was tested. Before each experimental campaign a step function in high heat flux was applied to the CaF_2 plate while recording the heater with

an IR-camera at a high framerate (>100 Hz). After 8 ms of heating areas of non uniform heat flux, markings on the plate, entrapped air bubbles in the epoxy layer and black dots became clearly visible as shown in Figure 4.12a. A Matlab algorithm was used to detect the location of each pixel that was below a certain threshold (Figure 4.12b). The final step was to fill and increase each area that was detect by the previous step.

4.4.3 Data reduction for Single phase flow

The Nusselt number within plate heat exchangers is usually defined as:

$$Nu = \frac{h_{fluid} d_h}{k_{fluid}} \tag{4.9}$$

where $d_h = 2b/\varphi$, and is a function of the Reynolds number, Prandtl number, and geometry factors. The Reynolds number is based on average flow velocity and a characteristic length:

$$Re = \frac{U d_h}{\nu} = \frac{\left(\frac{\dot{V}}{A}\right) d_h}{\nu} \tag{4.10}$$

where A is the cross sectional area perpendicular to the flow direction. The range of Reynolds numbers in the present study was between 300 and 3500. The Prandtl number for single phase flow was 7.8 and was assumed to be constant throughout the test section since the bulk fluid temperature only varied by about 3°C. The pressure drop is presented in terms of a Fanning friction factor:

$$f = \frac{dP}{dz} \frac{\rho d_h}{2G^2} \tag{4.11}$$

4.4.4 Data reduction for two-phase flow

Since all measurements are conducted under the steady state assumption, the calculation of HTC for the two-phase flow is identical to the single-phase regime. The liquid velocity however is commonly defined by the mass flux G

$$G = \frac{\dot{V}\rho}{A} \left[\frac{kg}{m^2 s}\right] \tag{4.12}$$

The dimensions of the PHE in this study are small compared to a standard PHE plate. Plates constructed from CaF_2 are comparatively costly and difficult to machine, necessitating a scaled down version of the PHE. Typically PHE are up to 10 times larger than our setup allows, therefore they have a much wider range of quality values within the channel during evaporation. This is visualized by the color pattern in Figure 4.13. It can be seen that the experimental plate would only be able to produce a much smaller quality range. However, by changing the inlet conditions of the test channel, it is possible to reproduce separately each section of a full PHE. Integrating over each subsection will give then the performance of a full plate heat exchanger, with the given geometrical parameters.

Although the used PHE is relatively small, the change in quality along the channel can be significant. To calculate the local quality during evaporation in the channel, it is necessary to include the change in pressure in the channel. Saturation temperature and liquid/vapor enthalpy are dependent on pressure which could change up to 20 kPa over the PHE.

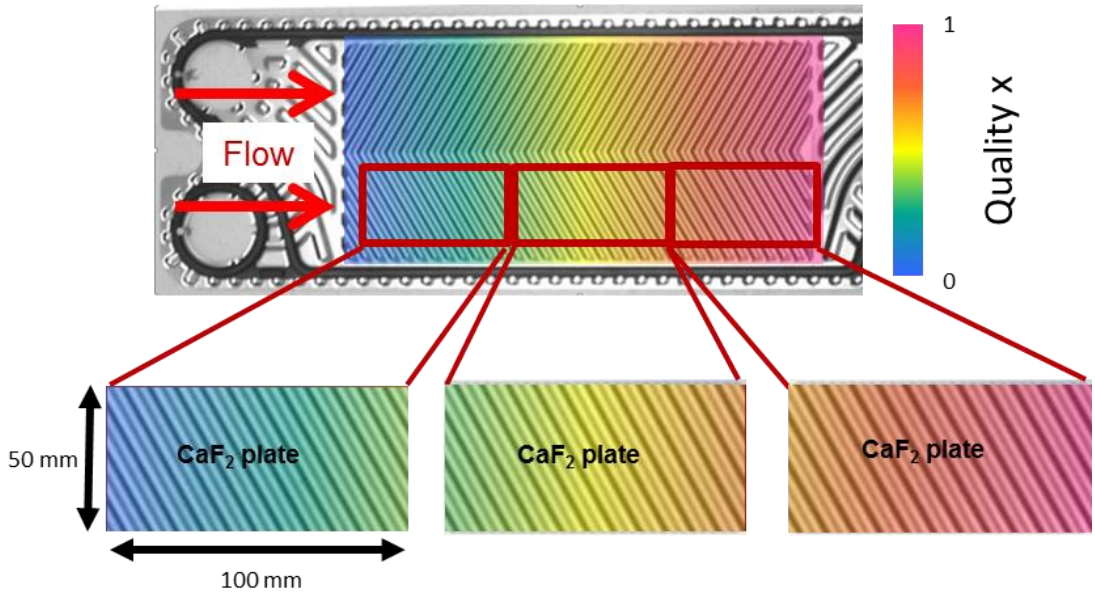

Figure 4.13: Visualization of change in quality along a PHE channel.

The quasi local liquid temperature gained from the seven thermocouples indicates the saturation temperature at any point in the channel, since the flow enters the test section at saturation. This means it is possible to write the energy balance across a small channel element only as a function of saturation temperature as is shown in Figure 4.14.

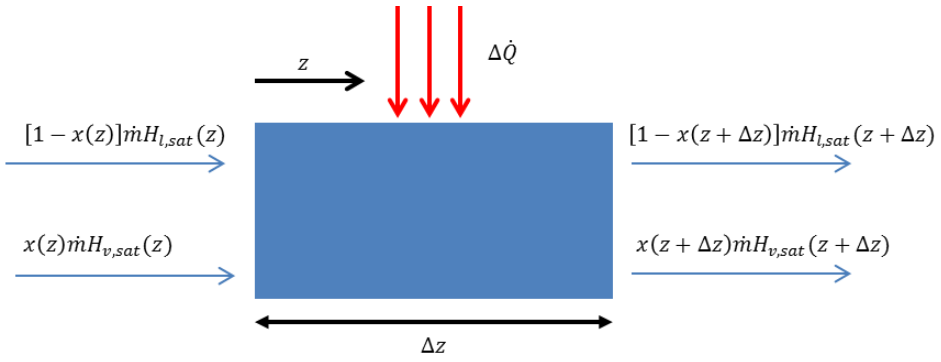

Figure 4.14: Energy Balance across a channel section, to calculate the change in quality

Writing out the energy balance and solving the equality for $x(z + \Delta z)$ will result in the following equation:

$$x\left(z+\Delta z\right)=\frac{\left[\frac{\dot{Q}}{\dot{m}}+\left[1-x\left(z\right)\right]H_{l,sat}\left(z\right)+x\left(z\right)H_{v,sat}\left(z\right)-H_{l,sat}\left(z+\Delta z\right)\right]}{H_{v,sat}\left(z+\Delta z\right)-H_{l,sat}\left(z+\Delta z\right)} \quad 4.13$$

Since the local temperature and pressure were known from the five thermocouples and five pressure taps along the PHE, the local values of the liquid and vapor enthalpy $H_{l,sat}$ and $H_{v,sat}$ could be determined. A marching procedure was then used to calculate the local quality along the test section.

Before entering the test section, the liquid was heated in the preheater to achieve the desired quality at the inlet of the test section. The total power input to the preheater was calculated from the following overall energy balance:

$$\dot{Q}=\dot{m}c_p\left(T_{sat}-T_i\right)+\dot{m}x_oH_{lv} \quad 4.14$$

where c_p was evaluated at the average of the preheater inlet and saturation temperature at the outlet of the preheater, and H_{lv} was computed at the preheater outlet condition.

As described earlier, the pressure data were obtained using an absolute pressure transducer to measure the saturation pressure close to the inlet of the PHE. A differential pressure transducer combined with four valves were used to measure the pressure drop along the PHE at four locations. The total pressure drop measured by the differential pressure transducer within the PHE was the sum of three components:

$$\Delta P_{tot,meas}=\Delta P_{g,meas}+\Delta P_f+\Delta P_a \quad 4.15$$

The measured gravitational pressure drop accounted for the pressure due to the liquid head included in the differential transducer measurement:

$$\Delta P_{g,meas} = -\left(\rho_l g D_P - g D_P \rho_m\right) \quad 4.16$$

which was reduced to

$$\Delta P_{g,meas} = D_P g(\rho_m - \rho_l) \quad 4.17$$

where D_P was the distance between two pressure taps and ρ_m was the mean two-phase density within the PHE defined by the homogeneous model as

$$\rho_m = \left[\frac{x}{\rho_v} + \frac{1-x}{\rho_l}\right]^{-1} \quad 4.18$$

This distance D_P has to be accounted for since the tubes leading to the differential pressure transducer are completely filled with liquid and have a density that is different from the two-phase mixture in the PHE channel. The pressure drop due to the acceleration during evaporation was estimated according to

$$\Delta P_a = G^2 \Delta x \left(\frac{1}{\rho_v} - \frac{1}{\rho_l}\right) \quad 4.19$$

The frictional pressure drop ΔP_f was computed from the above set of equations which allowed for the calculation of the actual pressure drop in the PHE

$$\Delta P_{tot} = \Delta P_g + \Delta P_f + \Delta P_a \quad 4.20$$

where ΔP_g represented the gravitational pressure drop within the PHE and was defined as:

$$\Delta P_g = D_p g \rho_m \quad 4.21$$

The acceleration pressure drop was of the order of 0.01% of the total pressure drop and could be neglected. Hence, the pressure drop can be assumed to be linear within the PHE channel since the frictional pressure gradient was fairly constant over the short PHE length. The four differential pressure transducer measurements were used to create a linear fit to the experimental data, and the slope of the linear fit was used to determine the pressure drop. The uncertainty of the pressure drop was based on the goodness of the linear fit and is discussed in the last section of this chapter.

4.5 Uncertainty analysis and preliminary validation

The uncertainties and ranges of the instruments used in this work are listed in Table 4.4. The overall uncertainty (with 95% confidence) for the friction factor, Nu, Re and HTC were computed using the error-propagation formula of Taylor (1982):

$$\sigma_R = \left[\left(\frac{\delta R}{\delta v_1}\delta\sigma_1\right)^2 + \left(\frac{\delta R}{\delta v_2}\delta\sigma_2\right)^2 + \cdots \left(\frac{\delta R}{\delta v_n}\delta\sigma_n\right)^2\right]^{0.5} \qquad 4.22$$

Where σ_R is the overall uncertainty of the value R which is a function of the variable v_1 to v_n having each an uncertainty of σ_1 to σ_n respectively. As mentioned before the error for the pressure drop within the test section was calculated based of the goodness of the linear fit of 5 pressure measurements within the PHE. The linear fit of the pressure distribution inside the PHE would give the following equation:

$$P(z) = bz + a \qquad 4.23$$

where $b = \frac{dP}{dz}$. The uncertainty of b is defined by:

$$\sigma_b = \sigma_P \sqrt{\frac{N}{\Delta}} \tag{4.24}$$

where N is the number of data points and σ_P is defined as:

$$\sigma_P = \sqrt{\frac{1}{N-2}\sum_{i=1}^{N}(P_i - a - bz_i)^2} \tag{4.25}$$

with

$$\Delta = N\sum z^2 - (\sum z)^2 \tag{4.26}$$

In addition the error-propagation are shown by the error bars on the figures. The average uncertainty of the local heat transfer coefficient was calculated to be ±12% and are shown by the error bars on the plots.

	Model	Range ($v_1 \dots v_n$)	Uncertainty ($\sigma_1 \dots \sigma_n$)
Flowmeter	Omega FLR 1000	400-5000 ml/min	±50ml/min
Flowmeter	Omega FLR 1000	0-500 ml/min	±5ml/min
Pressure transducer	Omega PX309-030AV	0-200000 Pa	±500 Pa
Differential Pressure Transducer	Validyne DP15	0-22000 Pa	±220 Pa
Thermocouple	T-type	-200-350°C	±0.2°C
IR-Camera	FLIR5600	30-80°C	±0.2°C

Table 4.4: Uncertainties of the instruments used in this study

An overall energy balance between the energy input to the heaters and the sensible heating of the liquid (measured using the 7 thermocouples, flow meter, and fluid properties) was carried out. Figure 4.15 shows the results of the energy balanced measured for forty experiments with different combinations of mass rate and heat fluxes. The energy balanced was calculated the following way:

$$\dot{Q}_{heater} = 2A_{heater}q'' \tag{4.27}$$

$$\dot{Q}_{liquid} = \dot{m}c_p\Delta T \tag{4.28}$$

$$\frac{\dot{Q}_{heater} - \dot{Q}_{liquid}}{\dot{Q}_{heater}} = \Delta\dot{Q} \tag{4.29}$$

That means if $\Delta\dot{Q} > 0$ heat is lost to the surroundings and values for $\Delta\dot{Q} < 0$ are due to the measurement uncertainty. On average, the balanced agreed to within ±11% or better for all flow rates.

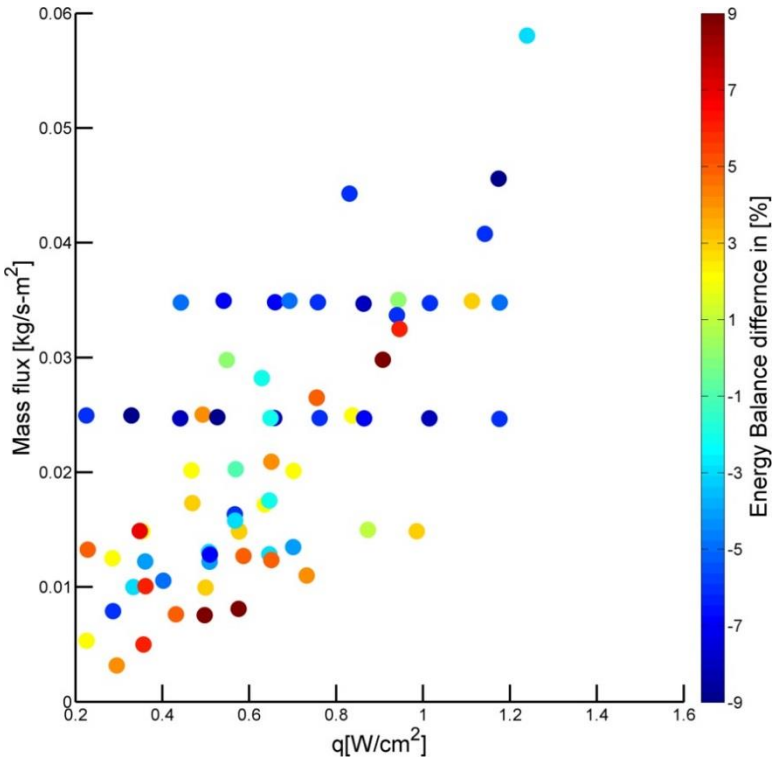

Figure 4.15: Result of the energy balance calculation for several experiments with different flow parameters and heat fluxes.

To test if the calibration was still valid during an experimental campaign, periodic adiabatic measurements between heated runs were recorded, where the

calculated temperature of the heater surface needed to match the temperature of the fluid measured by the TCs. This data was analyzed in real time, so potential adjustments in the calibrations could be performed before taking more data. Figure 4.16 shows the output of the real time data reduction during an adiabatic test run. If the temperature deviation between the heater and the fluid was above the uncertainty, the calibration had to be repeated.

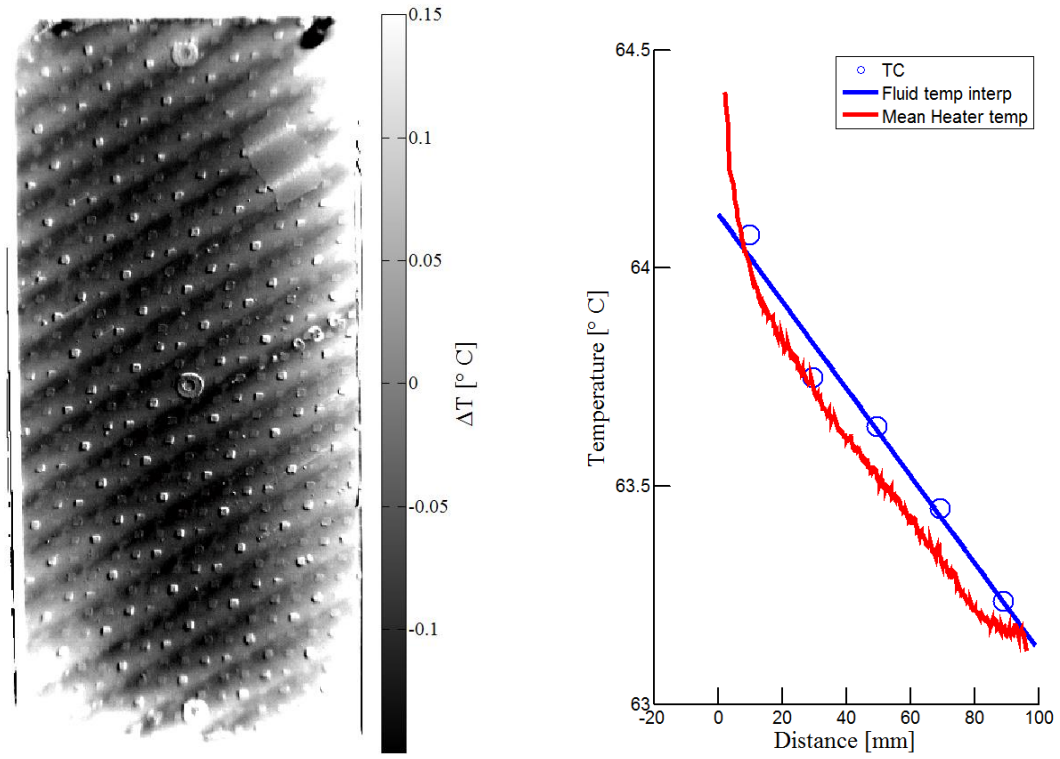

(a) (b)

Figure 4.16: Temperature difference between heater and fluid during adiabatic two-phase operation, (a) Temperature map of the entire PHE plate, (b) over the width averaged heater temperature vs. fluid temperature interpolated using the 5 TCs that are placed in the flow channel.

5. Single Phase flow results

The measured pressure drop and heat transfer data were compared with the relatively recent pressure drop and heat transfer correlations listed in Table 5.1. These correlations were selected since the geometry and parameter range upon which they were based were similar with the current study.

Reference	$\beta°$	φ	D_e $[mm]$	Re	Pr (Fluid)	Correlation
Thonon et al. [11]	15, 30, 45, 60			50 -15000		$\mathrm{Nu} = C(\beta)\mathrm{Re}^{m(\beta)}\mathrm{Pr}^{n}$ $f = E(\beta)\mathrm{Re}^{p2(\beta)}$
Muley and Manglik [10]	30, 45, 60, 75	1.29	5.08	600-10000	2.0-6.0 (Water)	$\mathrm{Nu} = C(\beta)D(\beta)\mathrm{Re}^{p1(\beta)}\ \mathrm{Pr}^{0.33}$ $f = E(\beta)F(\varphi)\mathrm{Re}^{p2(\beta)}$
Talik et al. [58]	60	1.22	4.65	1450-11460	2.5-5.0 (Water)	$\mathrm{Nu} = 0.248\mathrm{Re}^{0.7}$ $f = 0.3323\mathrm{Re}^{-0.042}$
Okada et al. [7]	30-75			700-25000	(Water)	$\mathrm{Nu} = C_1\mathrm{Re}^{\mathrm{C}_2}\ \mathrm{Pr}^{0.4}$
Heavner [8]	0-67			400-10000	3.3-5.9 (Water)	$\mathrm{Nu} = C_1(\varphi)^{1-m}\mathrm{Re}^{m}\ \mathrm{Pr}^{0.5}$ $f = C_2(\varphi)^{p+1}\mathrm{Re}^{-p}$
Focke et al. [9]	0-90	1.46	10	90 -50000	(Distilled Water)	$\mathrm{Nu} = C_1\mathrm{Re}^{m}\ \mathrm{Pr}^{0.5}$ $f = C_2\mathrm{Re}^{p}$
Kumar [59]	30, 40, 45, 60	1.17		>100	(Water)	$\mathrm{Nu} = C_1\mathrm{Re}^{m}\ \mathrm{Pr}^{0.33}(\mu/\mu_w)^{0.17}$ $f = C_2\mathrm{Re}^{p}$
Present Study	60, 45 65, 45	1.25 1.17	4 2	300 -3500	7.8 (HFE 7100)	

Table 5.1: Single phase pressure drop and heat transfer correlations appropriate for the current geometry.

5.1 Pressure Drop

The pressure drop along the test section for various Re is shown on Figure 5.1. This data was obtained by sampling the differential pressure transducer at 500 Hz for 5 s, which was enough for the sampling uncertainty to become negligible compared with other uncertainties. The linear fits to the data (solid lines) intercept the ordinate at

mostly positive values, likely due to higher pressure losses in the entry region. It is seen that the pressure drop is linear beyond the first downstream pressure tap, however, indicating a hydrodynamically fully developed flow.

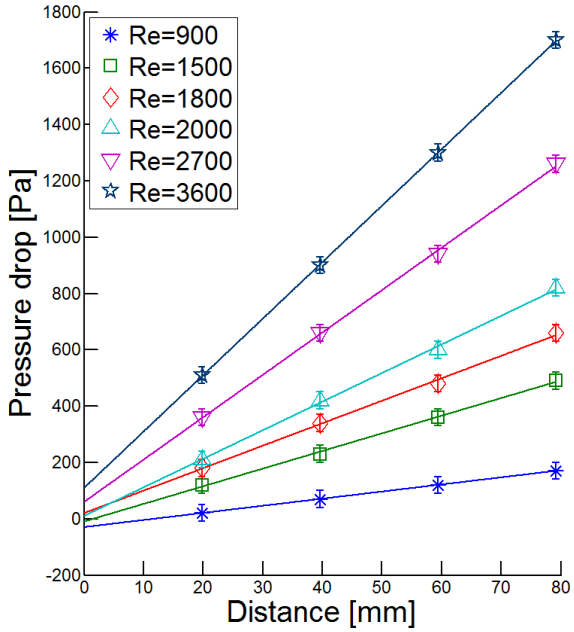

Figure 5.1: Pressure drop along the L5.7A1.0B60-60 PHE at various Re. Pressure drop is measured between the furthermost upstream tap (z=0 mm) and a downstream tap (z=20 mm, 40 mm, 60 mm, or 80 mm).

5.1.1 Single Phase friction factor measurements

Comparison of the friction factor measured using the pressure data, with the correlations in Table 5.1 are shown in Figure 5.2 and Figure 5.3. As can be seen from Table 5.1 most correlations depend only on Reynolds number, some include the corrugation angle β. In most cases each equation gives a different constant for each common angle. For the L3.7A0.5B65-65 geometry the constants were chosen that correspond to a 60° angle since that is the closest angle for a standard PHE. The only

equations that incorporate all geometrical factors is the ones from Muley and Manglik [10].

Figure 5.2a shows the friction factor for the L5.7A1.0B60-60 and L5.7A1.0B60-30 geometry. The data are bracketed by the proposed correlations, but agree best with Kumar [59]. The L5.7A1.0B60-60 data follows the downward trend of the friction factor with increasing Reynolds number as was predicted by Muley and Manglik [10] Focke et al. [9] and Kumar [59].

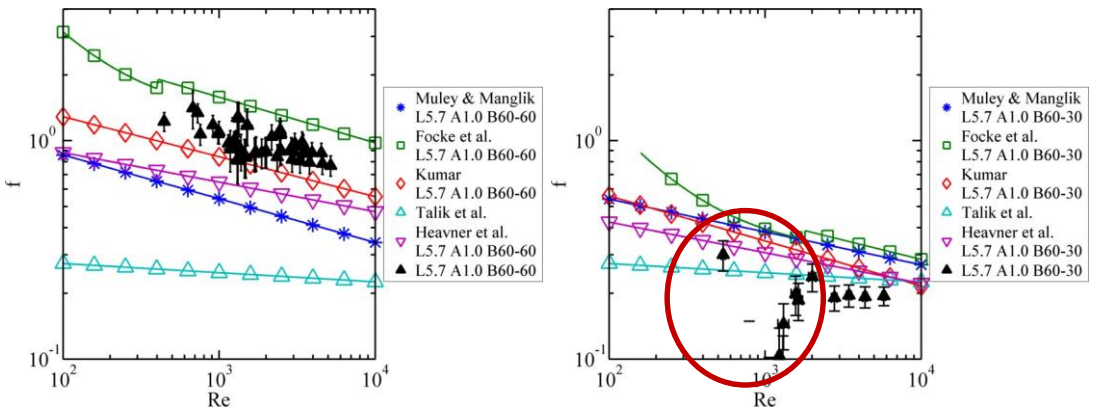

(a) (b)

Figure 5.2: Comparison of friction factor correlations from other studies with the results of the (a) L5.7A1.0B60-60 and (b) L3.7A1.0B60-30, values that are within the red circle need to be ignored since the measurement uncertainty was too high for these low Reynolds numbers.

Figure 5.2b shows the frictional pressure drop of the L5.7A1.0B60-30 PHE. The frictional pressure drop decreased by nearly a factor of magnitude when compared with the L5.7A1.0B60-60 PHE. Therefore, the pressure drop at low Reynolds numbers was too small to be reliably measured by the differential pressure transducer. Friction factor values that were measured below a Reynolds number of Re=2000 must be ignored since the overall pressure drop over the entire PHE was lower than the uncertainty of the

pressure transducer. The values in question are circled in Figure 5.2b. However, for Reynolds number above 2000 a clear trend could be detected. The data agrees very well with the prediction method proposed by Talik et al. [58]. The correlations that were able to follow the trend for the L5.7A1.0B60-60 plate were not able to do the same for the L5.7A1.0B60-30 plate even though the correlations were dependent on the corrugation angle. This is likely due to the fact that most researchers measured the pressure drop over the inlet and outlet distributor, which becomes more significant for softer plates.

Figure 5.3 shows the pressure drop for the L3.7A0.5B65-65. The effect of the small change in chevron angle β of 5° (from 60° to 65°) has less influence on the hydraulic performance, therefore with the exception of Muley and Manglik [10] the correlations are the same as for the L5.7A1.0B60-60 plate. As seen before, the correlations are able to bracket the data, but fail to have a good agreement for both tested corrugation angles. The data agrees best with the correlation of Muley and Manglik [10] for both cases. The downward trend of the friction factor for both geometries was predicted well by the correlations.

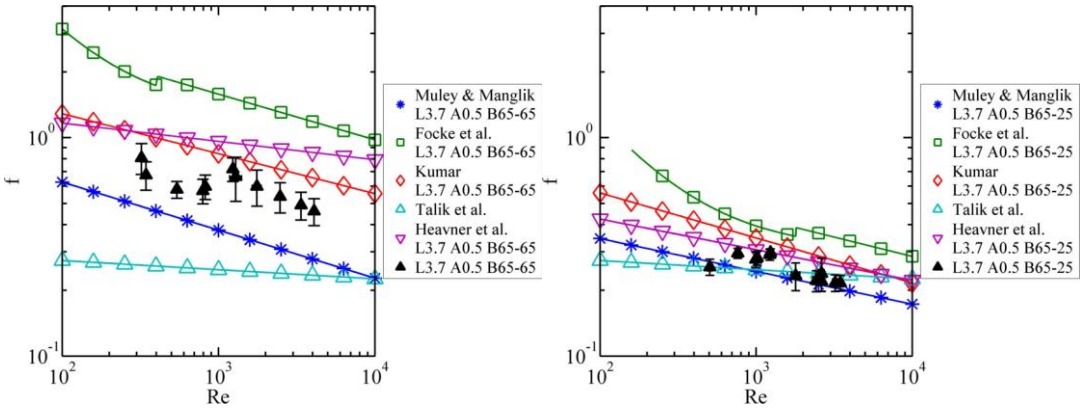

(a) (b)

Figure 5.3: Comparison of experimental friction factor of the L3.7A0.5B65-65 data with other studies.

Figure 5.4 shows the friction factor for all geometries in one plot. Muley and Manglik [10] included the dependence on the surface enlargement factor φ. Their correlation suggested that L5.7A1.0B60-60 and L5.7A1.0B60-30 (with φ=1.25) would have a higher friction factor than L3.7A0.5B65-65 and L3.7A0.5B65-25 (with φ=1.17), which is qualitatively consistent and clearly visible with the observed trends for the hard plates. Similar results were also observed by Okada et al. [7] who observed a pressure drop decrease with increasing corrugation wavelength and amplitude. When changing the corrugation from L10A2.3B60-60 to L15A3.4B60-60 the pressure drop decreased by a factor of 2.

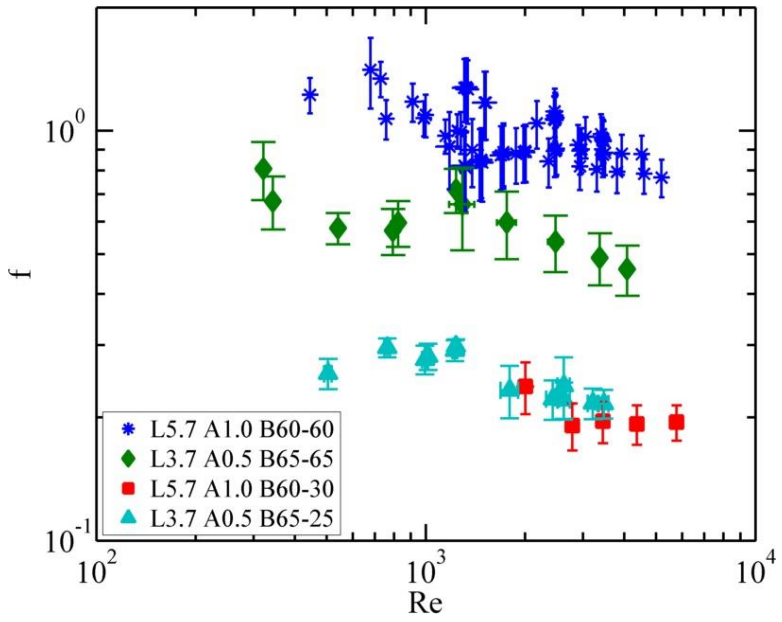

Figure 5.4: Comparison of experimental friction factor for all tested geometries.

For the two soft plates the effect of enlargement factor is less prominent. This could be due to the shift in flow direction when using a mixed plate arrangement. When two identical PHE plates are used the corrugation pattern runs parallel with the bulk fluid direction, however if one plate has a different corrugation angle the corrugation pattern is shifted by an angle α which is defined as followed:

$$\alpha = \frac{\left|\beta_{Plate_1} - \beta_{Plate_2}\right|}{2} \qquad 5.1$$

Therefore, the L5.7A1.0B60-30 and L3.7A0.5B65-25 have a shift angle of 15° and 20° respectively, which could produce a higher pressure drop for the L3.7A0.5B65-25 plate. In the industry where, in general, larger plates are used, it is assumed that this effect is negligible, however for our experiments only a small PHE was implemented which resulted in uneven mixing that will be later shown during HTC measurement. The non-uniform heat flux distribution was more pronounced on the L3.7A0.5B65-25 and is an indicator for higher pressure drop due to uneven liquid distribution. Further

tests on how a mixed plate configuration compares to a pure one are needed, and have not been carried out yet by other researchers.

5.1.2 The effect of Inlet/Outlet port and herringbone pattern

The pressure loss over inlet/outlet flow distributor within the PHE test section along the pressure drop over the entire PHE is plotted in Figure 5.5, for L5.7A1.0B60-30 PHE and L3.7A0.5B65-65 PHE. As can be seen, the port pressure drop plays a significant role in the overall pressure drop, especially with low corrugation angle plates. The elevated pressure drop at the outlet compared to the pressure drop at the inlet is due to the fact that different fittings were used at the inlet and outlet of the test section. In addition the predicted pressure drop over the port is plotted which is defined by Shah and Focke [44] as:

$$\Delta P_{port} = 1.5(\frac{\rho_l v^2}{2}) \qquad 5.2$$

The data shows that the predicted port pressure drop highly under predicts the measured data. Flow distributors can easily take up 30% of the total length of the PHE, yet in most cases they are neglected in the data reduction, allowing for significant errors in friction factor and Nu measurement.

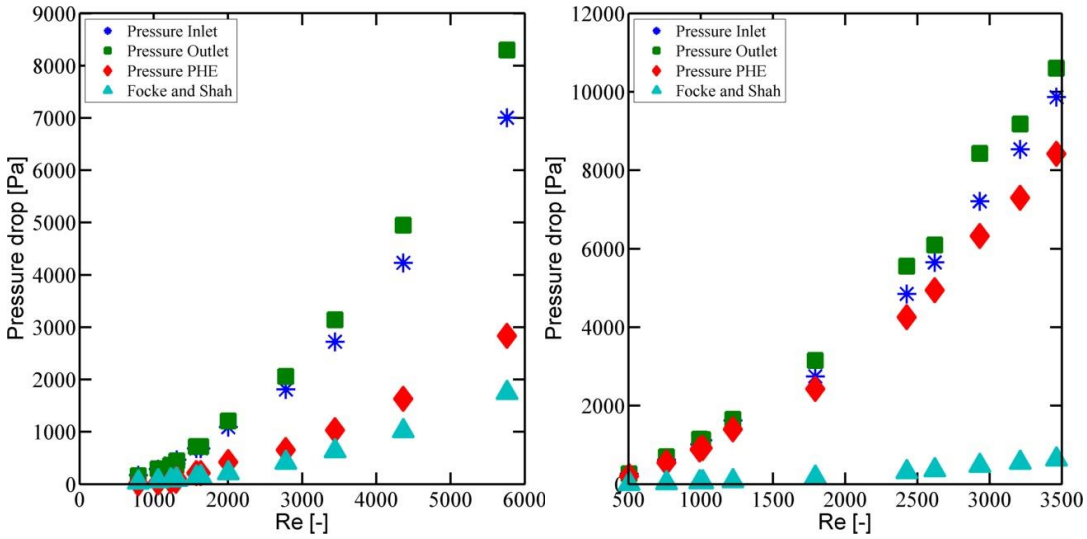

Figure 5.5: Pressure drop over the inlet and outlet compared with the frictional pressure drop within the (a) L5.7A1.0B60-30 PHE and (b) L3.7A0.5B65-65 PHE.

Another source of inconsistencies between data sets, is the arrangement of the corrugated pattern. The corrugated pattern is usually stamped into the PHE plate as a herringbone pattern (as can be seen in Figure 2.1), since the manufacturing process becomes easier and fouling can be reduced. In our application we decided against the herringbone pattern and chose an oblique washboard pattern, since it was easier to machine into the CaF_2 substrate and it made the attachment of the film heater significantly easier. In addition, it is well known that the herringbone configuration contributes little to none to the local heat transfer of a PHE cell that is located away from the herringbone center. Most correlations were established from experiments using plates with herringbone patterns. To investigate the effect of the pattern structure on pressure drop, a herringbone pattern was machined into two polycarbonate plates and adiabatic pressure measurements were taken. The results are listed in Figure 5.6.

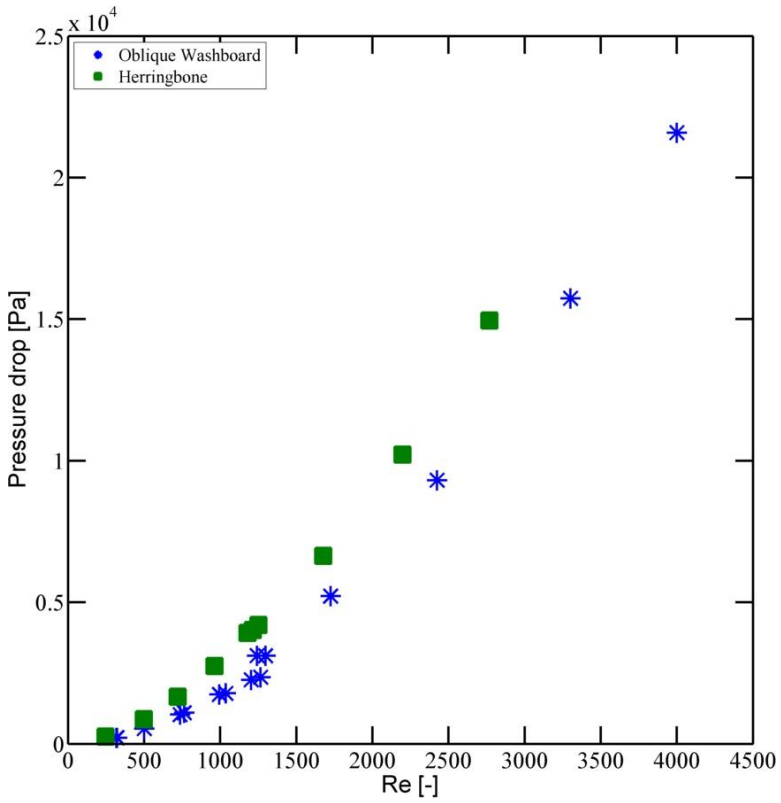

Figure 5.6: Single-phase pressure drop for the oblique washboard geometry and herringbone pattern at different Reynolds number for the L3.7A0.5B65-65 PHE.

The frictional pressure drop of the herringbone pattern is (up to 25%) higher compared to the oblique washboard pattern. The V-shape of the herringbone pattern, interrupts more frequently the viscous boundary layer at the center of the plate due to the abrupt transition from the minimum to the maximum plate spacing, which can be observed in Figure 5.7. Additionally, the local cross and swirl flows around crest and furrows at the center of the plate in turn produce more turbulence. The increased local mixing would increase the local HTC and therefore also the overall HTC as well. This effect would become less significant with wider plates for the local HTC, however the overall pressure drop and heat transfer data would be affected and is another reason why most correlations do not agree with each other well.

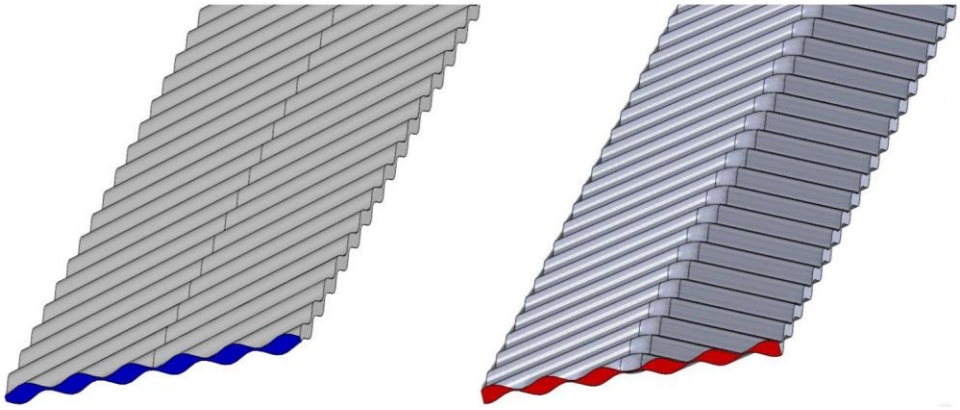

(a) (b)

Figure 5.7: Transversal cross section of two sinusoidal plate heat exchanger for the L3.7A0.5B65-65 PHE: (a) Oblique washboard, (b) herringbone pattern.

5.2 Area averaged HTC

To examine if the flow was thermally fully developed, the heat transfer coefficients were plotted along the direction of the stream and cross-stream directions at the locations shown in Figure 5.8a. It can be seen that the flow became thermally fully developed along the streamwise direction after a relative short entry length (y>15 mm) (Figure 5.8b, top). Similar entry lengths were observed at higher Re values. The heat transfer coefficient in the cross-stream direction was also very regular within the central 30 mm of the plate (Figure 5.8b, bottom). Irregularities in the horizontal temperature distribution as observed by Gherasim et al. [17] were not measured in our experiments for pure PHE arrangement, and may be due to the inlet distribution system that was added to our test section. In addition Figure 5.8a clearly shows the contact points with low HTC and the extended silver contacts (Figure 5.11) with high HTC due to the non-existing heat flux. This behavior was observed for the pure PHE arrangements (L5.7A1.0B60-60 and L3.7A0.5B65-65).

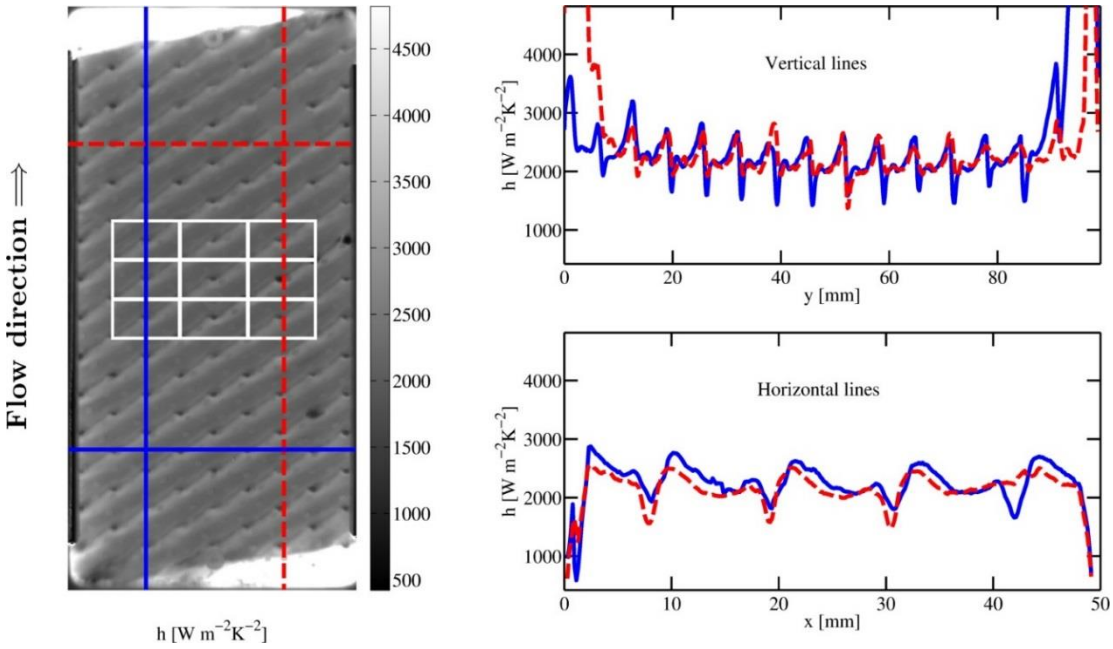

(a) (b)

Figure 5.8 Horizontal and vertical variation of heat transfer coefficient at Re=1700 and heat flux of 0.45W cm^{-1} for the L5.7A1.0B60-60 PHE. The white rectangles indicate the areas of the nine unit cells that were used to calculate the local heat transfer distribution within a unit cell.

Figure 5.9 shows the HTC distribution for the mixed plate arrangement L3.7A0.5B65-25. As can be seen the HTC distribution is not as good as with the pure arrangement. As discussed in Section 5.1.1 the bulk flow velocity vector is shifted by an angle α to the PHE (Figure 5.9a). The unsymmetrical plate arrangement produces a larger entry length and irregularities in HTC can be observed on the left and right boundary, however the center of the plate marked with a white box in Figure 5.9a provides a relative uniform area regarding HTC. This area was used to create the overall HTC of the PHE by averaging all the HTC values within that area. This perimeter was also used for all other PHE configuration, to eliminate potential boundary effects.

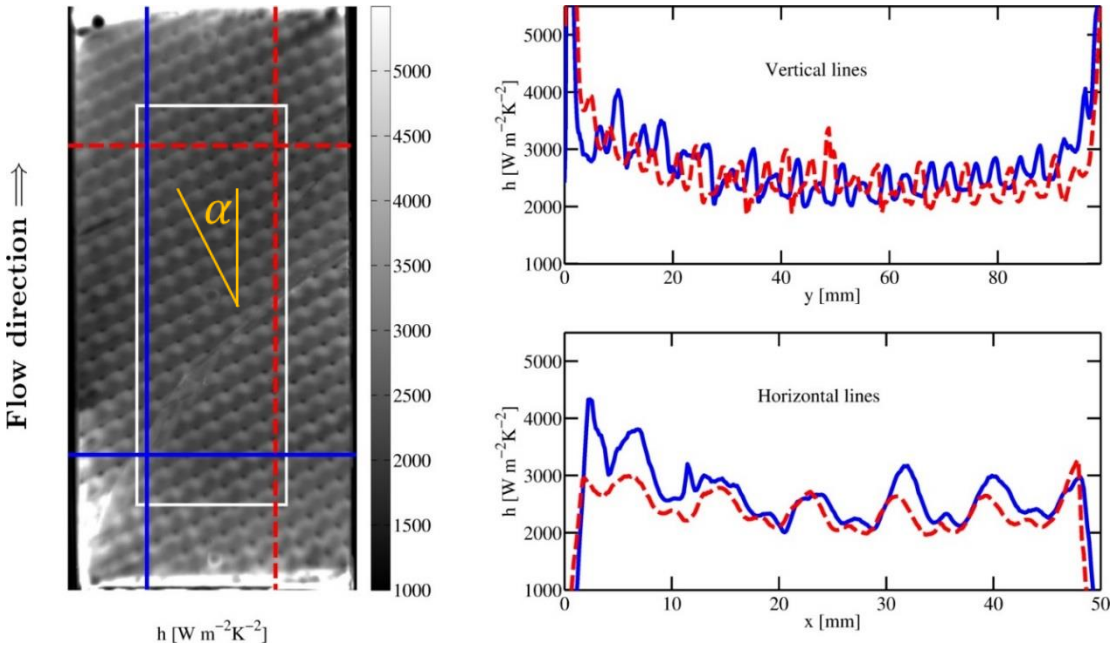

(a) (b)

Figure 5.9 Horizontal and vertical variation of heat transfer coefficient at Re=1300 and heat flux of 0.45W cm^{-1} for the L3.7A0.5B65-25 PHE. The white box representing the area that was used for the overall HTC computation.

The average heat transfer in the fully developed region was measured in the range of 300<Re<6000 and compared with the correlations listed Table 5.1. The results are shown in Figure 5.10 and Figure 5.11. As it was the case with the friction factor, the correlations are able to predict the trend of Nu with increasing Re and changes in corrugation angle and corrugation geometry. The current data is bounded by the correlations, but agrees best with Thonon et al. [11]

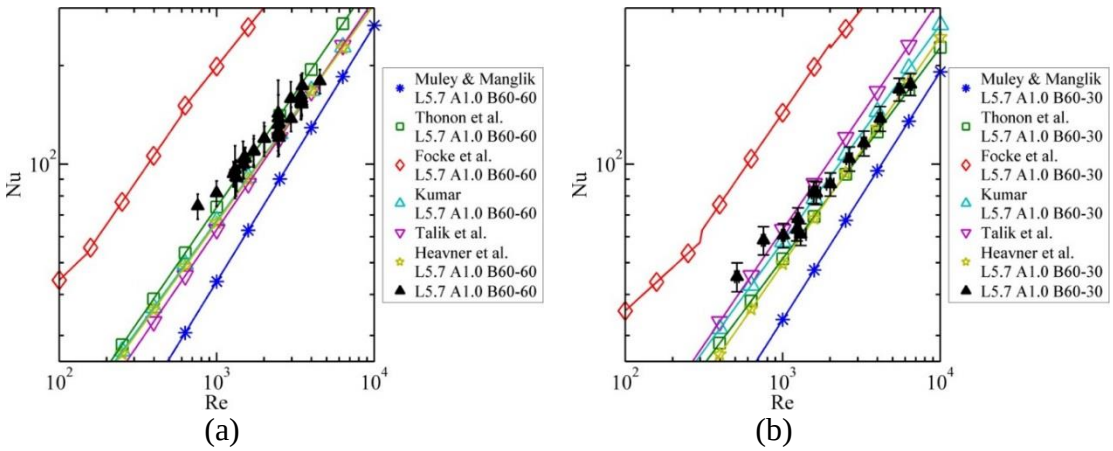

Figure 5.10: Comparison of experimental Nusselt number of the (a) L5.7A1.0B60-60 and (b) L5.7A1.0B60-30 data with other studies.

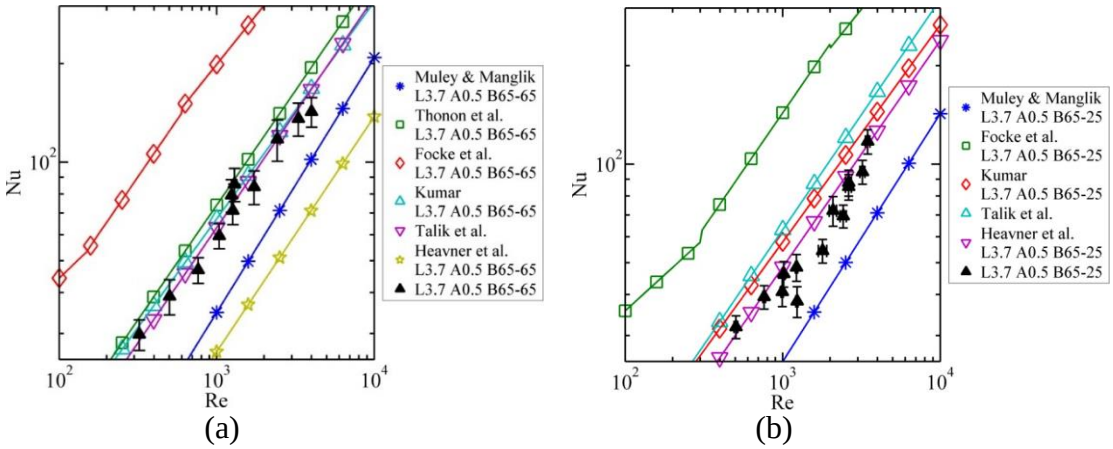

Figure 5.11: Comparison of experimental Nusselt number of the (a) L3.7A0.5B65-65 and (b) L3.7A0.5B65-25 data with other studies.

Figure 5.12 summarizes all Nu numbers measured during single-phase flow. As expected, the two hard plates produced higher Nu than their soft counter plate. The L5.7A1.0B60-60 produces the highest Nu for low Re and similar Nu as the L3.7A0.5B65-65 for higher Re.

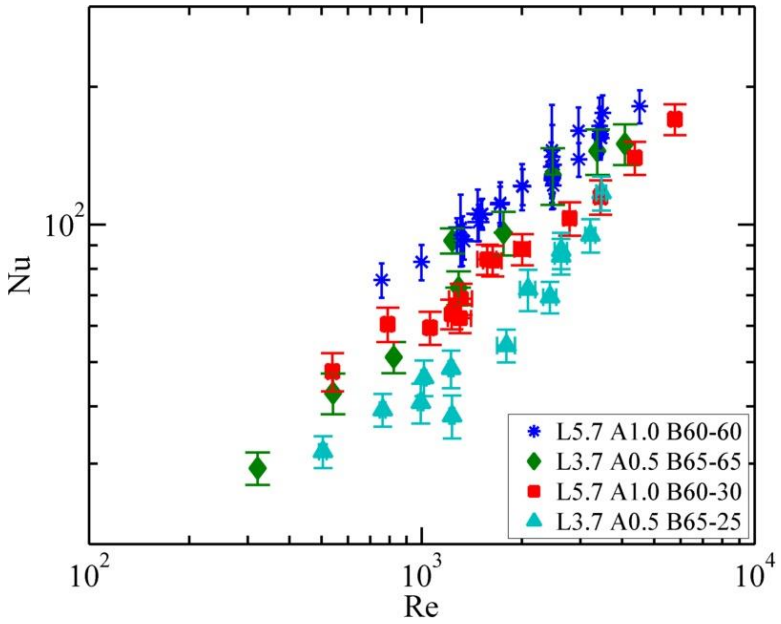

Figure 5.12: Heat transfer data from all geometries.

5.3 Local Heat transfer Measurements

The time average heat transfer distribution within a unit cell of the PHE was obtained (Figure 5.13) by averaging the data from nine cells in the fully developed region shown in Figure 5.8. When data was not available due to the presence of black dots or other defects in a given cell, the data from that cell was not included in the averaging. The maximum heat transfer coefficient occurs just upstream of a contact point, and higher heat transfer is seen on the upstream side of a corrugation as would be expected since the fluid strikes this surface. The minimum heat transfer occurs at the contact point, and generally lower heat transfer occurs on the downstream side of a corrugation.

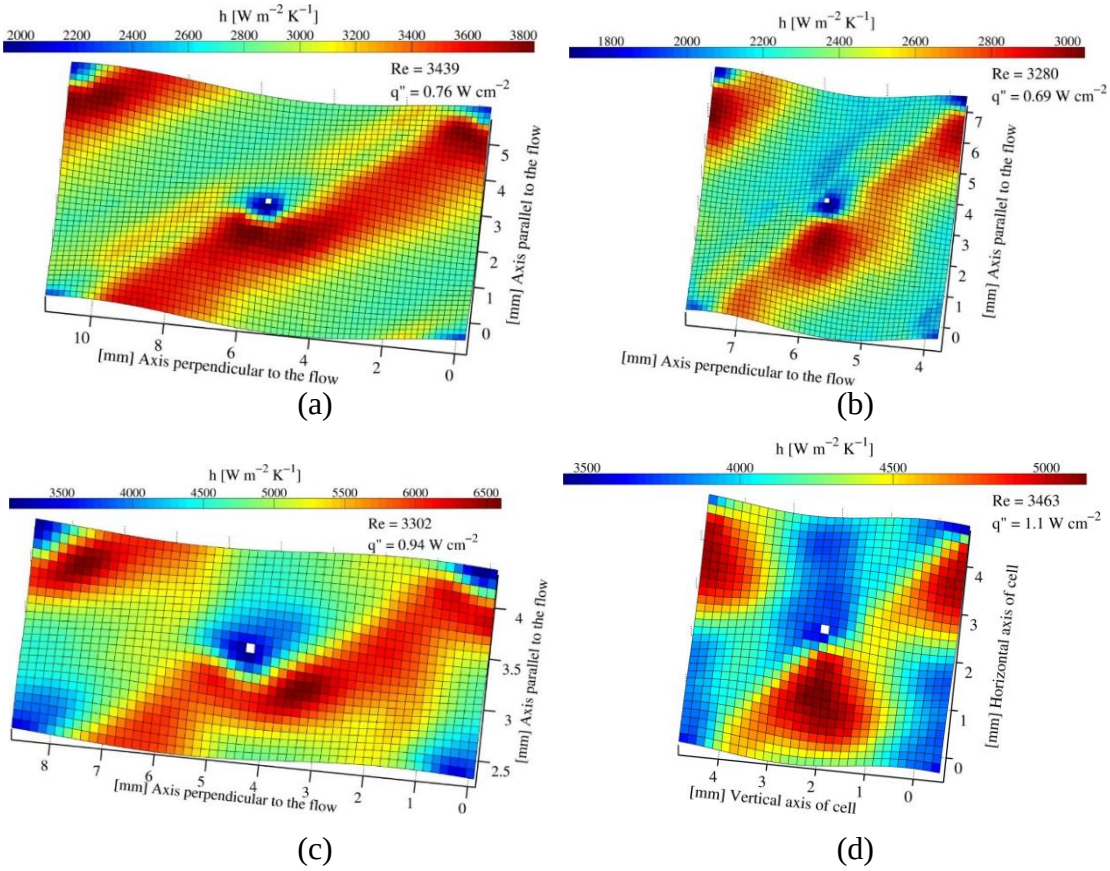

Figure 5.13: HTC distribution within a representative cell for the (a) L5.7A1.0B60-60 PHE, (b) L5.7A1.0B60-30 PHE, (c) L3.7A0.5B65-65 PHE, and (d) L3.7A0.5B65-25 PHE.

The location of the maximum and minimum heat transfer within a representative cell seen by Stasiek et al. [14], Gaiser and Kottke [13], and Freund and Kabelac [16] (see Figure 3.1) were consistent with our observations. However, the ratio of the maximum to minimum heat transfer in these studies were much higher than the ratios of ~2 observed in all of our data (300<Re<6000). For example, Stasiek et al. [14] and Gaiser and Kottke [13] observed ratios of ~4 and Freund and Kabelac [16] observed a decrease in this ratio from ~4 to ~2 as Re increased from 1060 to 3980. Stasiek et al. [14] claimed that the central region of the upstream corrugation side provided very little heat

transfer, which was inconsistent with the current data and that of Freund and Kabelac [16].

It is unclear why our heat transfer data was much more uniform than observed by others. One possible explanation of the discrepancy between our measured heat transfer coefficient ratio and the values stated in previous work, is the fact that one plate was covered with small pieces of tape at each contact point, thus preventing an electrical contact between both plates. The tape acts as an insulator and can allow the heat to spread within the material rather than heating up the film. In a real PHE the theoretical convective heat transfer at the contact point should be zero, since the temperature gradient across the contact area is not present assuming that the liquids have the same temperature on each side of the contact point. Therefore, the local HTC at the touching point is only dependent on conduction within the plates and thus depending on plate material and thickness.

To test how the heat transfer distribution changes with flow rate, HTC spreading in the PHE cell for different Reynolds numbers, was created by a graphical representation of the distribution of the HTC data (Figure 5.14). Each pixel was first normalized by using the average HTC value over the entire cell and then the cell was divided into one hundred equally spaced bins with their starting and end value being the minimum and maximum normalized HTC value in the cell, respectively. The results show that the quantitative local heat transfer distribution does not change with different Re. All geometries have a global maximum that is slightly lower than the average HTC of the cell. This peak represents the area in the trough region, which can be clearly seen for all geometries in Figure 5.13. A local maximum can be observed which is higher

than the average and accounts for the high HTC areas located near the touching point and on the downstream side of the crest.

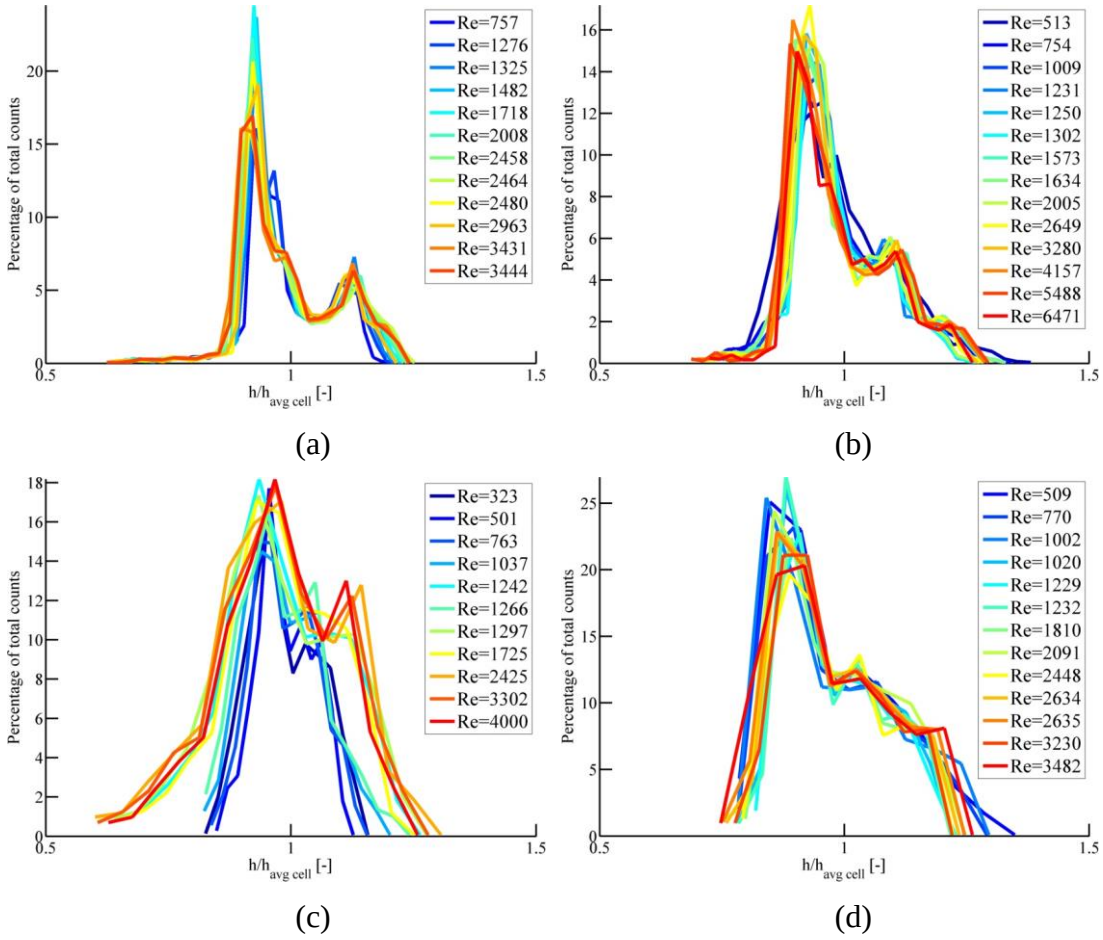

Figure 5.14: HTC distribution over a range of Re: (a) L5.7A1.0B60-60 PHE, (b) L5.7A1.0B60-30 PHE, (c) L3.7A0.5B65-65 PHE, and (d) L3.7A0.5B65-25 PHE

The standard deviation in heat transfer between the 9 cells, is shown in Figure 5.15 for all tested PHE at one Re as the representative case for all Re tested since the results were similar. The average standard deviation for all pixels is 125 W/m^2-K which include the largest standard deviation usually located at the five touching points of the cells. The total area of a touching point was of the order of 25 pixels which resulted in the relative large discrepancy due to the non-perfect pixel alignment of each cell.

However, the majority of the cell showed a low standard deviation which lets us conclude that all cells had similar HTC distribution due to flow uniformity.

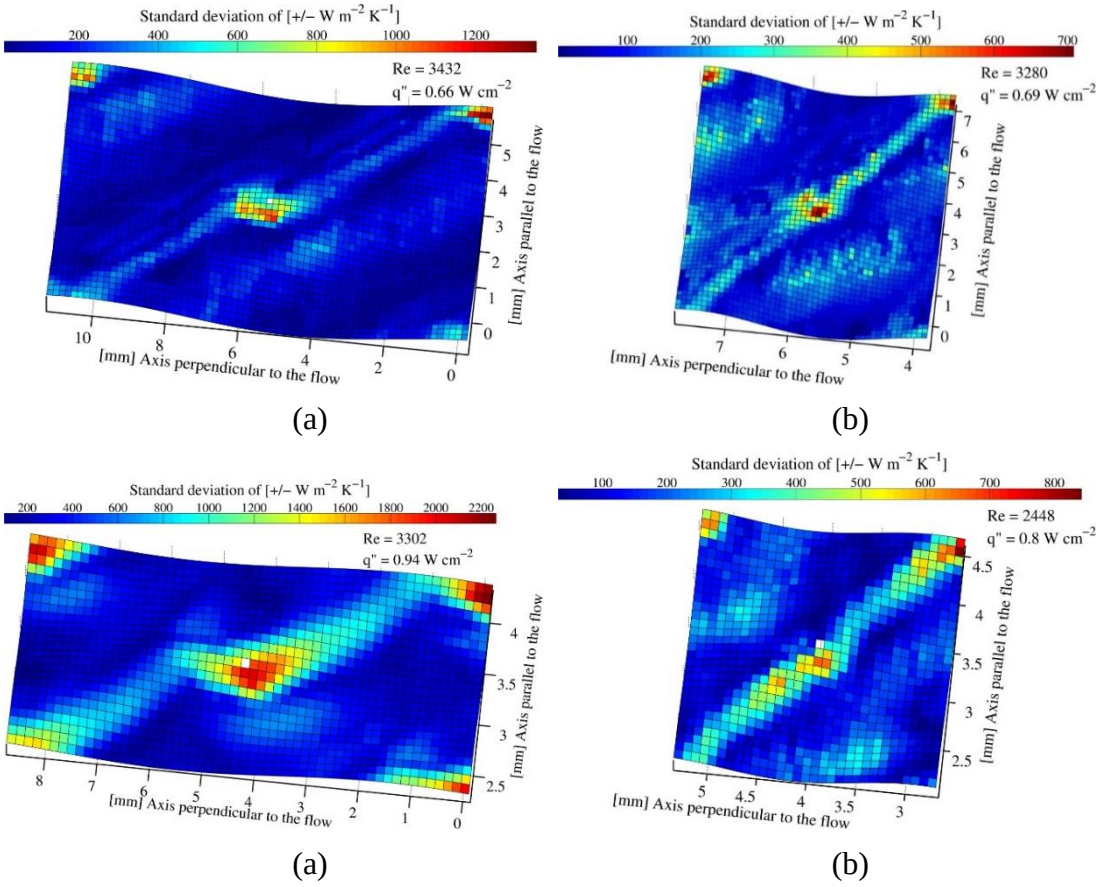

Figure 5.15: Weighted standard deviation of the heat transfer coefficient distribution within a representative cell for the (a) L5.7A1.0B60-60, (b) L5.7A1.0B60-30, (c) L3.7A0.5B65-65 (d) L3.7A0.5B65-25 PHE.

5.4 PHE performance comparison

The friction factor and Nusselt number for L5.7A1.0B60-60 are approximately twice as high as those for L3.7A0.5B65-65. The larger friction factor of L5.7A1.0B60-60, which has twice the pressing depth of L3.7A0.5B65-65, can likely be explained by the flow visualizations described by Focke and Knibbe [22]. They found that flow separation could occur for Reynolds numbers as low as 20 and the flow became

turbulent above *Re*~160 depending on the chevron angle. Smaller pressing depths might result in smaller separation regions and lower pressure losses. The corrugation aspect ratio γ is a good indicator of the trends since the pressure drop increases with γ. The effect of the small change in chevron angle β of 5° (from 60° to 65°) has less influence on the hydraulic performance.

With the exception of Muley and Manglik [10], the correlations listed in Table 5.1 depended on Reynolds numbers and the chevron angle, and did not include any dependence on the corrugation aspect ratio or surface enlargement factor. For L3.7A0.5B65-65 and L5.7A1.0B60-60, these correlations resulted in nearly identical curves since dependence on corrugation angle was negligible. Muley and Manglik [10] included the dependence on the surface enlargement factor φ. Their correlation suggested that L5.7A1.0B60-60 (with φ=1.25) would have a higher friction factor than L3.7A0.5B65-65 (with φ=1.17) , which is qualitatively consistent with the observed trends.

Figure 5.16 shows the HTC coefficient vs. frictional pressure gradient within all PHE. It can be seen that all geometries have similar performances. The L5.7A1.0B60-30 offers the best results, however during PHE optimization more factors have to be taken into account than just heat transfer and pressure drop performance. As previously seen, hard plates have a higher pressure drop but can produce higher HTC, this can be useful when minimizing the liquid charge of a PHE system or minimizing the size or number of plates needed to achieve certain cooling rates.

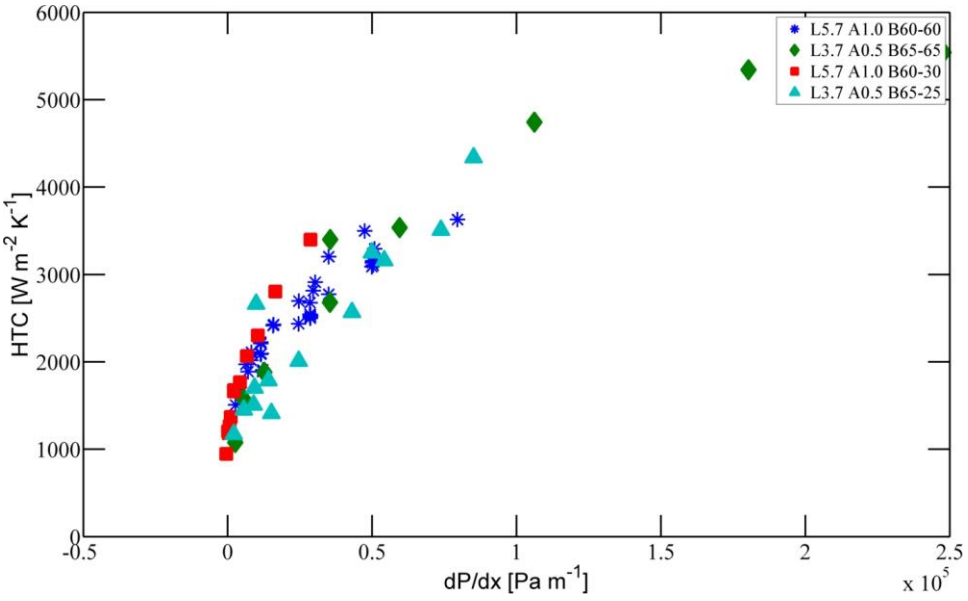

Figure 5.16: Comparison of experimental friction factor during single phase flow, for all tested geometries.

6. Two-Phase flow results

6.1 Flow Visualization

Using a high speed visual camera it is possible to capture different flow patterns in the PHE channel during adiabatic two-phase flow. Different inlet qualities were produced in the preheater. The channel was produced by pressing two polycarbonate plates together. The CaF_2 plates were not used for this experiment, since no heating was involved and the black heating film would have made the illumination rather cumbersome. The channel was back lit by an array of LEDs illuminating the bubbles by shining light through both plates. As a plastic, polycarbonate (Lexan) has a relative low thermal conductivity ($k_{Lexan} = 0.2 W m^{-1} K^{-1}$), and with a thickness of more than 6 mm it can be treated as an insulator. This means that the quality in the flow will not drastically change due to condensation. However, the quality will increase in the channel because of the decreasing pressure downstream. Since the pressure is measured along the channel, it is possible to calculate the local quality in the section that the camera is recording as described in Chapter 4.4.4. The quality change along the test section due to the two-phase pressure drop was found to be negligible.

We were able to observe two distinct flow patterns for both geometries, namely bubbly flow and film flow. For both cases, bubbly flow was visible up to a quality of $x = 0.05$. Then with an increase in quality the flow turned into a film flow and remained unchanged for higher qualities. The results of the flow visualizations for both geometries are shown in Figure 6.1 and Figure 6.2.

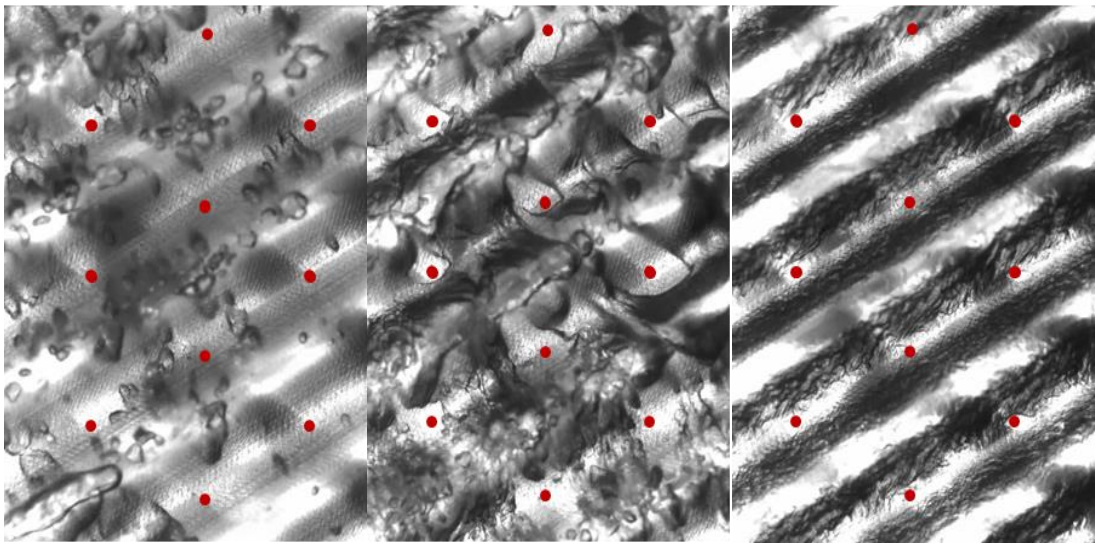

(a) (b) (c)

Figure 6.1: Two-phase flow visualization for L5.7A1.0B60-60 at G = 100 kg m^{-2} s^{-1}: (a) bubbly flow x = 0.02, (b) churn flow x = 0.05, (c) film flow x = 0.30. The red circles indicate contact points between the plates.

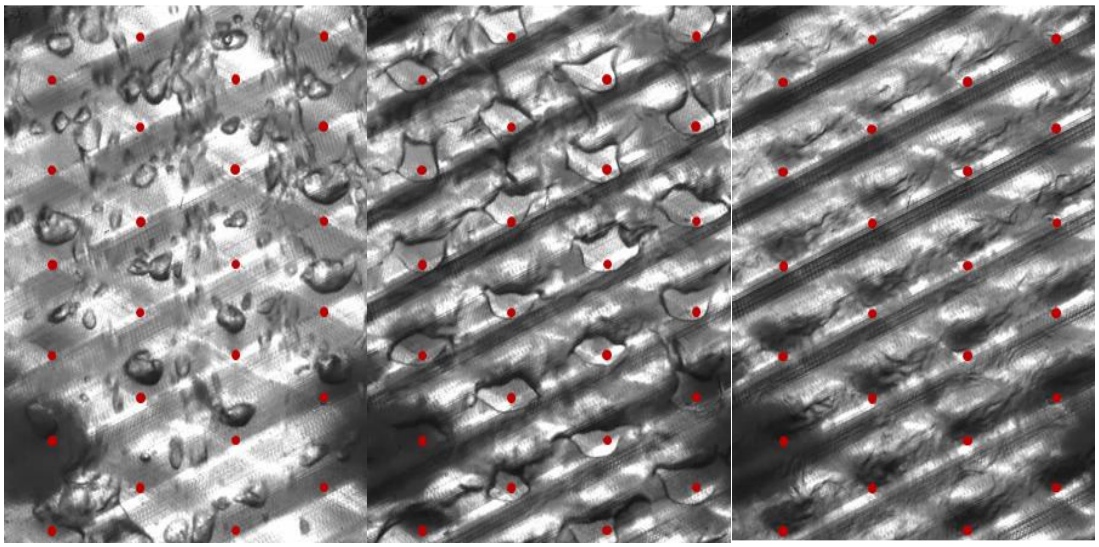

(a) (b) (c)

Figure 6.2: Two-phase flow visualization for L3.7A0.5B65-65 at G = 100 kg m^{-2} s^{-1}: (a) bubbly flow x = 0.05, (b) churn flow x = 0.15, (c) film flow x = 0.4. The red circles indicate contact points between the plates.

Three patterns similar to those observed by Tribbe and Müller-Steinhagen [24] were seen. At low qualities (x < 0.05) the flow was in the bubbly flow regime independent of the mass flux. Individual bubbles could become trapped for a short time where the spacing between both plates was maximum as shown in Figure 6.1a and Figure 6.2a. Low HTC was measured in these areas. With increasing quality, individual bubbles merged to form a liquid layer that covered the entire plate except at the contact points where dry spots periodically formed. For qualities greater than x=0.2, the liquid formed a stable film on the surface until dryout occurred at very high qualities. The size of the vapor region around the contact points decreased as the quality increased.

6.2 Pressure Drop

The two-phase frictional pressure gradient versus quality for all geometries is shown in Figure 6.3 and Figure 6.4.

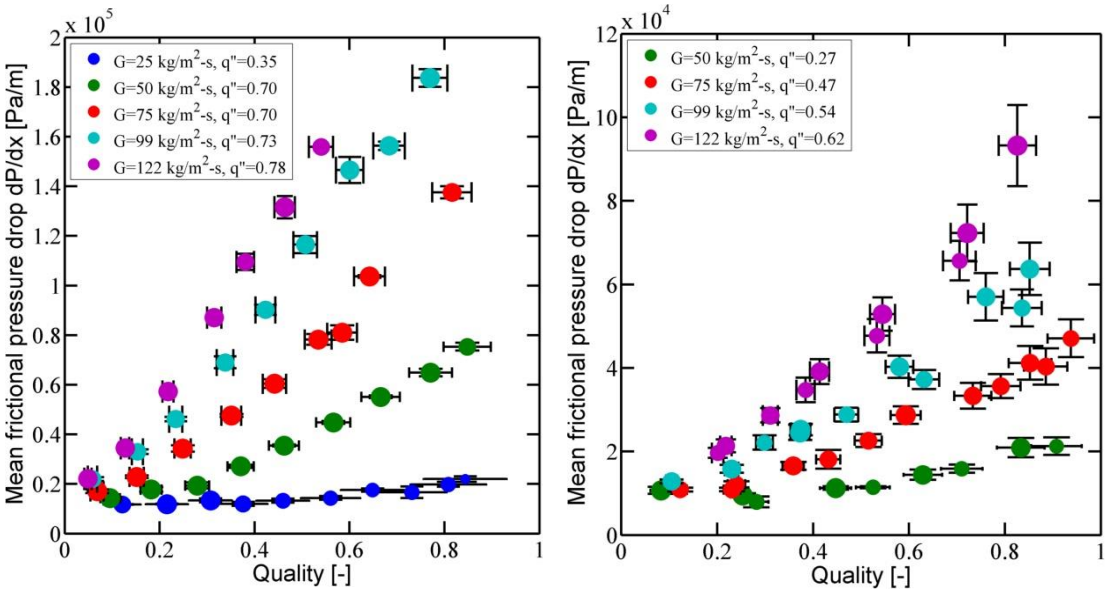

(a) (b)

Figure 6.3: Two-phase pressure drop results: (a) mean frictional pressure gradient versus mean quality for L5.7A1.0B60-60 geometry and (b) L5.7A1.0B60-30 geometry

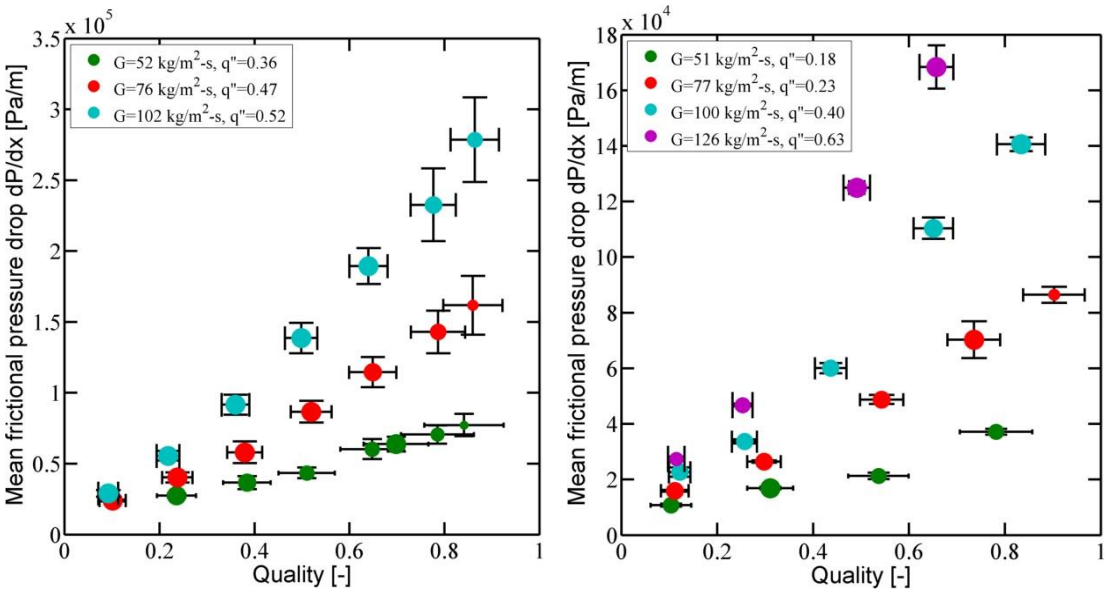

(a) (b)

Figure 6.4: Two-phase pressure drop results: (a) mean frictional pressure gradient versus mean quality for L5.7A1.0B60-60 geometry, (b) L5.7A1.0B60-30 geometry, and (c) L3.7A0.5B65-65 geometry.

The frictional pressure gradient increased with quality and mass flux as expected due to the shear stress at the liquid-vapor interface which is the dominant factor in the overall pressure drop. No sudden jumps due to changes in flow pattern were observed. At low qualities the pressure drop is less dependent on the mass flux than for high qualities, since the two-phase pressure drop depends on the vapor phase rather than the liquid phase, as was observed by numerous research groups [31, 35, 40, 54]. The soft plates reduce the frictional pressure drop by up to 50% of their hard plate counter parts.

The two-phase pressure gradient data were compared against many of the available correlations. The experimental versus predicted frictional pressure gradient for the best four correlations are shown in Figure 6.5 and the correlations along with the experimental test conditions are listed in Table 6.1.

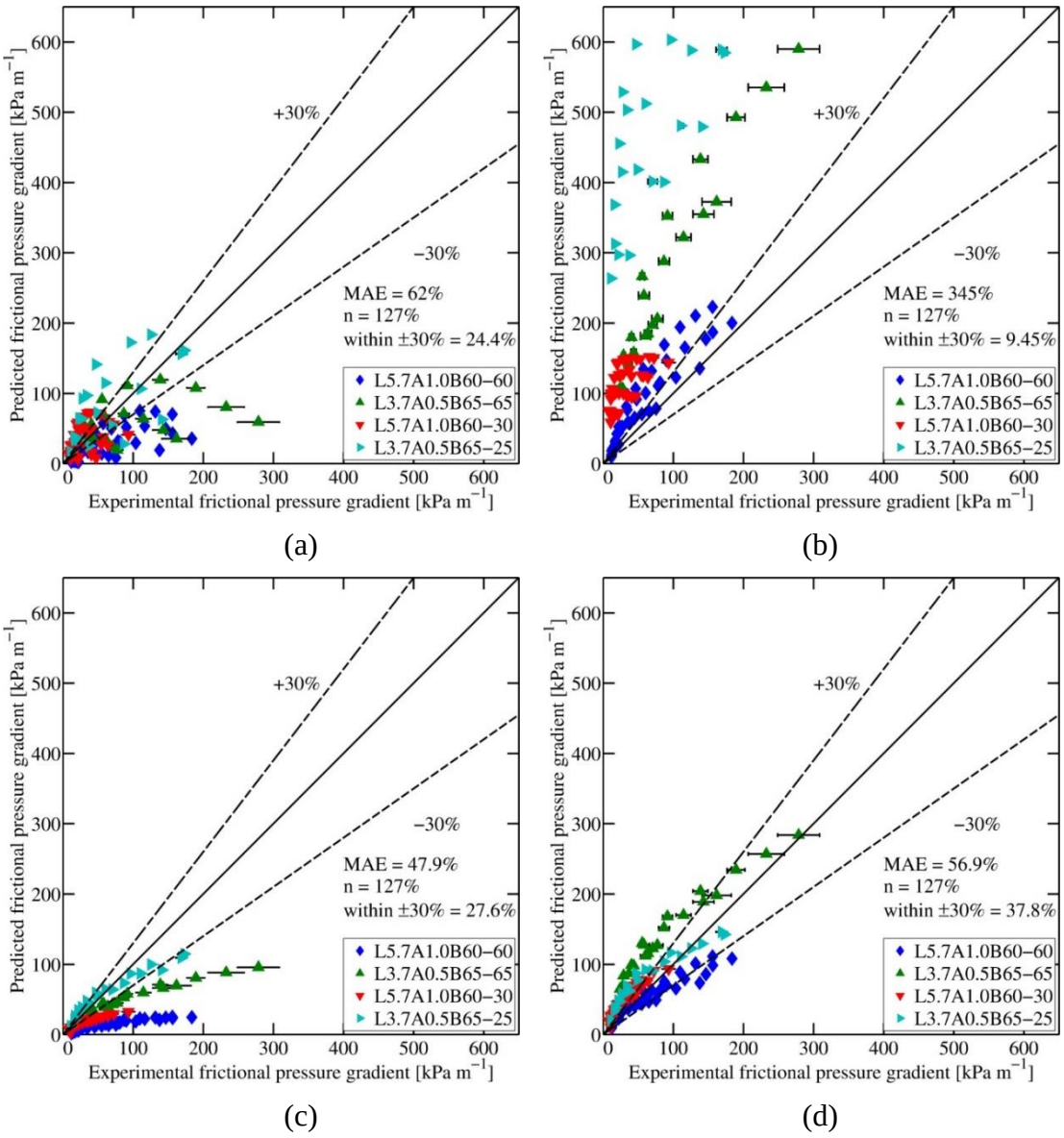

Figure 6.5: Two-phase frictional pressure drop data compared to the most quoted prediction methods from the literature: (a) Nilpueng and Wongwises [28], (b) Khan et al. [46]–[48], (c) Lee et al. [54], (d) Amalfi et al. [50,51].

Authors	Equations	Experimental Test Conditions
Nilpueng and Wongwises [28]	$\phi_l^2 = \frac{(dp/dz)_{tp}}{(dp/dz)_l} = \left(1.339 + \frac{C}{\mathrm{X}}\right) \quad C = 4.492$ $f_l = 4.929\,\mathrm{Re}_l^{-0.22}$	G = 129-264 kgm^{-2}s^{-1}, T_{sat} = 20 °C x = 0-0.04, q = 0 kWm^{-2} L- A1.25B55-10 Air-water mixture
Khan et al. [46]–[48],	$f_{tp} = 673336\,\mathrm{Re}_{eq}^{-1.3}\,p_r^{0.9} \quad \beta = 30°$ $f_{tp} = 305590\,\mathrm{Re}_{eq}^{-1.26}\,p_r^{0.9} \quad \beta = 45°$ $f_{tp} = 212\,\mathrm{Re}_{eq}^{-0.51}\,p_r^{0.53} \quad \beta = 60°$	G = 5.5-27 kgm^{-2}s^{-1}, T_{sat} = -25 °C to -2 °C x = 0.10-0.90, q = 6-49 kWm^{-2} L6.3A1.1B30-30, L6.3A1.1B30-60 L6.3A1.1B60-60 Ammonia
Lee et al. [54]	$f_{tp} = 49.13\,\mathrm{Re}_{eq}^{-0.4386}\,\mathrm{Re}_{lo}^{-0.4074}$	G = 14.5-34 kgm^{-2}s^{-1} , T_{sat} = 105 °C x = 0.10-0.90, q = 15-30 kWm^{-2} L10A1.25B60-60 Water
Amalfi et al. [50],[51]	$f_{tp} = (2.125\beta^{*9.993} + 0.955)\cdot$ $15.698 We^{-0.475} Bd^{0.255} \rho^{*-0.571}$	General prediction method on 1513 data points collected from 13 research studies between 1981 and 2015.

Table 6.1: Summary of the prediction methods for two-phase pressure drops including experimental test conditions

The reader is referred to Amalfi et al. [50],[51] for information regarding the operating test conditions and plate geometries for which these models were developed. The Mean Absolute Error is defined as:

$$MAE = \frac{100}{n}\sum_{j=1}^{n}\frac{\Upsilon_{j,pre} - \Upsilon_{j,\exp}}{\Upsilon_{j,\exp}} \qquad 6.1$$

The correlation from Nilpueng and Wongwises [28] (Figure 6.5a) was an underestimate of our data and this correlation was unable to follow the correct trend of the two-phase pressure drop data, especially in the higher qualities region. Conversely, Khan et al. [49] (Figure 6.5b) overestimated the present data because of the different test conditions (and ammonia as working fluid) and an incorrect evaluation of the inlet and outlet pressure drops. Lee et al. [54] (Figure 6.5c) strongly underestimated the

experimental data, since the authors investigated the dryout mechanisms at low mass fluxes using water which has a different behavior compared to the tested refrigerant. This model was able to capture the experimental data only at low refrigerant mass flux. The Amalfi et al. [50],[51] correlation (Figure 6.5d) provided the best agreement because it was developed over a wide range of operating conditions, fluids and plate geometries. This model slightly overestimated the experimental data due to the inlet and outlet pressure drops as well as extrapolation of the method to higher values of the refrigerant mass flux.

6.3 Area averaged HTC

The area-averaged HTC was calculated by averaging the local HTC over the area shown in Figure 6.6a to avoid entry length, inlet/outlet and side effects. The saturation temperatures measured by the five thermocouples are shown in Figure 6.6b. The temperature drop in the stream wise direction was consistent according to the measured total pressure drop as well as the variation of the thermodynamic properties along the PHE length. The cross-stream averaged wall temperatures are also plotted in Figure 6.6b beside with an example of the local temperature distribution along the black vertical line. The averaged wall-to-temperature difference was fairly constant and inlet/outlet effects were limited to ~10 mm near the test section inlet and exit. The wall-to-fluid temperature difference (and thus the HTC) did not vary significantly in the streamwise direction for most conditions tested, allowing the HTC averaged over the area within the white box to be correlated against the average quality.

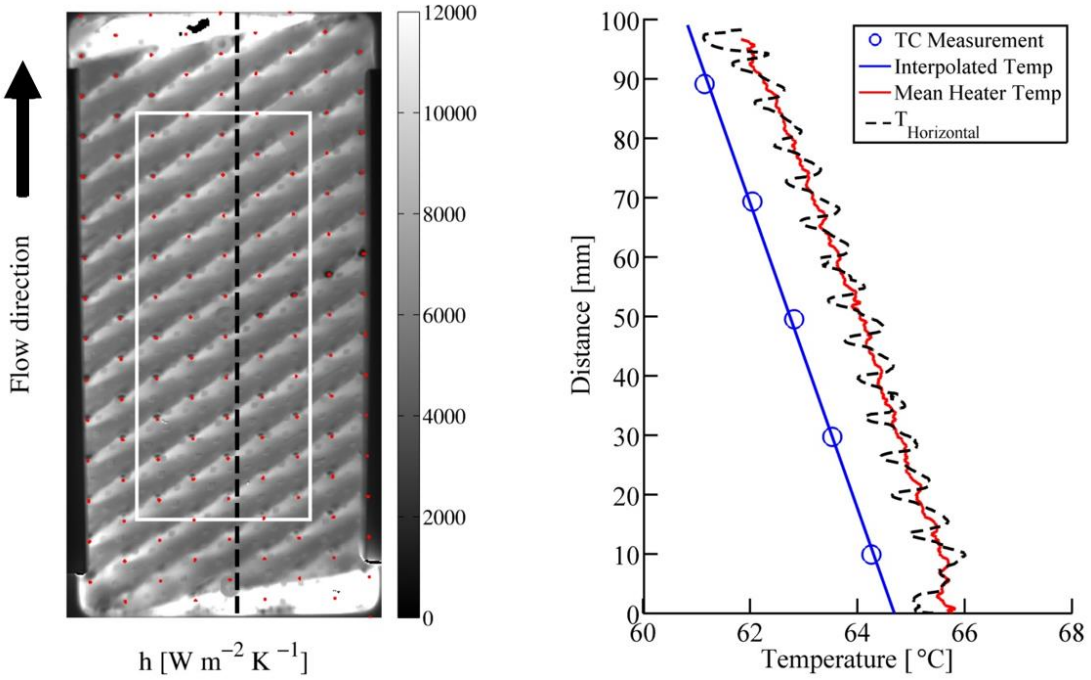

(a) (b)

Figure 6.6: Two-phase heat transfer results at G = 100 kg m^{-2} s^{-1} and x_i = 0.5: (a) time averaged HTC distribution for L5.7A1B60-60 with red dots indicating the contact points and the white box representing the area that was used for the overall HTC computation, (b) saturation temperature and mean heater temperature averaged over the partial width of the plate against the time averaged temperature along the dotted black line.

The uncertainty in HTC increased with quality as the wall-to-fluid temperature difference decreased. This could be partially mitigated by increasing the heat flux, but the maximum imposed heat flux was limited by the temperatures at the contact points that could become high enough to damage the tape used as an electrical insulator between the two film heaters. At higher inlet quality, the applicable heat flux lead to the partial dryout of the liquid film as shown in Figure 6.7. The left image illustrates the temperature from the IR-camera which highlights the presence of dryout in the upper half of the test section. The dryout area grew larger in size along the zig-zag

pattern as indicated by the arrows in Figure 6.7a. The heat transfer distribution computed from the temperature data for the same operating conditions is shown in Figure 6.7b. The technique to calculate HTC assumed that all the heat generated by the heaters is transferred into the fluid. However, when dryout occurs, the majority of heat generated is conducted into the substrate, and the heat flux into the fluid became essentially zero while the wall-to-fluid temperature difference increased (Figure 6.7c).

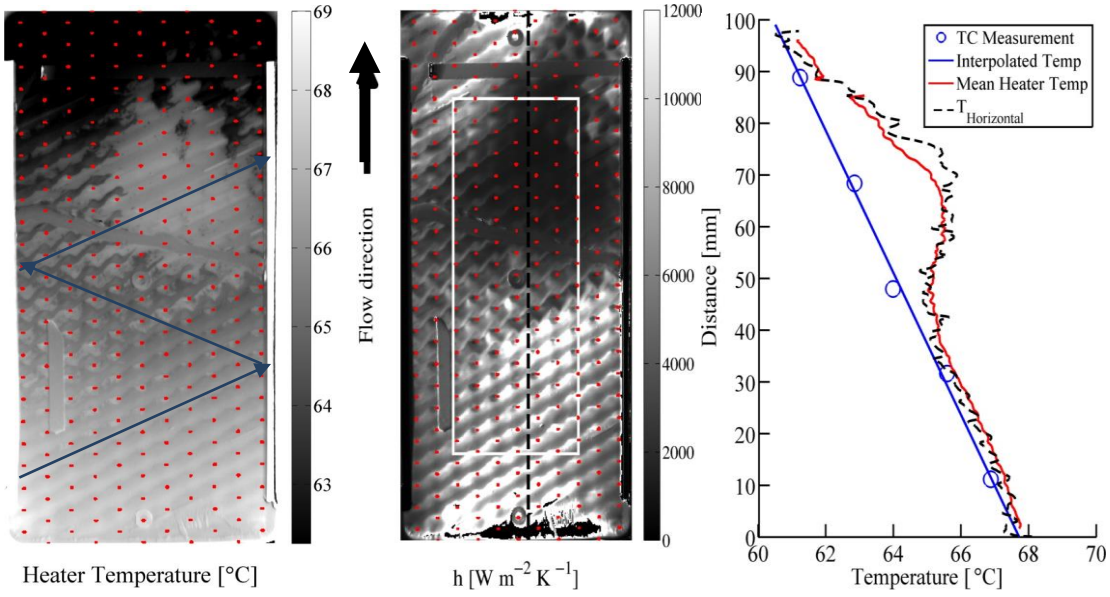

(a) (b) (c)

Figure 6.7: Partial dryout for L3.7A0.5B65-65 at G = 100 kg m-^{2} s-^{1} and x_i = 0.8: (a) instantaneous temperature distribution, with dots indicating the contact points and arrows show the direction of increasing dryout area, (b) time average HTC, with the white box indicating the area that was used for the overall HTC, (c) saturation temperature and mean heater temperature averaged over the partial width of the plate versus the time averaged temperature along the dotted black line.

Since a constant heat flux was assumed, the calculated HTC was higher compared to the actual heat transfer. In order to compute the true local HTC when dryout occurs, the transient heat conduction into the substrate as well as the temperature gradient at

the wall-fluid interface needs to be calculated as described in Kim et al. [60]. This procedure is beyond the scope of this work, however. The HTC data recorded during the dryout regime has been marked in the figures below and should be considered to be unreliable.

Figure 6.8 shows the two-phase HTC for all geometries plotted against the mean quality. The heat flux for each mass flux is the average value for all data points at this specific mass flux. The size of the data point in the graph indicates the heat flux value relative to the average value. The smaller the dot the smaller the heat flux. As cited before the heat flux had to be adjusted for some cases to minimize the measurement uncertainty and to prevent dryout. As mentioned by other research group ([33] [34] [38]) it is not expected that the HTC is dependent on the heat flux, since the mass flux is high enough that the dominant heat transfer mechanism is convective boiling, which is independent of heat flux. As expected, HTC increased with quality and mass flux for all geometries for the data where dryout does not occur. At low qualities the mass flux had a small effect on HTC, while at higher qualities, the effect of the mass flux became more significant. Similar results were observed by Djordjevic and Kabelac [39] and Margat et al. [33] who investigated flow boiling of refrigerants at high mass fluxes as in this study.

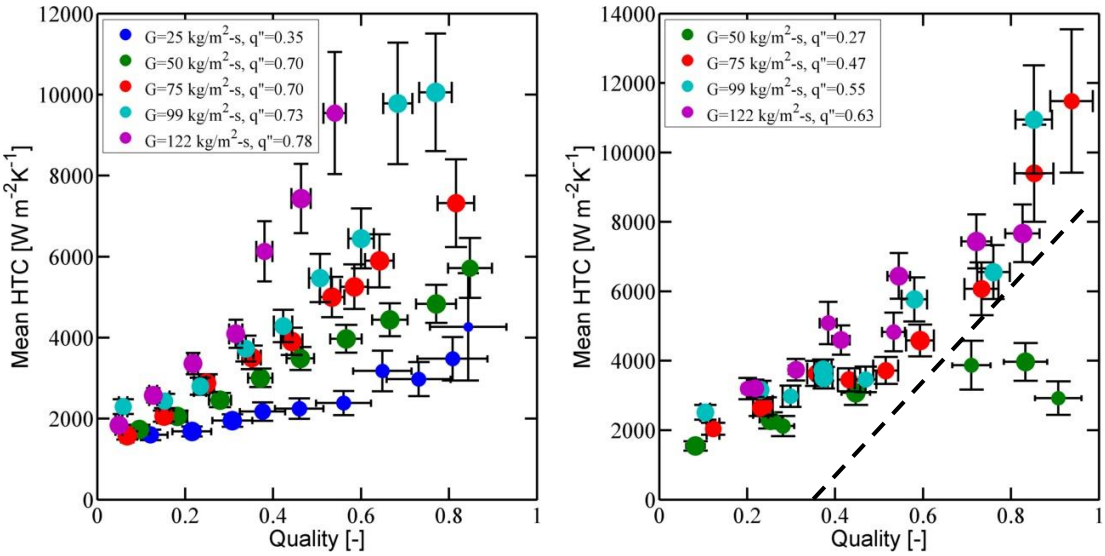

(a) (b)

Figure 6.8: Average two-phase heat transfer results: (a) HTC versus quality for L5.7A1.0B60-60 and (b) HTC versus quality for L5.7A1.0B60-30. Dryout occurred for the data to the right of the dotted line and are therefore unreliable.

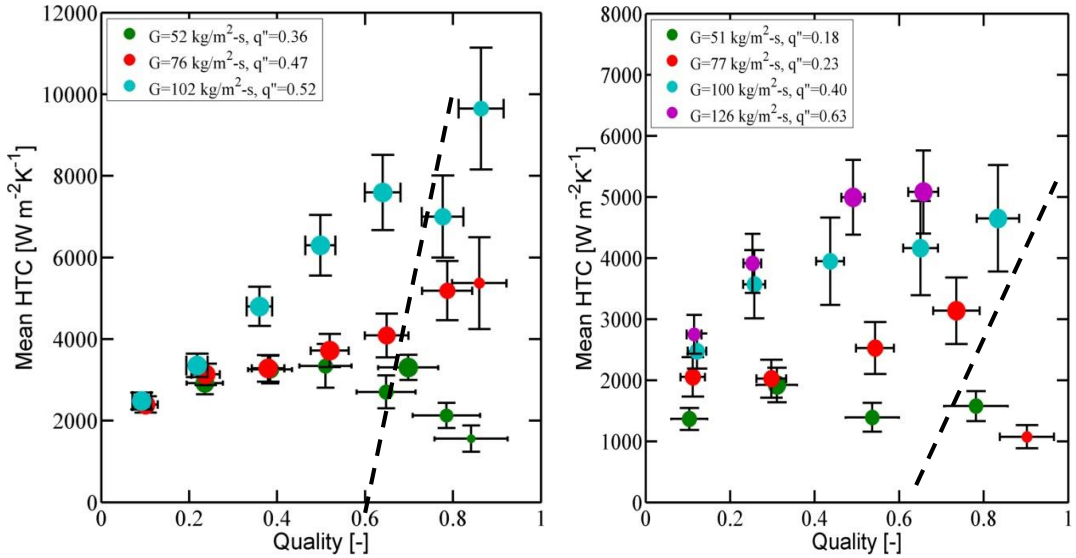

(a) (b)

Figure 6.9: Average two-phase heat transfer results: (a) HTC versus quality for L3.7A0.5B65-65 and (b) HTC versus quality for L3.7A0.5B65-25. Dryout occurred for the data to the right of the dotted line and are therefore unreliable.

The current two-phase heat transfer data were compared to models available in the literature. The results are presented in Figure 6.10 and the correlations along with the experimental test conditions are listed in Table 6.2 . The models of Donowski and Kandlikar [61] (Figure 6.10a) and Hsieh and Lin [62] (Figure 6.10c) agreed well with the data. Han et al. [34] (Figure 6.10b) was able to predict the experimental data at low mass flux conditions since the authors included in their model the effect of the hydraulic diameter, wavelength of the surface corrugation, and chevron angle. The agreement is much worse at higher mass fluxes. The Amalfi et al. [50],[51] method (Figure 6.10d), even though developed with a consolidated experimental databank, was able to capture the heat transfer data at low mass fluxes, but overall underestimated the present data. The poor agreement could be due to the present approach of evaluation of the inlet and outlet pressure drops, which play an important role in the local HTC calculation.

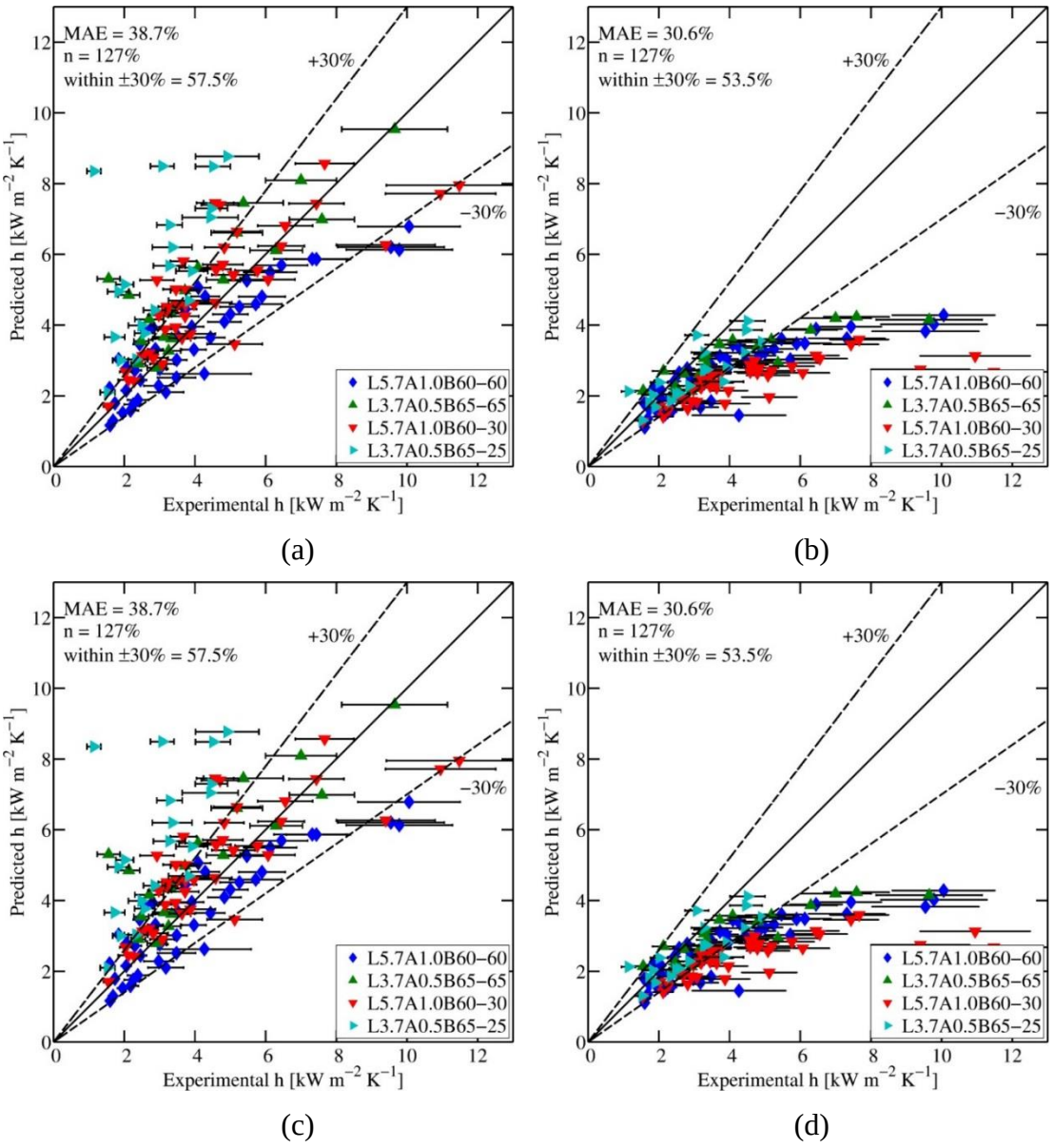

Figure 6.10: Two-phase heat transfer data compared to the most quoted prediction methods from the literature: (a) Donowski and Kandlikar [61], (b) Han et al. [34], (c) Hsieh and Lin [62], (d) Amalfi et al. [50,51].

Authors	Equations	Experimental Test Conditions
Donowski Kandlikar [60]	$S = \frac{Nu_{tp}}{Nu_{lo}} = \left[1.184Co^{-0.3} + 225.5Bo^{2.8}\right](1-x)^{0.003}$ $Nu_{lo} = 0.2875\,\mathrm{Re}_{lo}^{0.78}\,\mathrm{Pr}_l^{1/3}$	G = 55-70 kgm^{-2}s^{-1}, T_{sat} = 25.5-31 °C x = 0-0.90, q = 11-15 kWm^{-2} L10 A1.65 B60-60 R134a
Han et al. [34]	$Nu_{tp} = Ge_1\,\mathrm{Re}_{eq}^{Ge2}\,Bo_{eq}^{0.3}\,\mathrm{Pr}_l^{0.4}$ $Ge_1 = 2.81\left(\Lambda/d_h\right)^{-0.041}\left(\pi\beta/180\right)^{-2.83}$ $Ge_2 = 0.746\left(\Lambda/d_h\right)^{-0.082}\left(\pi\beta/180\right)^{0.61}$	G = 27 kgm^{-2}s^{-1}, T_{sat} = 5-15 °C x = 0.15-0.95, q = 5.5 kWm^{-2} L7A1.1B45-45, L5.2A1.1B55-55 L4.9A1.1B70-70 R410A
Hsieh and Lin [62]	$Nu_{tp} = Nu_{pool}S + Nu_{lo}F$ $Nu_{lo} = 0.023\,\mathrm{Re}_{lo}^{0.8}\,\mathrm{Pr}_l^{0.4}$ $Nu_{pool} = 55\left(d_h/k_l\right)P_r^{0.12}\left(-\log_{10}p_r\right)^{-0.55}M^{-0.5}q^{0.67}$ $F = 1 + 24000Bo^{1.16} + 1.37\left(1/\mathrm{X}_{tt}\right)^{0.86}$ $S = \left(1 + 1.15\times10^{-6}F^2\,\mathrm{Re}_{lo}^{1.17}\right)^{-1}$	G = 50-100 kgm^{-2}s^{-1}, T_{sat} = 10-15 °C x = 0-0.90, q = 10-20 kWm^{-2} L10A1.65B60-60 R410A
Amalfi et al. [50,51]	$Nu_{tp} = 982\beta^{*1.101}We^{0.315}Bo^{0.320}\rho^{*-0.224}$ $Bd < 4$ $Nu_{tp} = 18.495\beta^{*0.248}\,\mathrm{Re}_v^{0.135}\,\mathrm{Re}_{lo}^{0.351}\ldots$ $Bd^{0.235}Bo^{0.198}\rho^{*-0.223}$ $Bd > 4$	General prediction method on 1903 data points collected from 13 research studies between 1981 and 2015.

Table 6.2: Summary of the prediction methods for two-phase heat transfer including experimental test conditions

6.4 Local Heat transfer Measurements

Figure 6.11 to Figure 6.14 show the local two-phase HTC for all geometries with increasing quality. The HTC distribution in a unit cell during the two-phase regime is very similar to the single phase flow, since the heat transfer mechanism is mainly convective boiling. For single phase we observed changes in HTC up to a factor of 2 within a unit cell. For two-phase flow, however, this factor increased up to a value of ~2.5. In all geometries, the lowest HTC was found to be at the contact point, while the highest HTC was located on the upstream side of a furrow where the fluid accelerates. The biggest area of constant HTC remains in the downstream side and center of the

furrow and its value decreases with increasing quality relative to the maximum HTC. The touching point in the center is clearly visible for low qualities, at high qualities however it merges with the upstream side of the furrow.

At lower qualities, the highest HTCs occurred in those areas close to, but upstream of, the contact point where the flow cross-section narrows, resulting in an acceleration of the flow. The lowest HTCs occurred downstream of the contact point and was likely due to a thin layer of stagnant fluid that was prone to dryout. As the quality increased for the pure plate arrangement, the semi-continuous band of high HTC on the upstream side of the furrow "split" due to the formation and rewetting of a dry patch. For the mixed arrangement the high HTC region remained upstream of the contact point for high qualities.

For L3.7A0.5B65-65/L3.7A0.5B65-25, dry patches were observed more frequently and were larger in size than for L5.7A1.0B60-60/ L5.7A1.0B60-30. These oscillations were clearly visible in both the IR-videos and flow visualizations. This may be due to instabilities within the preheater. The flow cross sectional area of L3.7A0.5B65-65 was half that of L5.7A1.0B60-60, but the diameter of the tube used to heat the fluid to the desired inlet quality remained constant. The mass flux in the preheater for L3.7A0.5B65-65 was thus half that for L5.7A1.0B60-60 at a given PHE mass flux, resulting in a more unstable flow for L3.7A0.5B65-65, especially at higher inlet qualities.

Figure 6.11 shows the HTC distribution for the L5.7A1.0B60-60 at four qualities. When the average quality is low the HTC distribution is identical with the one from single phase (Figure 6.11a). At a quality of ~0.2 the HTC maximum that used

to be located upstream of the contact point is starting to shift to the right side of the contact point. In addition the downstream side of the furrow is decreasing in HTC relative to the maximum value of the cell (Figure 6.11b). When increasing the quality further, the maximum HTC has completely shifted to the left and right side of the contact point, leaving a corridor of lower HTC upstream the flow direction.

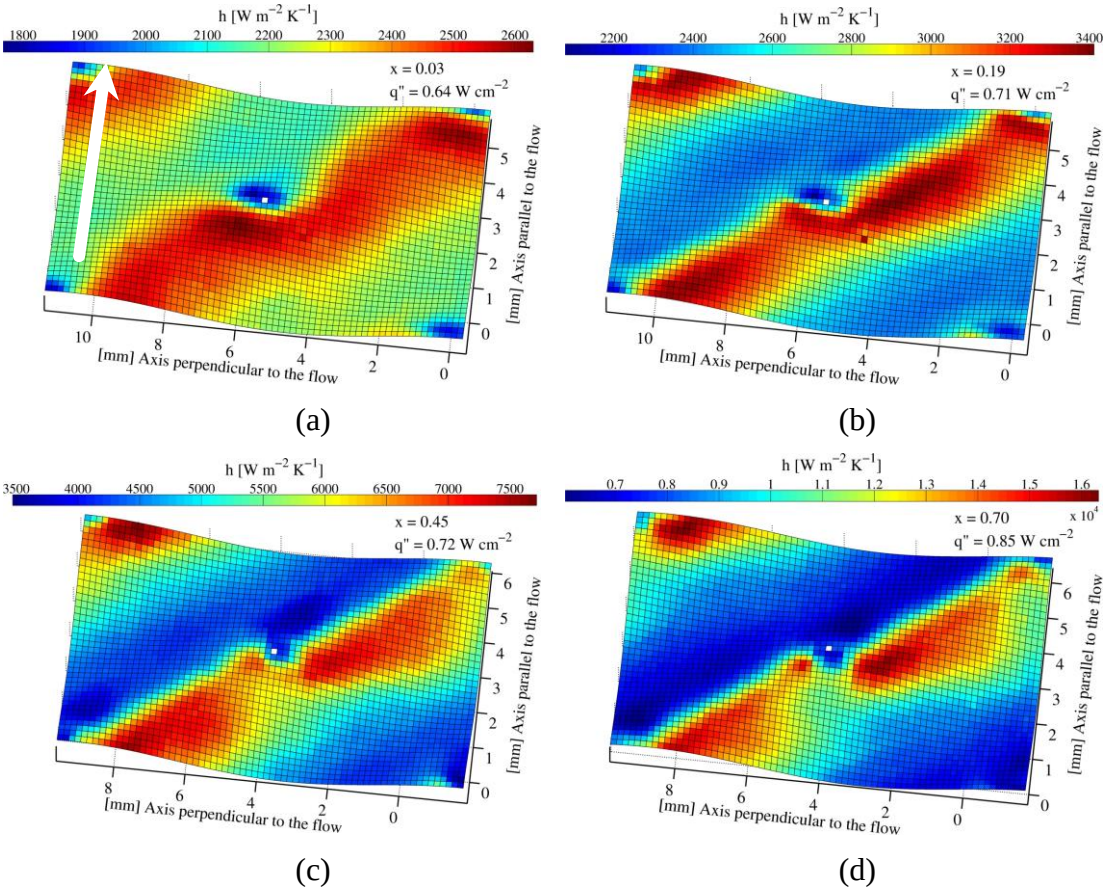

Figure 6.11: Local time averaged HTC distribution in a single cell for L5.7A1.0B60-60 at G = 100 kg m^{-2} s^{-1}, the white squares shows the location of the contact point and the white arrow in (a) the flow direction, quality and heat flux are listed in the upper right corner

The upstream side of the furrow has a very low HTC and some parts have a similar low HTC as the contact point (Figure 6.11c & d). The flow visualization showed that at

these conditions small patches of vapor would temporarily cover the area around the touching point and therefore decrease the HTC (Figure 6.1). The visualization also showed that at elevated qualities the downstream side of the furrow has a thicker and turbulent layer of liquid whereas the upstream side seems to be covered with a thin and homogeneous layer. At high heat fluxes this layer dries out, leading to small HTC similar to the one at the contact point (Figure 6.1c-d). Further, it was observed that at elevated qualities the contact point initiates a dry patch which stretches to the next contact point located downstream along the flow. The surrounding liquid confines that dry spot to a narrow corridor, which is why the HTC upstream of the contact point decreases at high qualities.

Figure 6.12 shows the HTC distribution for the L5.7A1.0B60-30 at four qualities. As previously mentioned, due to the mixed plate arrangement the bulk flow velocity is shifted by 15° as is indicated by the white arrow in Figure 6.12a. Contrary to its hard counter plate, the HTC distribution does not change with increasing quality. The maximum remains upstream of the contact point for all qualities, yet the decrease in HTC on the upstream furrow at high quality could be observed. This indicates that the upstream side of the furrow is not covered with a thick enough liquid layer which promotes dryout. The dryout corridor which was observed for L5.7A1.0B60-60 cannot be created for the mixed plate arrangement due to the shifted bulk flow velocity vector, which is why the maximum HTC remains upstream of the contact points for all qualities.

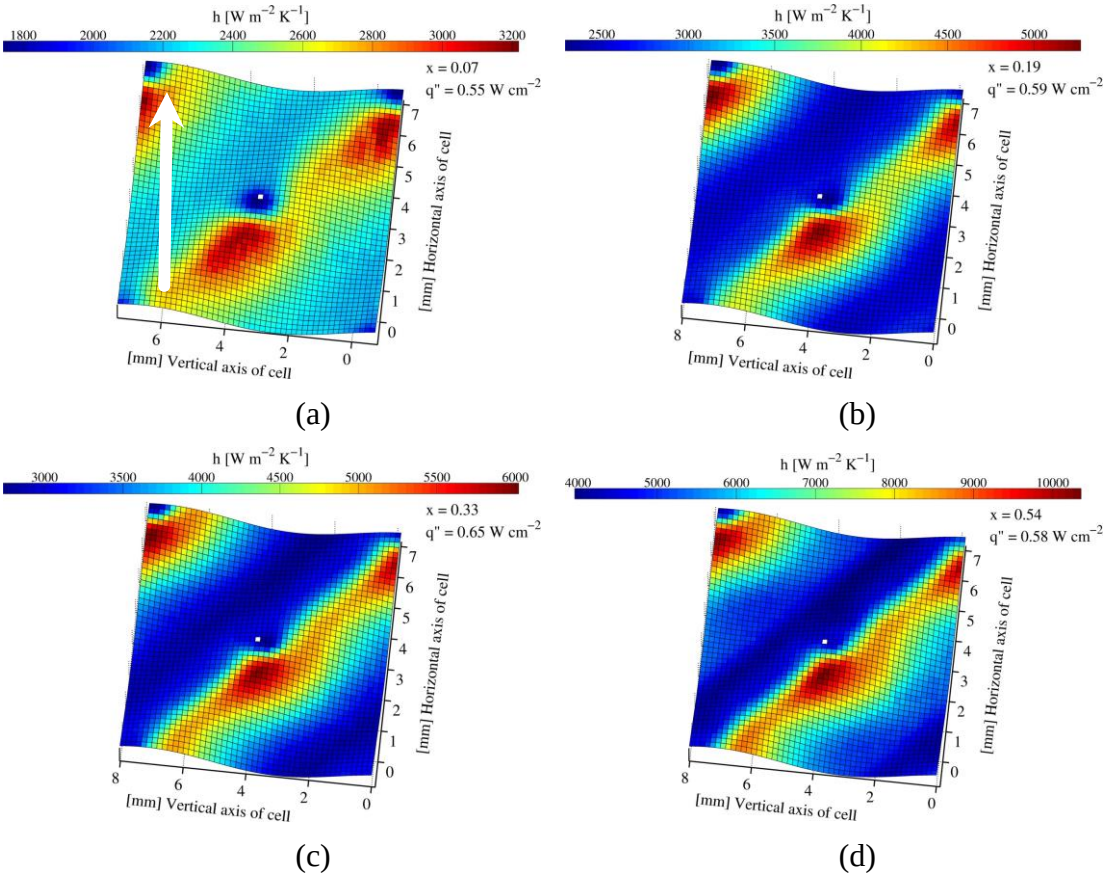

Figure 6.12: Local time averaged HTC distribution in a single cell for L5.7A1.0B60-30 at G = 100 kg m^{-2} s^{-1}, the white squares shows the location of the contact point and the white arrow in (a) the flow direction, quality and heat flux are listed in the upper right corner.

Figure 6.13 shows the HTC distribution for the L3.7A0.5B65-65 at four qualities. At low qualities a similar HTC pattern is observed as for the L5.7A1.0B60-60, with the difference that the maximum is located to the right of the contact point and the elevated HTC area extends further downstream due to the lower pressing depth. At high qualities the high HTC region upstream of the contact points disappears due to the growing dryout area which is initiated at the contact point and continuous in a narrow strip downstream to the next contact point. In the flow visualization this phenomenon is clearly visible as well as a thinning layer on the upstream side of the furrow.

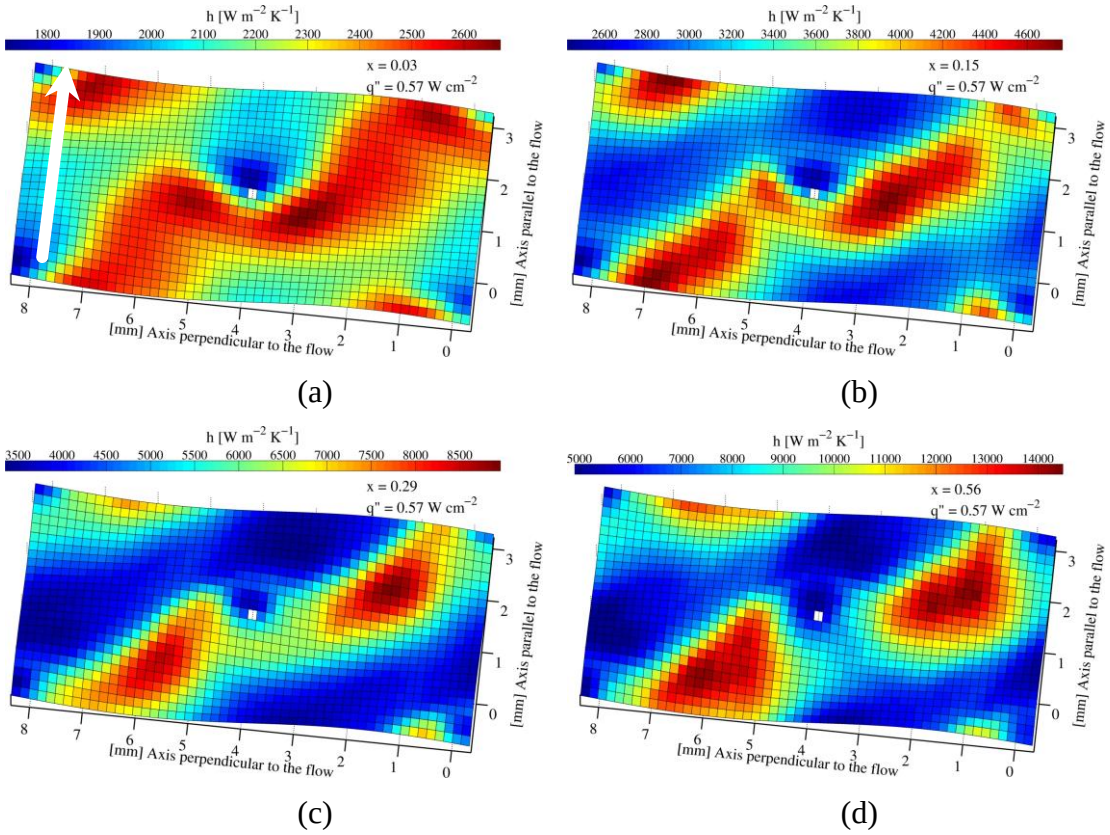

Figure 6.13: Local time averaged HTC distribution in a single cell for L3.7A0.5B65-65 at G = 100 kg m^{-2} s^{-1}, the white squares shows the location of the contact point and the white arrow in (a) the flow direction, quality and heat flux are listed in the upper right corner.

Figure 6.14 shows the HTC distribution for the L3.7A0.5B65-25 at four qualities. At low qualities the HTC distribution looks similar to the L3.7A0.5B65-65 at high qualities, where two distinctive maxima, left and right to the contact point can be observed (Figure 6.14a). At elevated qualities, however the HTC distribution is different to all previously discussed geometries. The low HTC area is only limited to the downstream side of the contact point and does not occupy the furrow over its complete length (Figure 6.14d). The L3.7A0.5B65-25 PHE is rotated relative to the

flow direction by 20° this could break up the dry area that is created at each contact point as was seen by the pure plate configurations. The relative large shift angle forces the liquid that is split by the contact point to directly hit another contact point downstream, therefore increasing the HTC substantially upstream of the contact point (Figure 6.14d). For the pure plate arrangement the contact point would create a wake that would last to the next contact point and thus having a continuous path where little to no liquid is covering the surface.

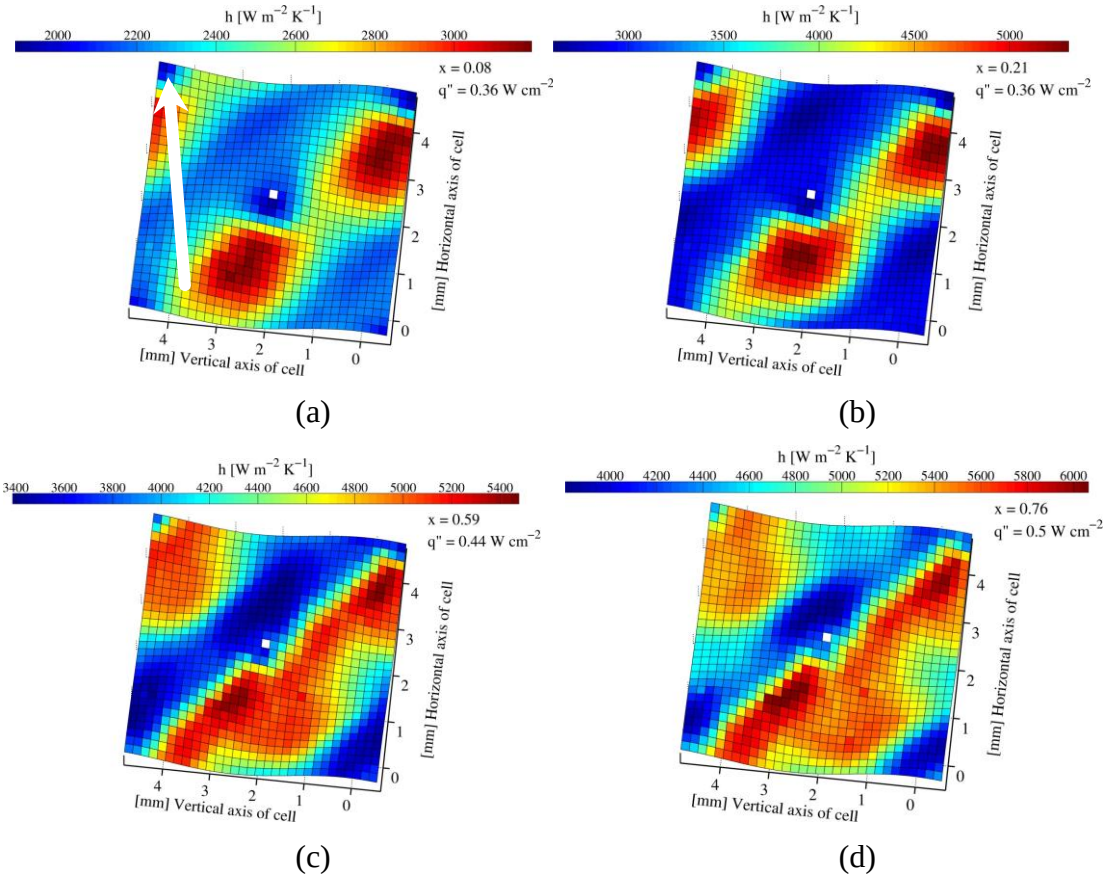

Figure 6.14: Local time averaged HTC distribution in a single cell for L3.7A0.5B65-25 at G = 100 kg m^{-2} s^{-1}, the white squares shows the location of the contact point and the white arrow in (a) the flow direction, quality and heat flux are listed in the upper right corner.

6.5 Dryout observation

As previously mentioned, partial dryout was observed for the L3.7A0.5B65-65 and L3.7A0.5B65-25 geometry. Instantaneous temperature measurements of the heated film were used to analyze the location and propagation of the dryout areas in a PHE cell. The local temperature distribution was a good indicator to identify which areas were wet and which were not since the temperature at a dry spot increased rapidly. The temperature distribution in the L3.7A0.5B65-65 cell shown in Figure 6.15Figure 6.15 illustrates how dryout progresses. At low qualities (Figure 6.15a), the temperature distribution indicates HTC is similar to that shown in Figure 6.13 since no dryout has yet occurred (high temperatures correspond to low HTC and vice versa). When the inlet quality is increased (Figure 6.15b), the point of lowest temperature (highest HTC) just upstream of the contact point experiences an increase in temperature indicating local dryout. With further increases in flow quality (Figure 6.15c and Figure 6.15d), the dry patch gradually enlarges until the side of the furrow upstream of the contact point is covered by vapor and liquid is only left on the downstream side of the furrow.

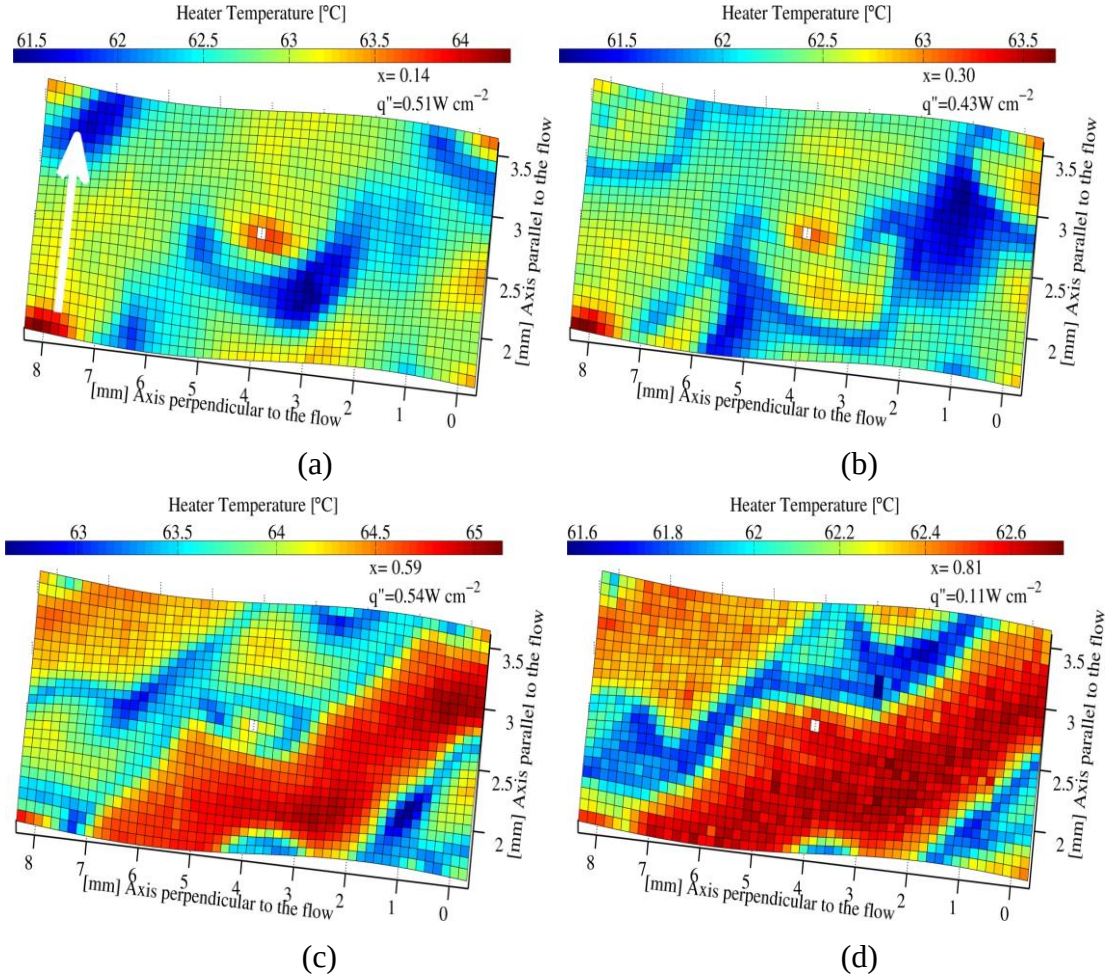

Figure 6.15: Local temperature distribution in a single cell for L3.7A0.5B65-65 at G = 50 kg m-^{2} s-^{1}, the white squares shows the location of the contact point and the white arrow in (a) the flow direction, quality and heat flux are listed in the upper right corner.

6.6 PHE performance comparison during two-phase flow

The trend of the mean HTC against the associated frictional pressure gradient for both plate geometries is shown in Figure 6.16.

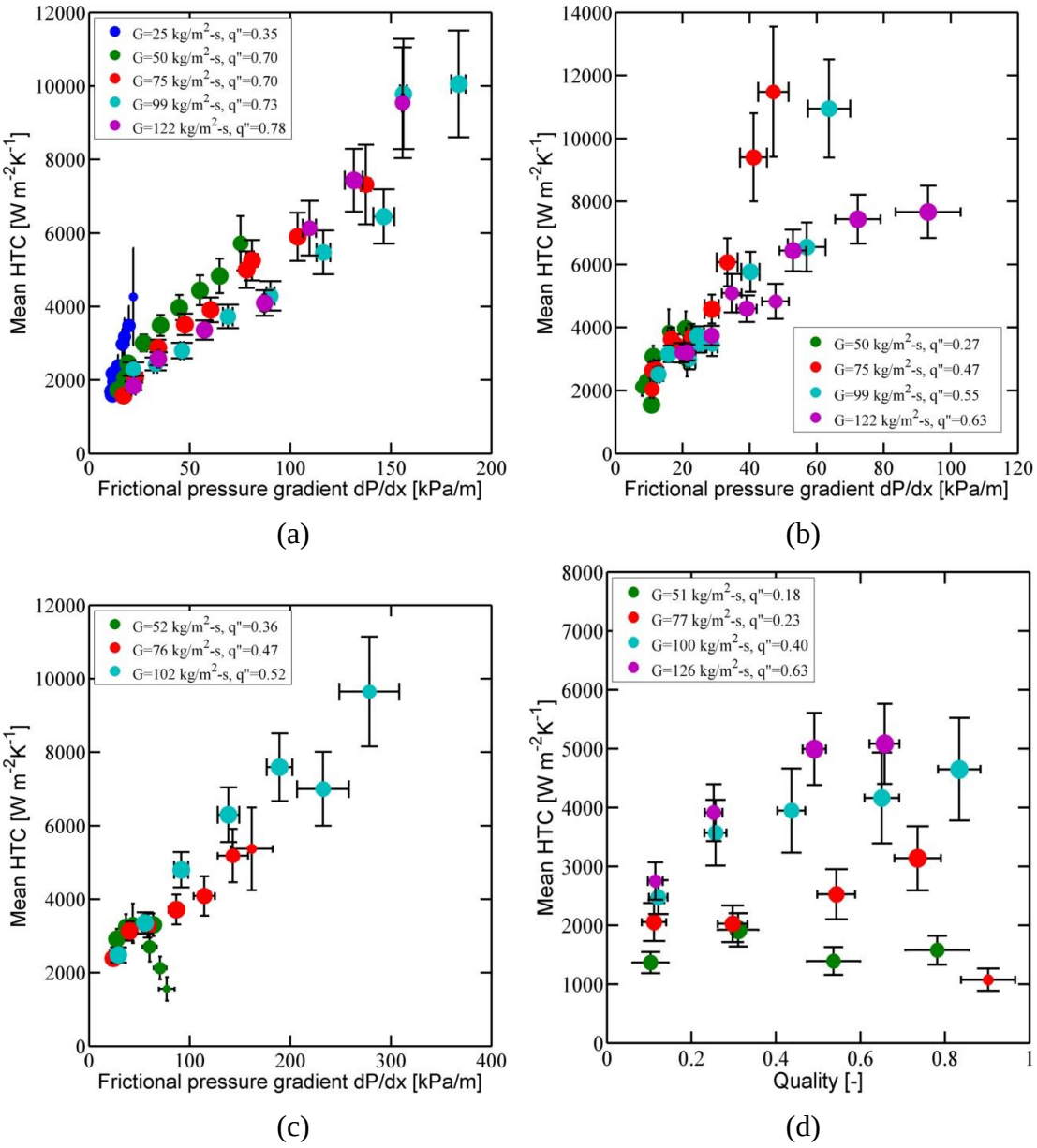

Figure 6.16: Average two-phase heat transfer results vs frictional pressure drop data: (a) L5.7A1.0B60-60, (b) L5.7A1.0B60-30, (c) L3.7A0.5B65-65, and (d) L3.7A0.5B65-25.

For the cases with no dryout, the trend in the data could be well described by a linear relationship. The 5.7A1.0B60-60 geometry provides slightly higher heat transfer than L3.7A0.5B65-65 geometry for a given pressure gradient, as was seen for the single phase heat transfer results. This might be associated with the larger pressing depth of

the L5.7A1.0B60-60 geometry that introduces higher turbulence, while the larger cross-section area of the flow channel decreases the pressure drop. The soft plates provide higher or equal HTC for a given pressure gradient, as was seen for the single-phase heat transfer results. This may be associated with the rotation of the PHE relative to the bulk flow velocity. With the rotation of the PHE the contact points are not parallel to the flow velocity, therefore breaking up growing dry patches that are initiated at each contact point. The L5.7A1B60-30 outperforms its hart counter plate especially in the high quality region, whereas the L3.7A0.5B65-25 has a similar performance as its hard counter plate. For the purpose of overview the performances of all plates are plotted in Figure 6.17.

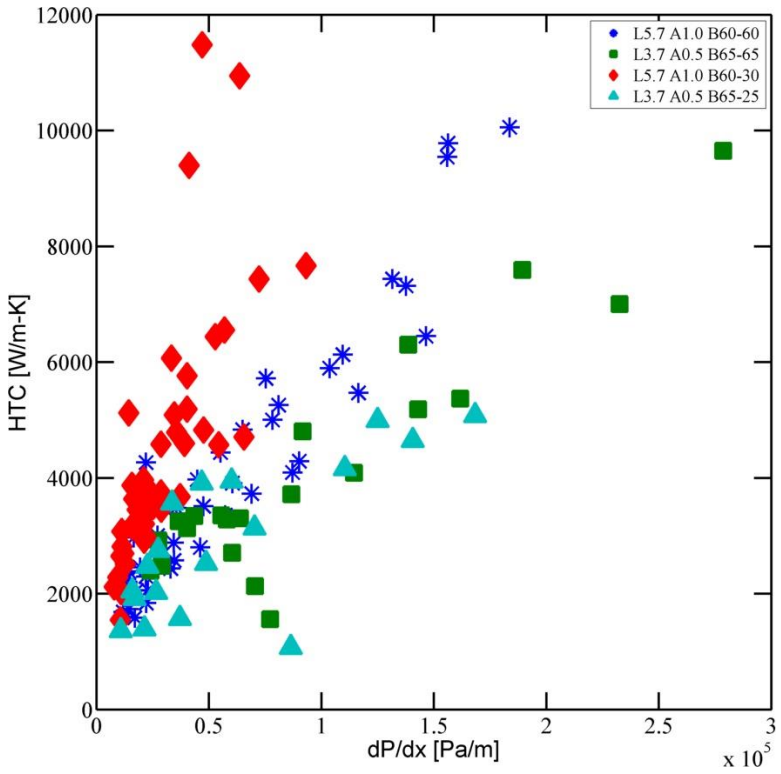

Figure 6.17: Average two-phase heat transfer results vs frictional pressure drop gradient for all data points

7. Conclusion and future outlook

Measurements of local flow boiling heat transfer and pressure drop within four PHE geometries were obtained using IR thermography. The PHE channels were created by pressing corrugated plates together, one made from IR-transparent CaF_2 and the other from a compliant plastic (polycarbonate). Both plates were heated by electric film heaters epoxied onto the corrugated surfaces. Five equally spaced thermocouples and five pressure taps were used to measure the temperature and pressure distribution. 3D-printed inlet and outlet flow distributors were used to create a flow that became thermally and hydrodynamically fully developed after a short entrance length. The technique was validated by comparing the measured friction factor and the Nusselt number with commonly used correlations for single phase flow.

Further analysis of the heat transfer within a unit cell showed a distinct pattern that was repeated throughout the entire PHE. For single phase flow, the ratio between the minimum and maximum heat transfer coefficient within the unit cell was measured to be ~2 and for two-phase flow ~2.5 over the range of Reynolds numbers tested, indicating that the heat transfer over all surfaces was quite uniform due to the widespread mixing. For the single phase flow, this was much smaller than the ratio observed by other researchers. Further research into the causes of this discrepancy is required.

The pressure gradient and HTC for all geometries increased steadily with mass flux and inlet quality at low to intermediate qualities. At high inlet qualities the measurement uncertainty in HTC became unacceptably large since the wall-to-fluid temperature difference was small even at the highest heat input which was restricted

by local burnout at the contact points for L5.7A1.0B60-60/L5.7A1.0B60-30 and partial dryout for L3.7A0.5B65-65/ L3.7A0.5B65-25. The HTC varied linearly with the pressure gradient for both geometries for the cases where dryout did not occur. When comparing the two-phase data to existing correlations very little agreement was observed, which is likely due to the fact that most researchers based their findings on global PHE data which include the inlet/outlet port and flow distributer pressure drops. The end ports of a PHE have a significant effect on the overall performance, potentially obscuring the local data if not taken into account. Using different liquids and small variations in geometries could also have a substantial effect on each data set.

In general, we observed that all tested PHE had similar performance when comparing the HTC to the pressure drop over the entire plate. The L5.7A1.0B60-30 performed slightly better than the rest of the plates. However, to achieve high HTC with low flowrates, a plate with lower amplitude and larger corrugation angles is preferable. For two-phase flow we could see a better distinction especially at higher qualities. As in single phase flow, the L5.7A1.0B60-30 outperformed the other plates, although similarly high HTC were achieved by plates with smaller amplitude and higher corrugation angle at lower mass fluxes and higher pressure drops. For the plates with low amplitude we could observe a decrease in HTC for low mass fluxes and high qualities ($x > 0.5$).

The time averaged, spatially resolved HTC distribution measurements within a representative PHE cell during two-phase flow indicated a minimum at the contact point, an elevated HTC on the upstream side of a furrow, and a maximum located just upstream of the contact point. As the inlet quality increased, the heat transfer

distribution became increasingly non-uniform. At high qualities the maximum HTC located upstream of the contact points began to disappear for the L5.7A1.0B60-60 and L3.7A0.5B65-65 geometry indicating local dryout. The two mixed PHE L5.7A1.0B60-30 and L3.7A0.5B65-25 showed different HTC patterns than their hard plate counterpart, since mixing two plates with different corrugation angles shifted the flow velocity vector relative to the PHE. Adiabatic two-phase flow visualizations indicated film flow to be the dominant flow regime with the vapor core sandwiched between thin liquid layers. Dryout periodically appeared in the proximity of the contact points, and these dry areas became more stable and smaller as the quality increased.

This work did not focus on establishing correlations for singe and two-phase flow since all measured values were obtained within the PHE. Real PHE have additionally a flow distribution system and inlet and outlet port which both can play a significant role on the heat transfer and pressure drop for the PHE system. More research in that field is necessary to predict the performance of a PHE.

The main contribution of this thesis is the development of a new technique that allows the measurement of local HTC on corrugated surfaces. This technique can help researchers to identify heat transfer and pressure performance of a corrugated pattern without taking into account inlet/outlet flow distribution systems and ports. We showed that the former can have significant effects on the overall performance of the PHE, especially for plates with small corrugation angles. PHE designers now have a tool to determine the performance of the PHE section exclusively. When performing additional experiments with a real PHE possessing the same properties, designers can easily identify the heat transfer and pressure losses over the fluid distribution systems

and ports by subtracting the extrapolated data that was gained using the technique described in this thesis.

For future experiments, the geometry of the CaF_2 plates can be altered to analyze the effect on changes in $,\beta, \lambda, d_{eq}$, and mixed vs pure plate arrangements on heat transfer and pressure drop. The apparatus and the technique described can be extended to the measurement of transient heat transfer, which will enable the analysis of transient two-phase flow within PHE geometries. A technique similar to that developed by Kim et al. (2012) can be used to calculate the instantaneous temperature profiles within the test wall, enabling transient heat transfer coefficients to be computed at the wall-liquid interface.

8. Appendices

8.1 Thermal conductivity measurement of 200RS100 film

The film heater used in this study (Dupont 200RS100) consisted of two layers, an insulating layer made of pure polyimide and a carbon-filled, electrically conductive polyimide layer with high emissivity. The thermal conductivity for the polyimide film was available from literature values (k=0.15 W/m^2-K), but the value for the carbon filled layer was unknown.

The principle for measuring the thermal conductivity of the carbon filled layer was to electrically heat square sections of the film and measure the temperature distribution with an IR camera and compare with numerical simulations. Figure 8.1 shows a schematic of the apparatus. Three pieces of film were cut and suspended between two copper electrodes to produce three square heated areas (2 mm, 4 mm, and 6 mm). The top and bottom edges of the film were kept at a constant temperature by the copper electrodes. The apparatus was mounted in a vacuum chamber to ensure that the heat generated within the film was lost only by conduction through the film to the electrodes and by radiation to the surroundings. The vacuum chamber had a silicon window with an anti-reflection coating (Edmund Optics #47-943) so the temperature distribution within each film could be measured using an IR camera.

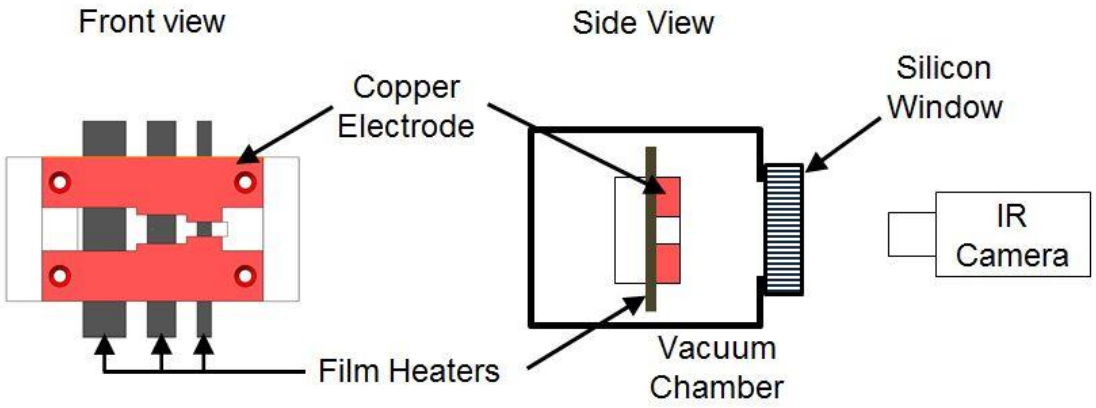

Figure 8.1: Schematics of the test configuration for determining the thermal conductivity of the electrically conductive layer in the 200RS100 film.

For a square heater of a given size, the shape of the temperature profile within the film is dependent on the thermal properties of the film, the heat generated within the film, the energy radiated from the surface of the film to the surroundings, and the thermal contact resistance between the film and the copper electrodes. The total heat generated in all three heaters was the same since the voltages and resistances were identical. Numerical simulations were performed to find the temperature distribution and the thermal conductivity and thermal contact resistance values to match the measured data were found. Comparison of the temperature distributions measured using the IR camera with the temperature distribution from the simulations is shown on. The ratio of the generated heat lost through radiation to that lost by conduction along the film into the copper electrodes increases with heater size, resulting in flatter temperature profiles. The thermal contact resistances and thermal conductivities required to obtain good agreement between the measured and calculated temperature distributions are shown for the three heater sizes. The thermal conductivity of the film is seen to be greater than 6 W/m-K.

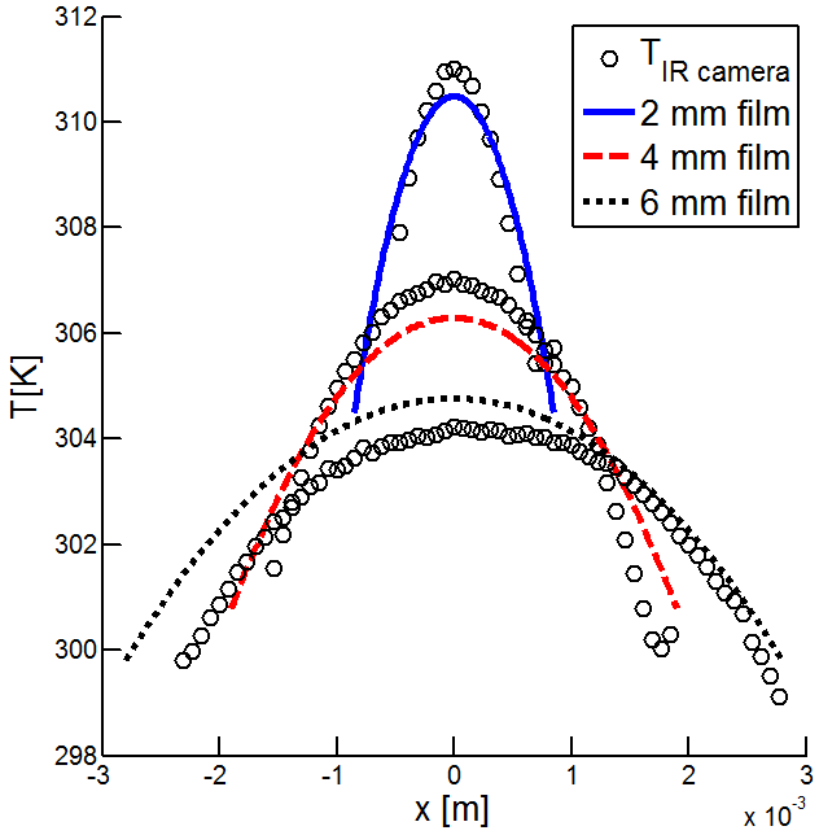

Figure 8.2: Comparison of the numerical and measured film temperature distributions at a voltage of 1 V using a thermal contact resistance of 10^{-3} m^2 K W^{-1} and a thermal conductivity of 7 W $m^{-1}K^{-1}$.

8.2 Outlook for transient HTC analysis

To measure the instantaneous HTC during two-phase evaporation in the PHE it is necessary to calculate the instantaneous temperature profile within the multilayer depicted in Figure 4.7. Therefore it is necessary to solve a conduction equation with two temperatures as boundary condition. Since the highest temperature drop is over the adhesive and a polyimide film (due to their low thermal conductivity) it is feasible to have the first temperature measurement at the liquid-heater interface, and the second one at the CaF_2-adhesive interface. The heating film has a high emissivity which

simplifies the measurement of the first temperature. For the second temperature, thin and highly emissive black dots were attached to the CaF_2 substrate. This section discusses the design criteria, such as size and spacing of the black dots.

8.2.1 Black dot sizing

The size of the black dots is not only dependent on the distance between camera and object, but also heavily dependent on the properties of the camera, namely optical properties and focal plane array (FPA) resolution. In the case of the Flir Silver 660 the resolution is 640x512 pixels with a horizontal field of view of (HFOV) 20° and vertical field of view (VFOV) of 16°, resulting in an instantaneous field of view (IFOV) of approximately 0.56 mrad. With a perfect camera that is perfectly aligned, so that one detector element would cover the whole black area of the black dot, the minimum edge length *s* of the black dot could be calculated for a certain camera to object distance *d* using Equation 8.1.

$$s = IFOV * d \tag{8.1}$$

Knowing that it is impossible to perfectly align the camera with the black dot one would increase the size of the black dot by a factor of 4 (2x2 pattern), so no matter how bad aligned the camera is, at least one detector element would be covered by the black dot. Due to defects of optical lenses, nonlinearity of the electro-optical sensor, wrong focus or vignetting there will always be a degradation of the original image. Each pixel will affect its neighboring pixel by changing its true value. This can clearly be seen, when a razor blade is placed in front of the opening of a heated black body.

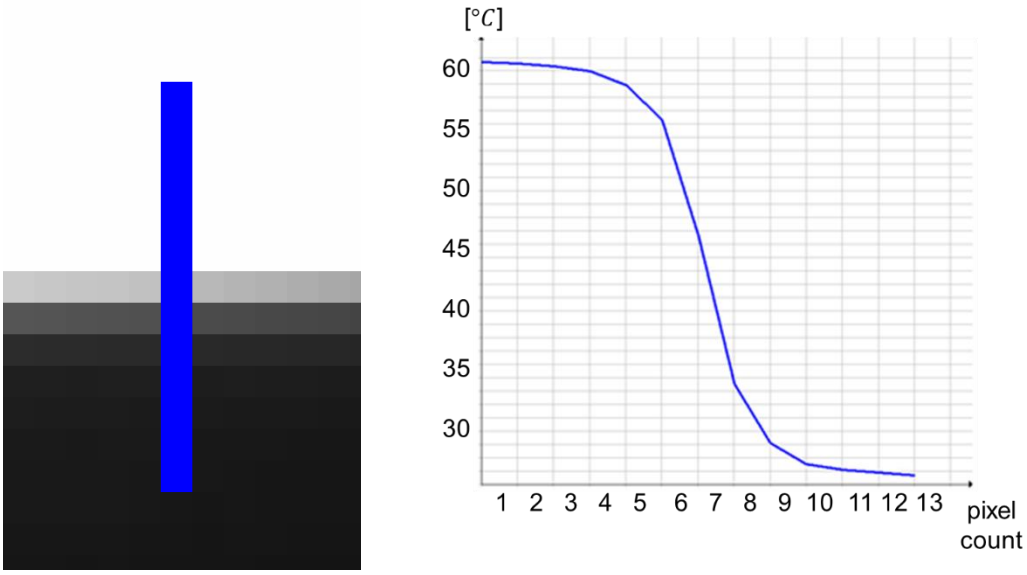

Figure 8.3: Infrared image of the razor blade edge placed in front of a heated black body (right) and the temperature profile across the edge (left)

Figure 8.3 shows that it takes approximately 6-7 pixels in order to go from the high to low temperature value. In the black dot case, we will not be dealing with one edge but rather two edges since the observed object is a dot. This means that theoretically the minimum edge length of the dot needs to be equal or larger than 12-14 pixels. With a minimum focus distance of roughly 110 mm, we would need a dot edge length of approximately 1 mm.

8.2.2 Black dot spacing

As mentioned in Section 4.2 the spacing of the black dots needed to be small enough to accurately predict the temperature between the dots using interpolation. A 2-D numerical heat conduction simulation was carried out in Matlab to determine the amount of heat spreading within the polyimide film and the optical glue. Each of the three layers was divided into 40 nodes. A step function in temperature was used as the

boundary condition on the top nodes of the polyimide film as depicted in Figure 8.4. The steady state temperature profile along the multilayer was numerically computed and the results are shown in Figure 8.5. The spacing between the dots, was chosen such that the temperature profile between the dots could be accurately reconstructed using spline interpolation as can be seen in Figure 8.6.

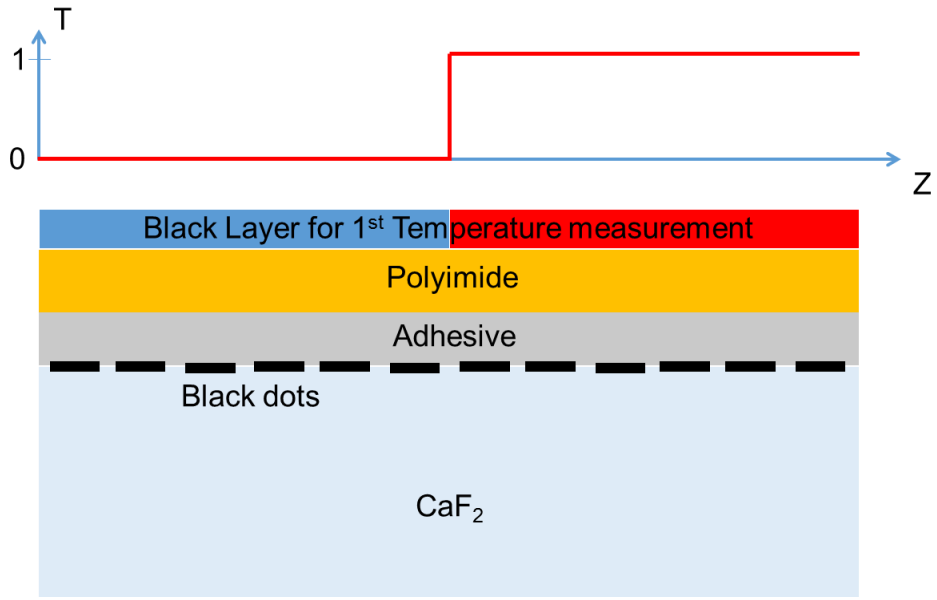

Figure 8.4: Schematic representation of the forced boundary condition in the form of a step function

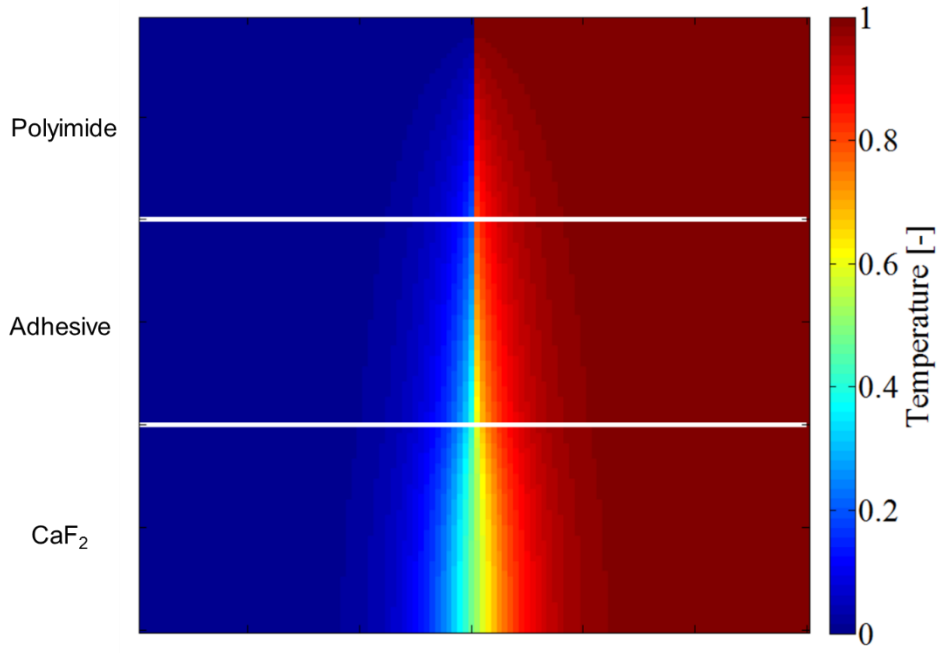

Figure 8.5: Steady state heat spreading within the multilayer

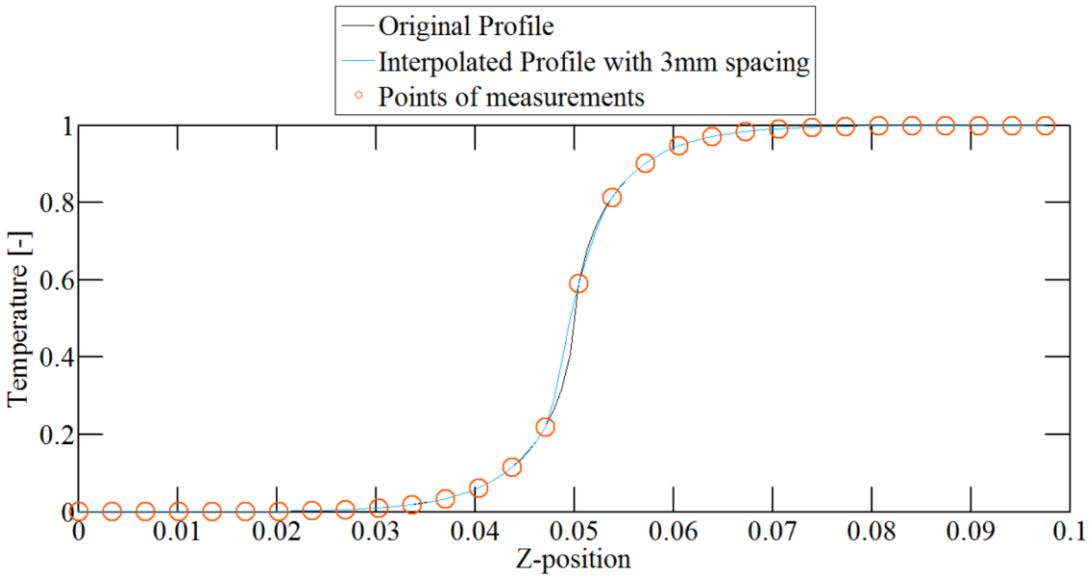

Figure 8.6: Calculated temperature profile along the CaF_2-adhesive interface and the interpolated temperature profile using the temperature measurements of the virtual dots that are 3 mm spaced apart.

8.3 Consideration of alternative heating methods

Numerous alternatives were considered to uniformly heat a PHE geometry, while measuring high resolved heat transfer. Two methods that were applied and failed are discussed in this section.

8.3.1 Silicon heater

Initially it was proposed to measure heat transfer and acquire flow visualization by using an IR thermometry technique developed by Kim et al. [60] that takes advantage of the transparency of silicon in the mid-IR range (3–5 μm). Two plates were cut out of single crystal silicon ingot and the L5.7 A1.0 B60-60 was CNC-machined into the material. The provided silicon was intrinsic meaning that it had no defects and therefore did not conduct electricity. Therefore the flat surface of each plate was n-doped using Boron. The amount of dopant determines the emissivity of the silicon (Figure 8.7) which is why a relative low amount of dopant was applied on the flat surface. Leads were mechanically attached on the sides of the silicon. To reduce the contact resistance. The sides were heavily doped and a layer of chromium and silver was additionally deposited similar to the process explained in Kommer [63].

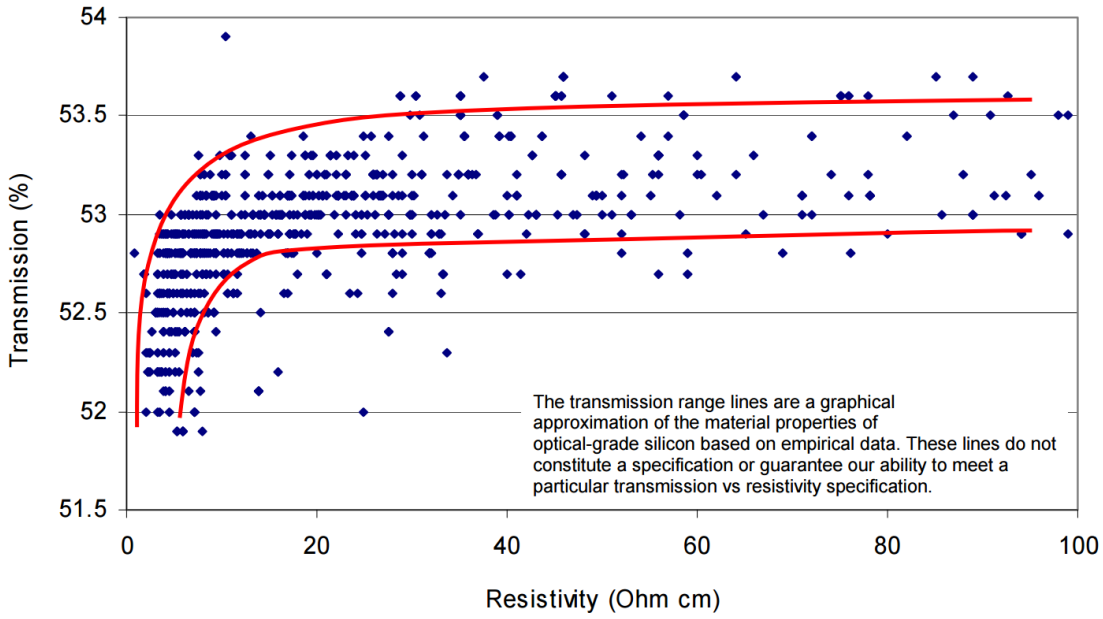

Figure 8.7: Transmission @ 3.0 um through an uncoated polished 0.5 mm thick sample, data provided by Lattice [64]

The plates were each coated on the inner wall with a 60 μm layer of polyimide tape as shown in Figure 8.8b. One plate was then covered with an IR opaque paint containing carbon black (Nazdar GV111), which allowed an effective inner wall temperature to be measured through the silicon and polyimide layer (Figure 8.8c). Two strips of the painted polyimide tape were also attached to the outer wall of the plate so the outer wall temperature could be measured.

The inside and outside temperature measurements can be used to solve a coupled conduction/radiation problem which accounted for absorption, emission, and reflection of the thermal energy from the layers and the surroundings, to determine the temperature profiles within the multilayer. The heat flux and heat transfer coefficient could then be calculated for every camera pixel of the plate.

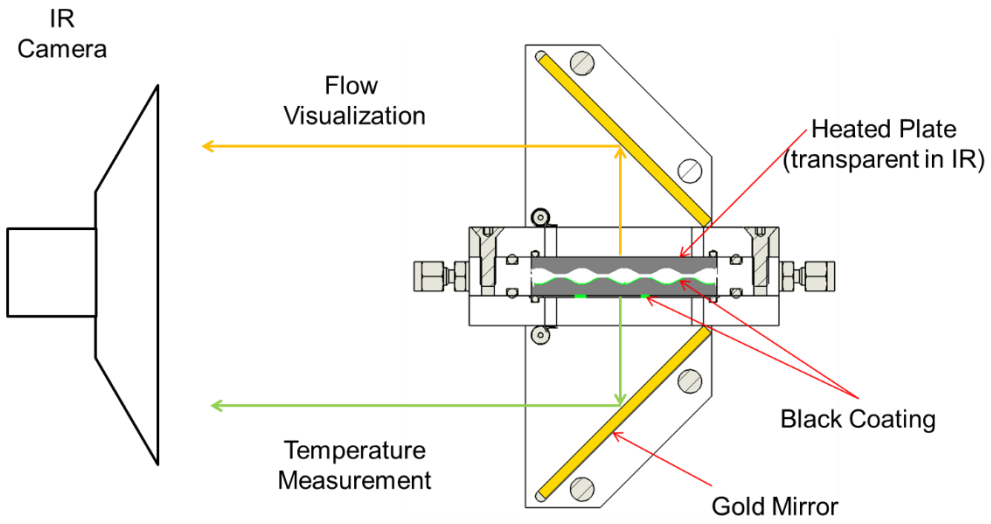

(a)

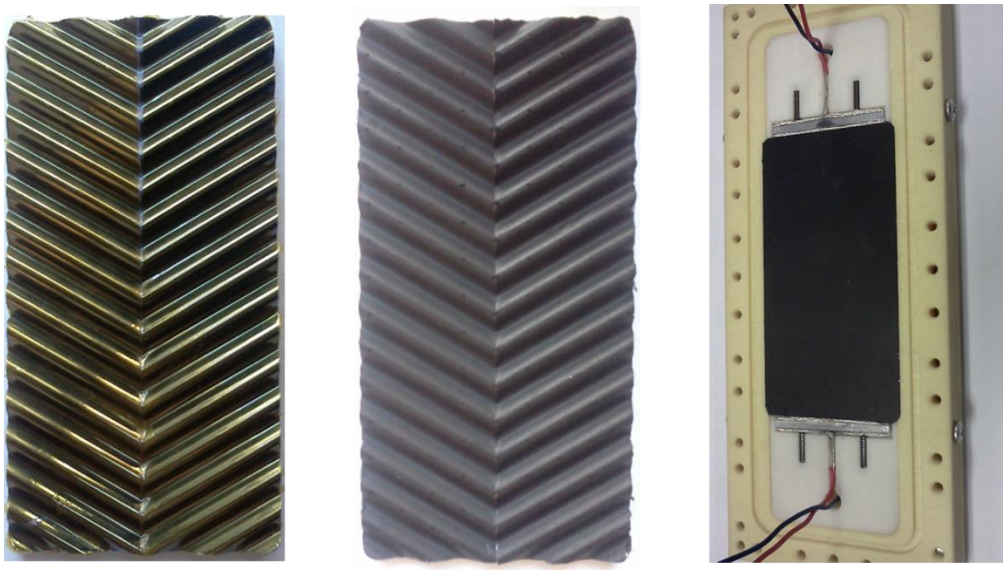

(b) (c) (d)

Figure 8.8: Schematic of the test section (a). Silicon plates covered with transparent polyimide film (a) and black polyimide film (b) along with the test section (c), where the mechanical electrical contact is shown.

Two gold mirrors were used to simultaneously capture both plates with the IR-camera, since silicon and polyimide are partially transparent in the IR-spectrum and therefore allowing heat transfer measurements on one plate and flow visualization on

the other plate. The two plates along with the test section without the mirrors are shown in Figure 8.8.

Figure 8.9 shows the raw temperature output of the IR-camera of both plates during pool boiling. Besides the clearly visible contact points on both plates, dark patches that are located between the trough and crest can be observed.

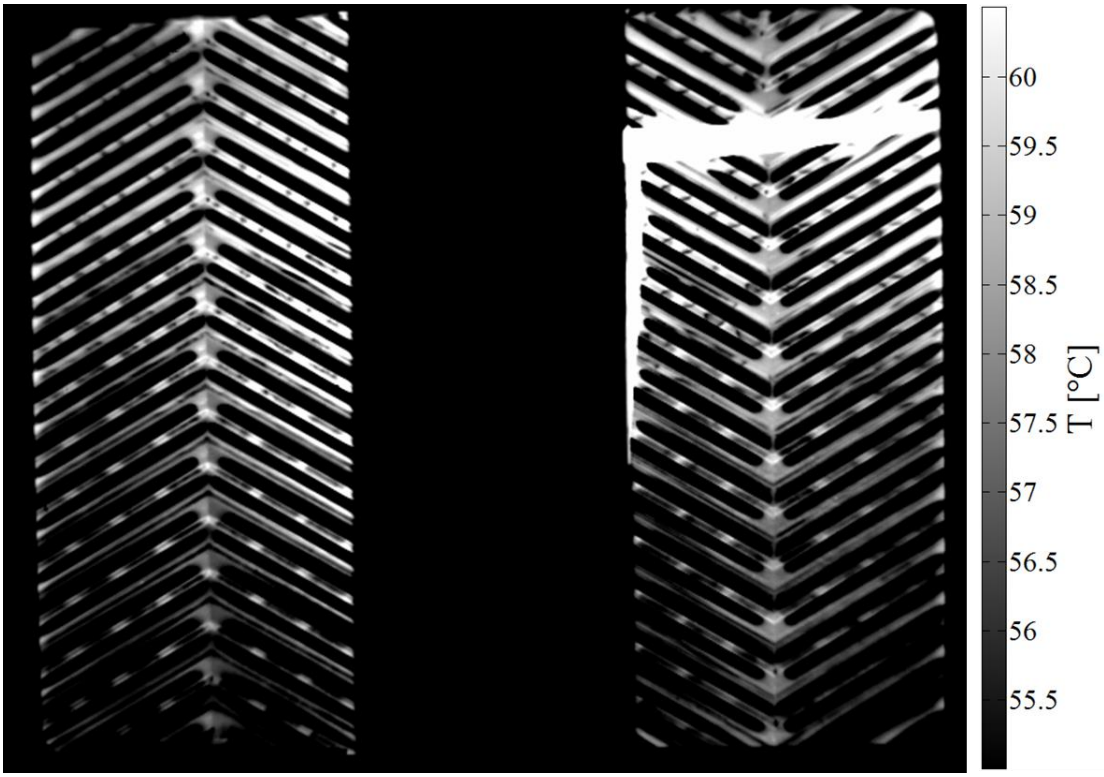

Figure 8.9: Raw temperature output of the IR-camera during pool boiling within the PHE geometry, Left: Silicon plate with transparent polyimide film, right: silicon with black polyimide film.

These dark patches were also observed during adiabatic operation, where a uniform temperature distribution would be expected. To understand the forming of the mentioned dark patches a ray tracing simulation had to be performed. Ray tracing follows the path of a light beam accounting for reflection and refraction at each

interface between two materials with different index of refraction, according to Snell's law.

$$\frac{\sin \Theta_1}{\sin \Theta_2} = \frac{n_2}{n_1} \qquad 8.2$$

Where Θ_1 and Θ_2 are the angle of incident and angle of refraction respectively and n_1 and n_2 are the index of refraction of the two materials. During each reflection/refraction the energy flux of the beam is divided over the two new rays. The ratio between the two new rays is governed by the index of refraction of both materials and can be expressed by Fresnel's equation:

$$r = \left(\frac{n_1 \cos \Theta - n_2 \cos \Theta}{n_1 \cos \Theta + n_2 \cos \Theta}\right)^2 \xrightarrow{\Theta=0} \left(\frac{n_1 - n_2}{n_1 + n_2}\right)^2 \qquad 8.3$$

Where r is the percentage of the initial ray that gets reflected and $(1 - r)$ is the percentage that passes through the material and gets refracted.

Figure 8.10 shows a simplified 2-D version of the ray tracing simulation. The starting point of the simulation is located between the trough and crest. The initial cone has an angle of approximately 70° due to the thin polyimide layer (not shown) that is attached on the silicon.

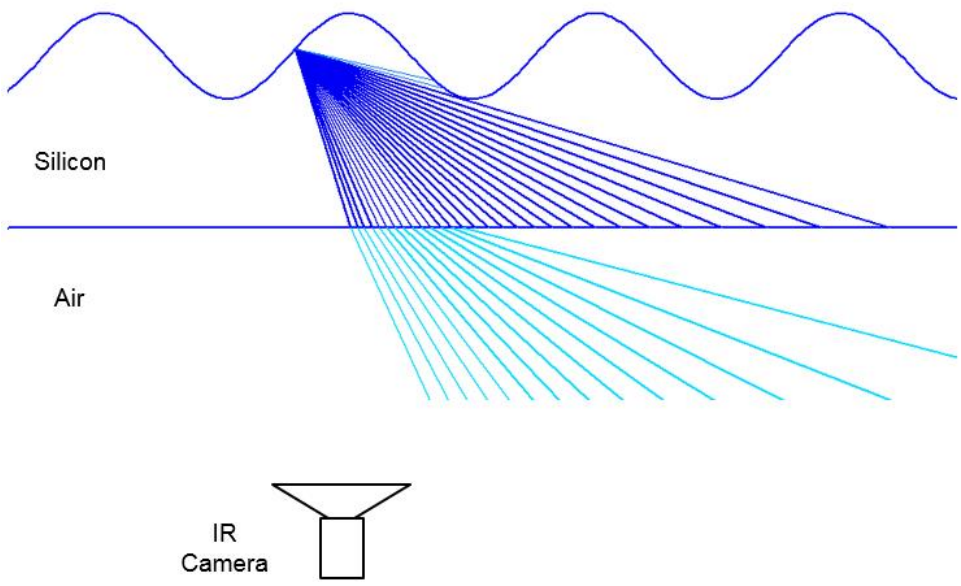

Figure 8.10: Ray tracing of the L5.7A1.0B60-60 geometry, with the starting point located between trough and crest, showing the initial light cone and the first refraction

The simulation shows that none of the initial rays will reach the lens of the camera. In addition more than half of the initial cone will be totally internal reflected, so they will not exit the silicon at all. Figure 8.11 shows the qualitative energy distribution of the wave pattern as the IR-camera would see for an adiabatic case. As can be seen the pattern is very similar to the one observed in Figure 8.9.

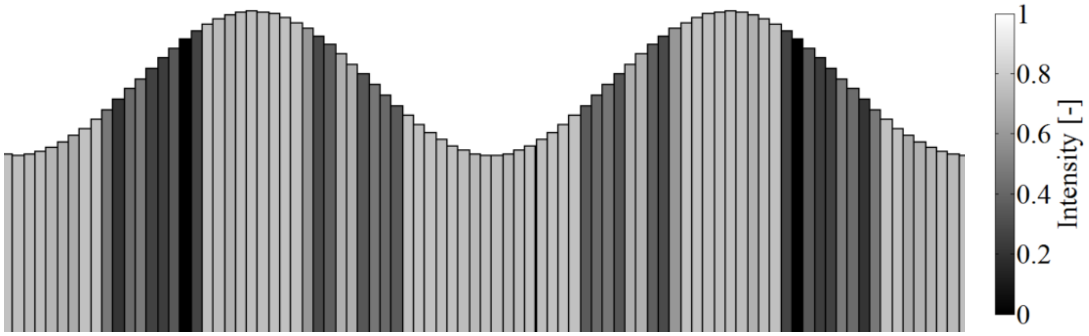

Figure 8.11: Qualitative intensity distribution along the wave pattern of a uniform heated silicon plate, when measured with an IR-camera, with the initial intensity being unity.

The intuitive solution to that problem would be altering the geometry of the corrugation so that at least one ray of the initial cone will exit the flat side of the silicon with a 90° angle. This can be done by either increasing the wavelength or decreasing the amplitude. Figure 8.12 shows the altered geometry of the corrugation. Due to the high index of refraction of silicon ($n_{si} \approx 3.5$) a relative high amount of radiation gets reflected at the interface between silicon-air ($R{\sim}0.30$) and also silicon-polyimide ($R{\sim}0.12$).

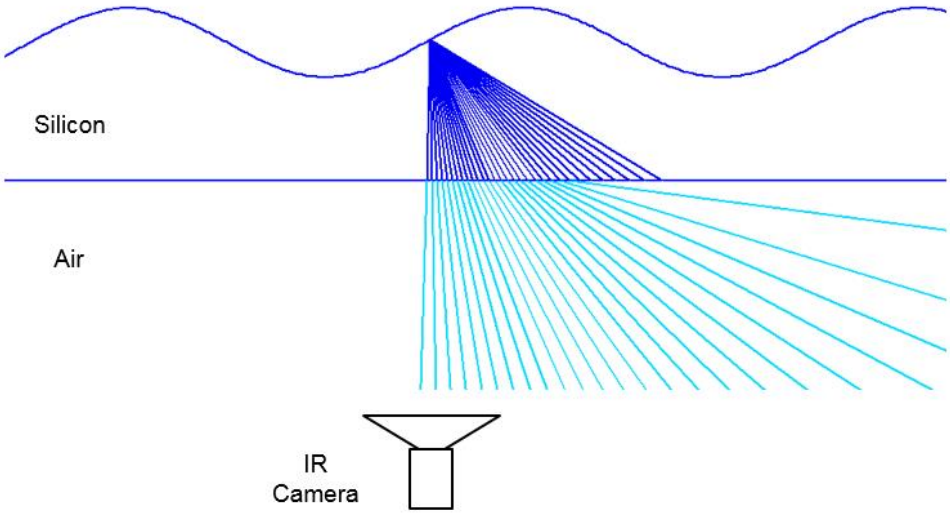

Figure 8.12: Ray tracing of the altered geometry so at least one ray of the initial light cone will exit the flat side of the silicon plate perpendicular, when the starting point is located between the trough and crest.

As was seen in Figure 8.7 the highest transmission of a silicon waver is of the order of 55%, meaning that the majority of the rays are reflected since absorptivity of silicone in the IR-spectrum is small. When using a flat silicon surface as the heating element, it is possible to calculate all loses due to reflection within the multilayer, as was done in Kim et al. [60]. For a curved surface however the rays do not remain

perpendicular as shown in Figure 8.13, which makes a full ray tracing calculation close to impossible.

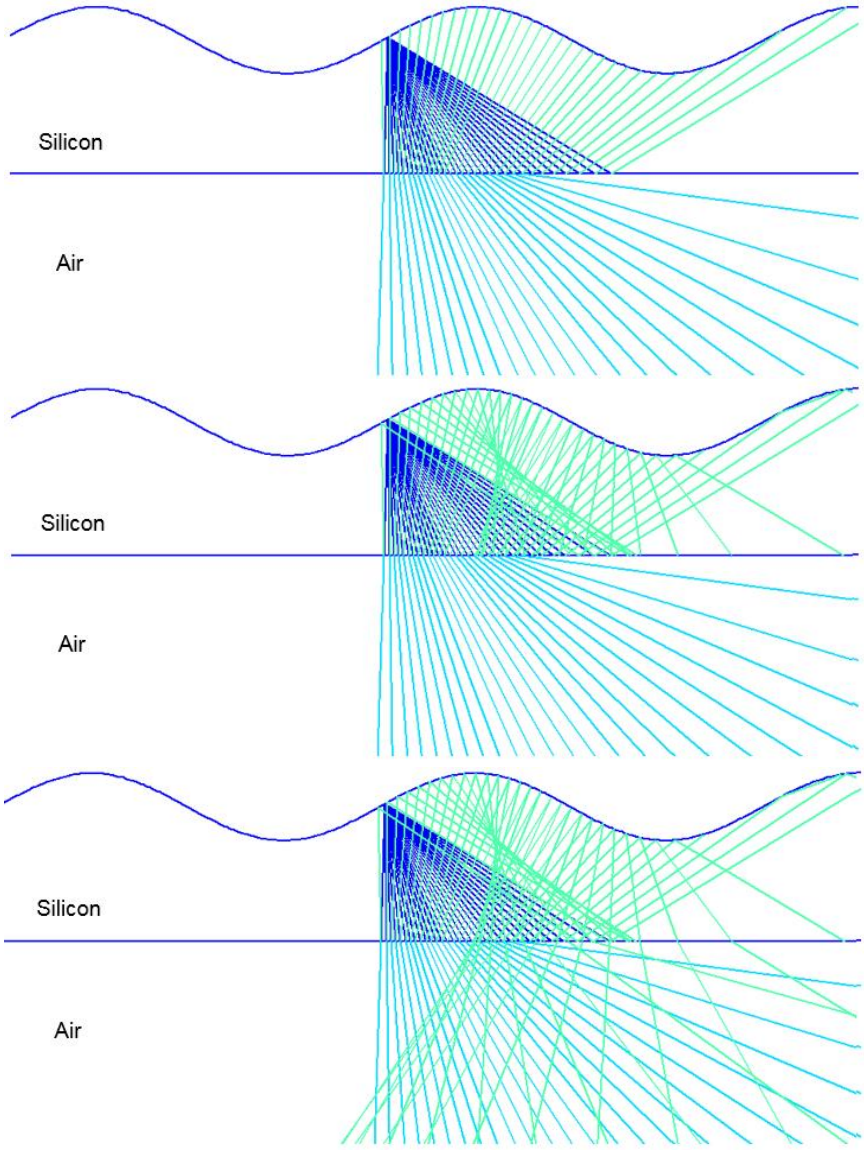

Figure 8.13: Continuation of the ray tracing from Figure 8.12 adding 1st (top), 2nd reflection (center) rays and 2nd refracted rays (bottom).

Using a calibration technique as is discussed in section 4.3 would not be able to solve for the steady state temperature of a single pixel either, since neighboring points on the curved surface would interact with other points and therefore falsifying the true

temperature value of each pixel. This can be observed in the left image of Figure 8.9 where the black tape that was attached on the flat side of the silicon plate clearly interacts with its neighboring point as well as the center of the plate where the two corrugation of the herringbone pattern meet.

Choosing a different material for the PHE geometry, with a lower index of refraction such as CaF_2 ($n_{CaF_2} \approx 1.5$) proved to eliminate that problem since the effect of reflected rays within the multilayer became negligible as can be seen in the ray tracing simulation in Figure 8.14. However CaF_2 is not a semiconductor as is silicon, which meant that a new method for heating the liquid was needed.

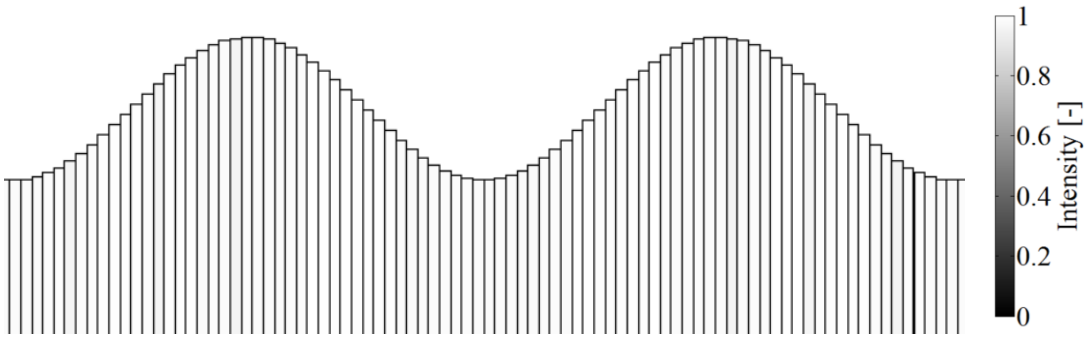

Figure 8.14: Qualitative intensity distribution along the wave pattern of a uniform heated CaF_2 plate, when measured with an IR-camera, with the initial intensity being unity.

8.3.2 Gold coated polyimide tape

Before using the 200RS100 film other options for heating the CaF_2 plate were considered. The first option was to apply the same black polyimide tape that was used for the silicon plates (section 8.3.1) on the corrugation of the CaF_2 and deposit a thin layer of metal on top of the black surface. Sputtering and vacuum vapor deposition were used to apply a 50 nm thick gold layer. However due to the nature of the

corrugation the film could not be deposited with a uniform thickness by either method, as can be seen in Figure 8.15. In addition, the working fluid HFE7100 would wash of the gold over time, contaminating the liquid and lowering the resistance of the heater.

Therefore it was decided to apply the gold onto the polyimide film and add a protection layer on top of the gold, prior to adhering the film to the CaF_2. The protective layer consisted of a uniform thin PMMA film that was created by spin coating. The result was a multilayer that could be uniformly heated and would withstand the dissolving effect of the working liquid (Figure 8.16a). However the gold layer got damaged during the application of the multilayer on the plate due to the sharp radii (1 mm) of the corrugation at the crest. This was causing a lower resistance at the crest and therefore increased the amount of heat flux at the crest, as can be seen in Figure 8.16b. In general coating the polyimide film with a thin gold layer turned out to be unreliable and not repeatable and therefore was not used for the experiment.

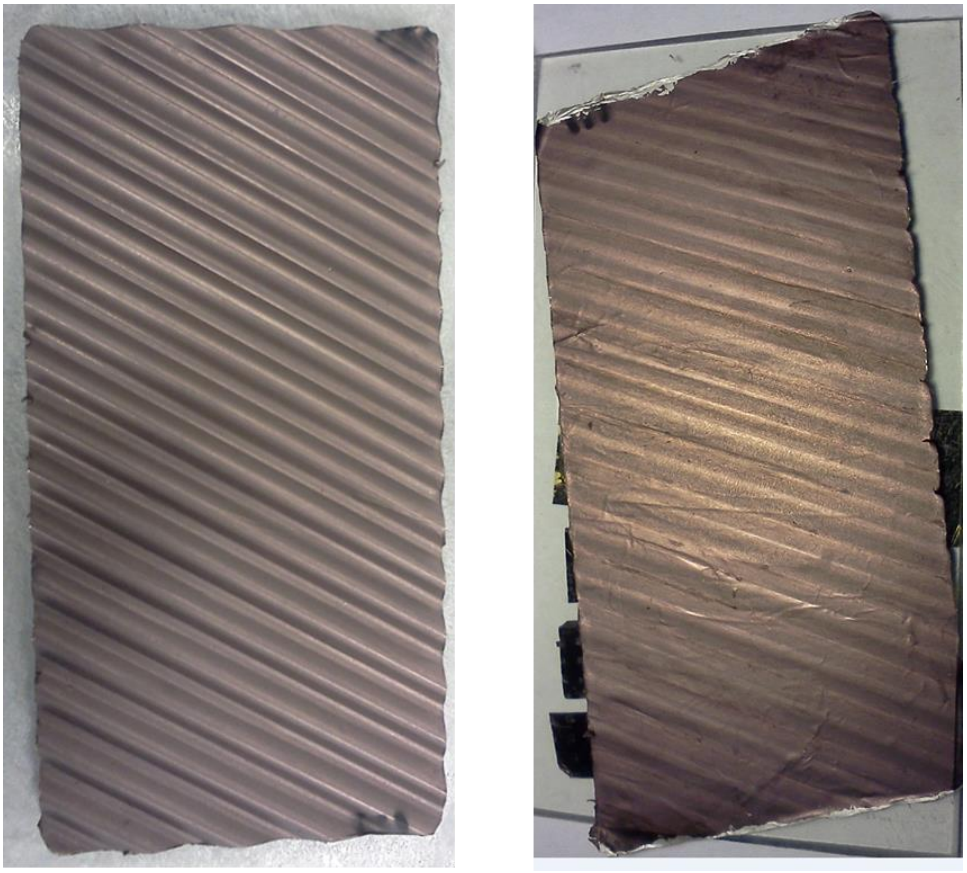

(a) (b)

Figure 8.15: Black polyimide tape with gold sputtered layer while being attached on the corrugated plate (a), non-uniformity of the gold layer becomes visible after detaching the tape from the plate (b)

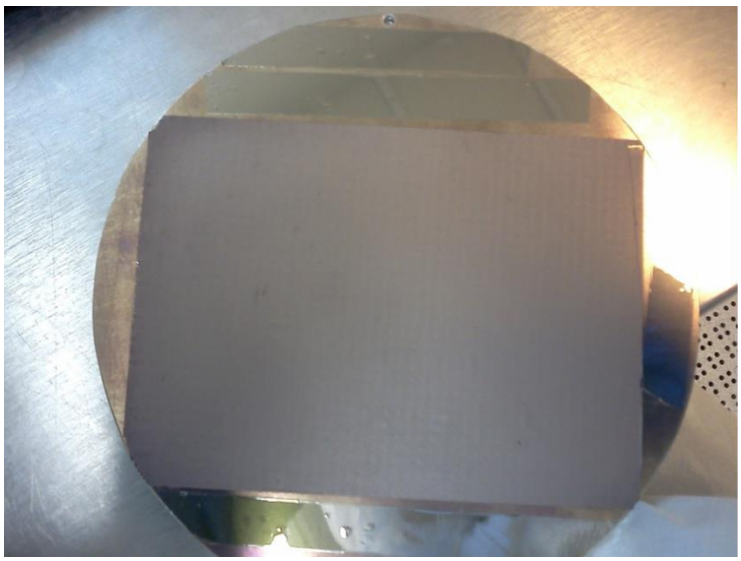

(a)

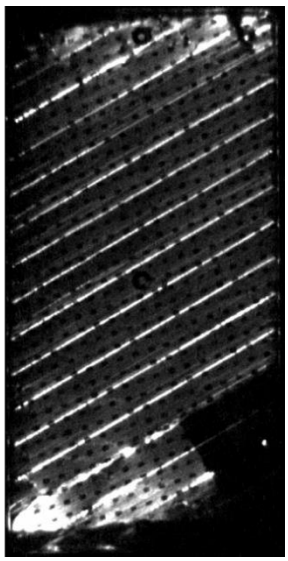

(b)

Figure 8.16: Black polyimide tape with gold sputtered layer while being attached to a flat surface (a), non-uniformity heating of the gold layer due to the small radii of the corrugations seen by the IR-camera during heating (b)

9. Bibliography

[1] J. Collier, J. Thome, Convective Boiling and Condensation, (1994).

[2] J.C. Chen, Correlation for boiling heat transfer to saturated fluids in convective flow, Ind. Eng. Chem. Process Des. Dev. 5 (1966) 322–329. doi:10.1021/i260019a023.

[3] D. Steiner, J. Taborek, Flow boiling heat transfer in vertical tubes correlated by an asymptotic model, Heat Transf. Eng. 13 (1992) 43–69.

[4] Z.H. Ayub, Plate Heat Exchanger Literature Survey and New Heat Transfer and Pressure Drop Correlations for Refrigerant Evaporators, Heat Transf. Eng. 24 (2003) 3–16. doi:10.1080/01457630390218074.

[5] R.M. Manglik, L. Wang, B. Sunden, Plate Heat Exchangers: Design, Applications and Performance, WIT Press, Southampton, 2007.

[6] M.M. Abu-Khader, Plate heat exchangers: Recent advances, Renew. Sustain. Energy Rev. 16 (2012) 1883–1891. doi:10.1016/j.rser.2012.01.009.

[7] K. Okada, M. Ono, T. Tomimura, T. Okuma, H. Konno, S. Ohtani, Design and Heat Transfer Characteristics of New Plate Heat Exchanger, Heat Transf. Res. 1 (1972) 90–95.

[8] R. Heavner, Performance of an industrial plate heat exchanger: effect of chevron angle, AIChE Symp. Ser. 89 (1993) 262–267.

[9] W.W. Focke, J. Zachariades, I. Olivier, The effect of the corrugation inclination angle on the thermohydraulic performance of plate heat exchangers, Int. J. Heat Mass Transf. 28 (1985) 1469–1479.

[10] A. Muley, R.M. Manglik, Experimental Study of Turbulent Flow Heat Transfer and Pressure Drop in a Plate Heat Exchanger with Chevron Plates, J. Heat Transfer. 121 (1999) 110–117.

[11] B. Thonon, R. Vidil, C. Marvillet, Recent research and developments in plate heat exchangers, J. Enhanc. Heat Transf. 2 (1995) 149–155.

[12] T.S. Khan, M.S. Khan, M.-C. Chyu, Z.H. Ayub, Experimental investigation of single phase convective heat transfer coefficient in a corrugated plate heat exchanger for multiple plate configurations, Appl. Therm. Eng. 30 (2010) 1058–1065. doi:10.1016/j.applthermaleng.2010.01.021.

[13] G. Gaiser, V. Kottke, Flow phenomena and local heat and mass transfer in corrugated passages, Chem. Eng. Technol. - CET. 12 (1989) 400–405. doi:10.1002/ceat.270120157.

[14] J. Stasiek, M.W. Collins, M. Ciofalo, P.E. Chew, Investigation corrugated of flow and heat transfer in Experimental results, Int. J. Heat Mass Transf. 39 (1996) 149–164.

[15] M. Ciofalo, J. Stasiek, M.W. Collins, Investigation of flow and heat transfer in corrugated passages—II. Numerical simulations, Int. J. Heat Mass Transf. 39 (1996) 165–192. doi:10.1016/S0017-9310(96)85014-9.

[16] S. Freund, S. Kabelac, Investigation of local heat transfer coefficients in plate heat exchangers with temperature oscillation IR thermography and CFD, Int. J. Heat Mass Transf. 53 (2010) 3764–3781. doi:10.1016/j.ijheatmasstransfer.2010.04.027.

[17] I. Gherasim, M. Taws, N. Galanis, C.T. Nguyen, Heat transfer and fluid flow in a plate heat exchanger part I. Experimental investigation, Int. J. Therm. Sci. 50 (2011) 1492–1498. doi:10.1016/j.ijthermalsci.2011.03.018.

[18] I. Gherasim, N. Galanis, C.T. Nguyen, Heat transfer and fluid flow in a plate heat exchanger. Part II: Assessment of laminar and two-equation turbulent models, Int. J. Therm. Sci. 50 (2011) 1499–1511. doi:10.1016/j.ijthermalsci.2011.03.017.

[19] G.A. Longo, Hydrocarbon Refrigerant Vaporization Inside a Brazed Plate Heat

Exchanger, J. Heat Transfer. 134 (2012) 1–10. doi:10.1115/1.4006817.

[20] G. Croce, P. D'Agaro, Numerical analysis of forced convection in plate and frame heat exchangers, Int. J. Numer. Methods Heat Fluid Flow. 12 (2002) 10–20.

[21] H.M. Metwally, R.M. Manglik, Enhanced heat transfer due to curvature-induced lateral vortices in laminar flows in sinusoidal corrugated-plate channels, Int. J. Heat Mass Transf. 47 (2004) 2283–2292. doi:10.1016/j.ijheatmasstransfer.2003.11.019.

[22] W.W. Focke, P.G. Knibbe, Flow visualization in parallel plate ducts with corrugated walls.pdf, J. Fluid Mech. (1986).

[23] M. Gradeck, M. Lebouché, Two-phase gas–liquid flow in horizontal corrugated channels, Int. J. Multiph. Flow. 26 (2000) 435–443. doi:10.1016/S0301-9322(99)00018-X.

[24] C. Tribbe, H.M. Müller-Steinhagen, Gas/Liquid Flow in Plate-and-Frame Heat Exchangers - Part II: Two-Phase Multiplier and Flow Pattern Analysis, Heat Transf. Eng. 22 (2001) 12–21. doi:10.1080/01457630150215686.

[25] P. Vlasogiannis, G. Karagiannis, P. Argyropoulos, V. Bontozoglou, Air–water two-phase flow and heat transfer in a plate heat exchanger, Int. J. Multiph. Flow. 28 (2002) 757–772. doi:10.1016/S0301-9322(02)00010-1.

[26] Y.Y. Hsieh, L.J. Chiang, T.-F. Lin, Subcooled flow boiling heat transfer of R-134a and the associated bubble characteristics in a vertical plate heat exchanger, Int. J. Heat Mass Transf. 45 (2002) 1791–1806. doi:10.1016/S0017-9310(01)00294-0.

[27] H. Asano, N. Takenaka, T. Fujii, N. Maeda, Visualization and void fraction measurement of gas-liquid two-phase flow in plate heat exchanger., Appl. Radiat. Isot. 61 (2004) 707–713. doi:10.1016/j.apradiso.2004.03.098.

[28] K. Nilpueng, S. Wongwises, Two-phase gas–liquid flow characteristics inside a plate heat exchanger, Exp. Therm. Fluid Sci. 34 (2010) 1217–1229. doi:10.1016/j.expthermflusci.2010.05.001.

[29] G.N. Danilova, V.M. Azarskov, B.B. Zemskov, Danilova Teploobmen v plastinchatihisparitljan razichnole geometri, Kholod. Tek. 4 (1981) 25–31.

[30] H.R. Engelhorn, A.M. Reinhart, Investigations on heat transfer in a plate evaporator, Chem. Eng. Process. Process Intensif. 28 (1990) 143–146. doi:10.1016/0255-2701(90)80011-S.

[31] C. Tribbe, H.M. Müller-Steinhagen, Gas/Liquid Flow in Plate-and-Frame Heat Exchangers - Part I: Pressure Drop Measurements, Heat Transf. Eng. 22 (2001) 5–11. doi:10.1080/01457630150215677.

[32] H. Kumar, The design of plate heat exchangers for refrigerants, Proceedigs Conf. Institue Refrig. (1992) 5.1–5.2.

[33] L. Margat, B. Thonon, L. Tadrist, Heat transfer and two-phase flow characteristics during convective boiling in a corrugated channel, Bell House, New York, 1997.

[34] D.H. Han, K.J. Lee, Y.H. Kim, Experiments on the characteristics of evaporation of R410A in brazed plate heat exchangers with different geometric configurations, Appl. Therm. Eng. 23 (2003) 1209–1225. doi:10.1016/S1359-4311(03)00061-9.

[35] J.H. Park, Y.S. Kim, Evaporation heat transfer and pressure drop characteristics of R-134a in the oblong shell and plate heat exchanger, KSME Int. J. 18 (2004) 2284–2293.

[36] B. Palm, J. Claesson, Plate Heat Exchangers: Calculation Methods for Singleand Two-Phase Flow, Heat Transf. Eng. 27 (2006) 88–98. doi:10.1080/01457630500523949.

[37] A. Cooper, Condensation of steam in plate heat exchangers, AIChE Symp. Ser. 70 (1987) 172–177.

[38] D. Sterner, B. Sunden, Performance of Plate Heat Exchangers for Evaporation of Ammonia, Heat Transf. Eng. 27 (2006) 45–55. doi:10.1080/01457630600559611.

[39] E. Djordjevic, S. Kabelac, Flow boiling of R134a and ammonia in a plate heat exchanger, Int. J. Heat Mass Transf. 51 (2008) 6235–6242. doi:10.1016/j.ijheatmasstransfer.2008.01.042.

[40] F. Táboas, M. Vallès, M. Bourouis, A. Coronas, Flow boiling heat transfer of ammonia/water mixture in a plate heat exchanger, Int. J. Refrig. 33 (2010) 695–705. doi:10.1016/j.ijrefrig.2009.12.005.

[41] F. Táboas, M. Vallès, M. Bourouis, A. Coronas, Assessment of boiling heat transfer and pressure drop correlations of ammonia/water mixture in a plate heat exchanger, Int. J. Refrig. 35 (2012) 633–644. doi:10.1016/j.ijrefrig.2011.10.003.

[42] D. Chisholm, A theoretical basis for the Lockhart-Martinelli correlation for two-phase flow, Int. J. Heat Mass Transf. 10 (1967) 1767–1778. doi:10.1016/0017-9310(67)90047-6.

[43] J. Huang, T.J. Sheer, M. Bailey-McEwan, Heat transfer and pressure drop in plate heat exchanger refrigerant evaporators, Int. J. Refrig. 35 (2012) 325–335. doi:10.1016/j.ijrefrig.2011.11.002.

[44] R.K. Shah, W.W. Focke, Plate heat exchangers and their design theory, Hemishere, Washington, 1988.

[45] T. Khan, M. Khan, M.-C. Chyu, Z. Ayub, J. Chattha, Review of Heat Transfer and Pressure Drop Correlations for Evaporation of Fluid Flow in Plate Heat Exchangers (RP-1352), HVAC&R Res. 15 (2009) 169–188. doi:10.1080/10789669.2009.10390832.

[46] M.S. Khan, T.S. Khan, M.C. Chyu, Z.H. Ayub, Experimental investigation of evaporation heat transfer and pressure drop of ammonia in a 30 chevron plate heat exchanger, Int. J. Refrig. 35 (2012) 1757–1765. doi:10.1016/j.ijrefrig.2012.05.019.

[47] T.S. Khan, M.S. Khan, M.C. Chyu, Z.H. Ayub, Experimental investigation of evaporation heat transfer and pressure drop of ammonia in a 60 chevron plate heat exchanger, Int. J. Refrig. 35 (2012) 336–348. doi:10.1016/j.ijrefrig.2011.10.018.

[48] M.S. Khan, T.S. Khan, M.-C. Chyu, Z.H. Ayub, Evaporation heat transfer and pressure drop of ammonia in a mixed configuration chevron plate heat exchanger, Int. J. Refrig. 41 (2014) 92–102. doi:10.1016/j.ijrefrig.2013.12.015.

[49] T.S. Khan, M.S. Khan, M.-C. Chyu, Z.H. Ayub, Ammonia evaporation in a mixed configuration chevron plate heat exchanger with and without miscible oil, Int. J. Refrig. 51 (2015) 120–134. doi:10.1016/j.ijrefrig.2014.12.002.

[50] R.L. Amalfi, F. Vakili-Farahani, J.R. Thome, Flow boiling and frictional pressure gradients in plate heat exchangers: part 2, comparison of literature methods to database and new prediction methods, Int. J. Refrig. (2015). doi:10.1016/j.ijrefrig.2015.07.009.

[51] R.L. Amalfi, F. Vakili-Farahani, J.R. Thome, Flow boiling and frictional pressure gradients in plate heat exchangers: part 1, review and experimental database, Int. J. Refrig. (2015). doi:10.1016/j.ijrefrig.2015.07.010.

[52] F. Vakili-Farahani, R.L. Amalfi, J.R. Thome, Two-Phase Flow and boiling of R-245fa in a 1 mm pressing depth plate heat exchanger — Part I : Adiabatic pressure Drop, Interfacial Phenom. Heat Transf. 2 (2014) 325–342.

[53] F. Vakili-Farahani, R.L. Amalfi, J.R. Thome, Two-Phase Flow and boiling of R-245fa in a 1 mm pressing depth plate heat exchanger — Part II : Flow boiling heat transfer, Interfacial Phenom. Heat Transf. 2 (2014) 343–361.

[54] E. Lee, H. Kang, Y. Kim, Flow boiling heat transfer and pressure drop of water in a plate heat exchanger with corrugated channels at low mass flux conditions, Int. J. Heat Mass Transf. 77 (2014) 37–45. doi:10.1016/j.ijheatmasstransfer.2014.05.019.

[55] M. Vollmer, K.-P. Moellmann, Infrared Thermal Imaging, WILEY-VCH Verlag GmbH & Co. KGaA, Weinheim, 2010.

[56] V.J. Gokhale, O.A. Shenderova, G.E. McGuire, M. Rais-Zadeh, Infrared absorption properties of carbon nanotube/nanodiamond based thin film coatings, J. Microelectromechanical Syst. 23 (2014) 191–197. http://ieeexplore.ieee.org/xpls/abs_all.jsp?arnumber=6558489 (accessed October 22, 2014).

[57] T. Astarita, G. Cardone, G.M. Carlomagno, C. Meola, M. Melloni, G. Kirchho, et al., A survey on infrared thermography for convective heat transfer measurements, 32 (2001) 593–610.

[58] A.C. Talik, L.S. Fletcher, N.K. Anand, L.W. Swanson, Heat Transfer and Pressure Drop Characteristics of a Plate Heat Exchanger, Proc. ASME/JSME Therm. Eng. Conf. 4 (1995) 321–329.

[59] H. Kumar, The Plate Heat Exchanger: Construction and Design, Inst. Chem. Eng. Symp. Ser. 86 (1984) 1275–1288.

[60] T.H. Kim, E. Kommer, S. Dessiatoun, J. Kim, Measurement of two-phase flow and heat transfer parameters using infrared thermometry, Int. J. Multiph. Flow. 40 (2012) 56–67. doi:10.1016/j.ijmultiphaseflow.2011.11.012.

[61] V.D. Donowski, S.G. Kandlikar, Correlating Evaporation Heat Transfer Coefficient of Refrigerant R-134a in a Plate Heat Exchanger, Paper 154, Alaska, 2000.

[62] Y.Y. Hsieh, T.-F. Lin, Evaporation Heat Transfer and Pressure Drop of Refrigerant R410a Flow in a Vertical Plate Heat Exchanger, J. Heat Transfer.

125 (2003) 852–857.

[63] E. Kommer, FORCED CONVECTIVE BOILING VIA INFRARED THERMOMETRY, University of Maryland, 2011.

[64] Lattice, HIGH PURITY SILICON FOR OPTICAL APPLICATIONS, (2015). http://50.87.248.68/~lattice3/wp-content/uploads/2014/08/Optical-Silicon-Whitepaper.pdf.